

The Audible Human Project: Modeling Sound Transmission in the Lungs and Torso

BY

ZOUJUN DAI

B.S., Shanghai Jiaotong University, Shanghai, China, 2006

THESIS

Submitted as partial fulfillment of the requirements
for the degree of Doctor of Philosophy in Mechanical Engineering
in the Graduate College of the
University of Illinois at Chicago, 2013

Chicago, Illinois

Defense Committee:

Thomas Royston, Chair and Advisor
Ahmed Shabana, Mechanical & Industrial Engineering
Michael Scott, Mechanical & Industrial Engineering
Richard Magin, Bioengineering
Hansen Mansy, Rush University Medical Center

DEDICATION

To my family for the unwavering support and encouragement over the years.

ACKNOWLEDGEMENTS

I express sincere appreciation, first and foremost, to my revered advisor Professor Thomas Royston for his guidance and patience throughout this research. Also I would like to thank Professor Hansen Mansy for his support and guidance.

I am grateful to the other members of the dissertation committee, Professor Richard Magin, Michael Scott and Ahmed Shabana, for their comments and suggestions. The financial support of the National Institute of Health (Grant No. EB012142) is acknowledged.

I express thanks to my colleague Ying Peng and Brian Henry who work on the Audible Human Project with me. Additionally, I must express thanks to my other colleagues (past and present) of the Acoustics and Vibration Laboratory, in particular Temel Yasar, Yifei Liu, Rajesh Chaunsali, Faik Meral, Serhan Acikgoz and Mehmet Ozer for helpful advice, insight and support. It is fortunate indeed for me to have my bosom friend David H. Hwang. But for the aegis of his learning and versatility, my academic horizons would have been far less expansive. Jiehui Zhao, Ningli Yang and Qiaojian Huang are also acknowledged for their help in this research. Last but not least, I thank my parents and my grandfather for their love and encouragement throughout this endeavor.

Zoujun Dai

TABLE OF CONTENTS

CHAPTER	PAGE
1. INTRODUCTION.....	1
1.1. Background and Motivation	1
1.2. Literature Review	2
1.3. Research Objective	7
1.4. Dissertation Overview	8
1.5. References.....	9
2. LUNG TISSUE VISCOELASTICITY	15
2.1. Introduction	15
2.2. Theory.....	17
2.2.1. Viscoelastic Continuum: Equation of Motion.....	17
2.2.2. Relaxed Elastic Moduli Estimation of Viscoelastic Medium by Indentation	20
2.2.3. Surface Wave Propagation on a Half-Space due to a Surface Source	22
2.2.4. Viscoelasticity Estimation from Surface Wave Measurements	23
2.3. Viscoelasticity Identification of a Tissue-Mimicking Phantom	26
2.3.1. Analytical Case Studies.....	26
2.3.2. Numerical Case Studies	30
2.3.3. Experimental Studies	34
2.4. Viscoelasticity Identification of Ex Vivo Pig Lungs	37
2.4.1. Compression Wave, Shear Wave and Surface Wave in the Lung	37
2.4.2. Experimental Studies.	39
2.5. Discussion.....	42
2.6. References.....	43
3. POROVISCOELASTIC MODELING OF SOUND PROPAGATION IN THE LUNG	48
3.1. Introduction	48

TABLE OF CONTENTS (Continued)

CHAPTER	PAGE
3.2. Biot Theory Applied to Wave Propagation in the Lung	50
3.3. Comparison of Wave Speed and Attenuation Predictions.....	54
3.4. Ex Vivo Experimental Studies on Pig Lung.....	57
3.4.1. Lung Preparation	57
3.4.2. Mass and Air Volume Fraction of Inflated Lung	57
3.4.3. Permeability Measurement on Dried Pig Lung	58
3.4.4. Mechanical Indentation Tests on the Lung	60
3.4.5. Surface Wave Measurements	61
3.4.6. Compression Wave Measurements	62
3.5. Discussion.....	70
3.6. References.....	71
4. SOUND TRANSMISSION IN AIRWAYS AND COUPLING TO LUNG PARENCHYMA.....	75
4.1. Introduction	75
4.2. Theory.....	76
4.2.1. Horsfield Model of the Human Airway Tree	76
4.2.2. Mathematical and Diagrammatic Description of the Subglottal Model.....	80
4.3. Studies on Tissue-Mimicking Phantom.....	84
4.3.1. Airway Acoustics in Tissue-Mimicking Phantom	84
4.3.2. Sound Coupling into Tissue-Mimicking Phantom.....	88
4.4. Studies on Ex Vivo Pig Lung and In Vivo Human Lung	90
4.4.1. Pig Lung Excitation through Airway Insonification	90
4.4.2. Geometry Construction of Human Lung and Airway Tree.....	91
4.4.3. Simulations on Human Lung Excitation through Airway Insonification.....	93
4.5. Discussion.....	99

TABLE OF CONTENTS (Continued)

CHAPTER	PAGE
4.6. References	100
5. ACOUSTIC MEASUREMENTS OF SOUND TRANSMISSION IN HUMAN SUBJECTS ...	102
5.1. Introduction	102
5.2. Sound Transmission Measured by SLDV	103
5.3. Sound Transmission Measured by the Piezodisk Sensor	108
5.4. Comparison of Measurements by Two Techniques	114
5.5. Discussion.....	116
5.6. References	117
6. SUMMARY AND PERSPECTIVES.....	119
6.1. Summary.....	119
6.2. Topics for Future Research.....	122
CITED LITERATURE	125
VITA.....	136

LIST OF TABLES

TABLE	PAGE
Table 2.1	Viscoelastic material models used in analytical and numerical case studies.....26
Table 2.2	Estimated viscoelastic coefficients and residual error in analytical case studies28
Table 2.3	Estimated viscoelastic coefficients and residual error in numerical case studies32
Table 2.4	Estimated viscoelastic coefficients and residual error in experimental studies..... 36
Table 2.5	Estimated viscoelastic coefficients and residual error in experimental studies42
Table 3.1	Parameters for effective medium theory.....55
Table 3.2	Additional parameters for Biot theory.....55
Table 3.3	Lung parenchyma permeability.....60
Table 4.1	Structural parameters of the human airway model as adapted from Habib et al. [17] and scaled to match the Visible Human Male images (n , Horsefield airway order; $l^{(n)}$ and $d^{(n)}$, airway length and diameter, respectively; $h^{(n)}$, wall thickness between lumen and outer smooth muscle; $c(n)$, fractional cartilage content as a function of airway order n79
Table 4.2	Material properties of the tissue-mimicking phantom85
Table 4.3	Structural parameters of the airway tree (n , Horsefield airway order; $l^{(n)}$ and $d^{(n)}$, airway length and diameter, respectively; $h^{(n)}$, wall thickness, $\Delta^{(n)}$, recursion index)86
Table 4.4	Material properties and boundary conditions for simulation at 300 Hz96
Table 4.5	Material properties and boundary conditions for simulation at 500 Hz96
Table 5.1	Frequencies in each frequency band at which there are a maximum number of points with coherence ≥ 0.9107
Table 5.2	Frequencies in each frequency band at which there are a maximum number of points with coherence ≥ 0.9113

LIST OF FIGURES

FIGURE	PAGE
Figure 2.1	A tree arrangement of springs and dashpots (left) resulting in a fractional order element, called a springpot (middle). Schematic representation of a fractional order Voigt model (right); the dashpot is replaced with a springpot.....19
Figure 2.2	Different viscoelastic models: (a) Voigt (b) Fractional Voigt (c) Standard Linear Solid (SLS).....19
Figure 2.3	Ideal viscoelastic halfspace with finite surface source23
Figure 2.4	Theoretical studies. FRF at $\omega/2\pi = 100$ and 600 Hz for (a) Voigt, (b) fractional Voigt, and (c) SLS material studies. Key: — Real part, — • — Imaginary part. Material property values given in Table 2.1.....27
Figure 2.5	Voigt material study. Best fit Voigt, Fractional Voigt and SLS models based on (a) Approach 1 and (b) Approach 2. Key: ○ ○ ○ actual value, — estimated value based on Approach 1 or Approach 2, ▲— . —▲ best fit Voigt, □.....□ best fit Fractional Voigt, ◇— —◇ best fit SLS.....28
Figure 2.6	Fractional Voigt material study. Best fit Voigt, Fractional Voigt and SLS models based on (a) Approach 1 and (b) Approach 2. Key: ○ ○ ○ actual value, — estimated value based on Approach 1 or Approach 2, ▲— . —▲ best fit Voigt, □.....□ best fit Fractional Voigt, ◇— —◇ best fit SLS.....29
Figure 2.7	SLS material study. Best fit Voigt, Fractional Voigt and SLS models based on (a) Approach 1 and (b) Approach 2. Key: ○ ○ ○ actual value, — estimated value based on Approach 1 or Approach 2, ▲— . —▲ best fit Voigt, □.....□ best fit Fractional Voigt, ◇— —◇ best fit SLS.....29
Figure 2.8	Experimental schematic for measurement of surface wave motion caused by a surface source using a scanning laser Doppler vibrometer (SLDV)30
Figure 2.9	Numerical Studies FRF at $\omega/2\pi = 100$ and 600 Hz for (a) Voigt (b) fractional Voigt and (c) SLS material studies. Key: — Real part, — • — Imaginary part. Material property values given in Table 2.1.....31
Figure 2.10	Voigt numerical study. Best fit Voigt, Fractional Voigt and SLS models based on (a) Approach 1 and (b) Approach 2. Key: ○ ○ ○ actual value, — estimated value based on Approach 1 or Approach 2, ▲— . —▲ best fit Voigt, □.....□ best fit Fractional Voigt, ◇— —◇ best fit SLS.....33
Figure 2.11	Fractional Voigt numerical study. Best fit Voigt, Fractional Voigt and SLS models based on (a) Approach 1 and (b) Approach 2. Key: ○ ○ ○ actual value, — estimated value based on Approach 1 or Approach 2, ▲— . —▲ best fit Voigt, □.....□ best fit Fractional Voigt, ◇— —◇ best fit SLS.....33

LIST OF FIGURES (Continued)

FIGURE	PAGE
Figure 2.12	SLS numerical study. Best fit Voigt, Fractional Voigt and SLS models based on (a) Approach 1 and (b) Approach 2. Key: $\circ \circ \circ$ actual value, — estimated value based on Approach 1 or Approach 2, $\Delta - \Delta$ best fit Voigt, $\square \cdots \square$ best fit Fractional Voigt, $\diamond - \diamond$ best fit SLS.....34
Figure 2.13	Experimental study. FRF at $\omega/2\pi = 100, 200, 300$ and 400 Hz Key: — Real part, $-\bullet-$ Imaginary part.....35
Figure 2.14	Experimental study. Best fit Voigt, Fractional Voigt and SLS models based on (a) Approach 1 and (b) Approach 2. Key: — estimated value based on Approach 1 or Approach 2, $\Delta - \Delta$ best fit Voigt, $\square \cdots \square$ best fit Fractional Voigt, $\diamond - \diamond$ best fit SLS.....36
Figure 2.15	Experimental setup of ex vivo pig lung surface wave measurement.....40
Figure 2.16	Frequency response function versus radial position, $\circ \circ \circ$ 100 Hz, *** 500 Hz.....41
Figure 2.17	Experimental study. Best fit Voigt, Fractional Voigt and SLS models based on (a) Approach 1 and (b) Approach 2. Key: — estimated value based on Approach 1 or Approach 2, $\Delta - \Delta$ best fit Voigt, $\square \cdots \square$ best fit Fractional Voigt, $\diamond - \diamond$ best fit SLS.....42
Figure 3.1	Microscope image showing morphometric parameters h and r for an alveolar duct.....52
Figure 3.2	Compression and shear wave group velocity at 20 cm H ₂ O P _{tp} , — fast compression wave, Biot theory, — — slow compression wave, Biot theory, $-\cdot-$ compression wave, effective medium model, - - - shear wave, Biot theory.....56
Figure 3.3	Compression and shear wave attenuation at 20 cm H ₂ O P _{tp} , — fast compression wave, Biot theory, — — slow compression wave, Biot theory, $-\cdot-$ compression wave, thermal dissipation model, - - - shear wave, Biot theory.....56
Figure 3.4	Experimental setup for lung parenchyma permeability measurement.....59
Figure 3.5	Force and indentation depth relation in indentation measurement, $\circ \circ \circ$ experiment, 20cm H ₂ O, — least square fit, 20cm H ₂ O, $\square \square \square$ experiment, 10cm H ₂ O, — — least square fit, 10cm H ₂ O.....60
Figure 3.6	Surface wave speed, $\circ \circ \circ$ experiment, 20cm H ₂ O, line 1, $\square \square \square$ experiment, 20cm H ₂ O, line 2, — Fractional Voigt model least square fit, 20cm H ₂ O, $\Delta \Delta \Delta$ experiment, 10cm H ₂ O, line 1, + + + experiment, 10cm H ₂ O, line 2, — — Fractional Voigt model least square fit, 10cm H ₂ O.....62
Figure 3.7	Schematic diagram of compression wave measurement.....63
Figure 3.8	Experiment set up of compression wave measurement.....64

LIST OF FIGURES (Continued)

FIGURE	PAGE
Figure 3.9	Photo and dimension of subminiature microphone BL-21785-000.....65
Figure 3.10	Experiment setup of compression wave attenuation measurement.....65
Figure 3.11	Time history of the acceleration and velocity of a point at 400 Hz with 10 cm H ₂ O. The amplitude of the velocity is increased by 2000 times for ease of viewing here.....66
Figure 3.12	Fast compression wave group velocity, ○ ○ ○ experiment, 20cm H ₂ O, — Biot theory, 20cm H ₂ O, —.— effective medium model, 20cm H ₂ O, □ □ □ experiment, 10cm H ₂ O, — — Biot theory, 10cm H ₂ O, - - - effective medium model, 10cm H ₂ O. Bars on experiment denote 95% confidence interval.....68
Figure 3.13	Fast compression wave attenuation, ○ ○ ○ experiment, 20cm H ₂ O, location 1, □ □ □ experiment, 20cm H ₂ O, location 2, — Biot theory, 20cm H ₂ O, —.— effective medium model, 20cm H ₂ O, △ △ △ experiment, 10cm H ₂ O, location 1, + + + experiment, 10cm H ₂ O, location 2, — — Biot theory, 10cm H ₂ O, - - - effective medium model, 10cm H ₂ O.....70
Figure 4.1	Diagram of partial airway model of Horsfield (from 35 th to 23 rd order), adapted from Fredberg et al. [16]80
Figure 4.2	Airway acoustic model showing one bifurcation.....84
Figure 4.3	Phantom with airway tree inside.....85
Figure 4.4	Schematic diagram of the airway tree in the phantom.....85
Figure 4.5	3D geometry of the left half of the phantom.....87
Figure 4.6	FRF of Mic 2/Mic 1 (Pa/Pa), fixed boundary condition at all terminal segments, for locations refer to Figure 4.4. Key: — simulation, — theoretical prediction, — and — measurement.....88
Figure 4.7	Experimental setup of sound coupling into phantom measurement.....89
Figure 4.8	FRF of phantom surface velocity at 500 Hz. (Left: Simulation, Right: Experiment)89
Figure 4.9	FRF of phantom surface velocity at 1000 Hz. (Left: Simulation, Right: Experiment) ...90
Figure 4.10	FRF of phantom surface velocity at 1500 Hz. (Left: Simulation, Right: Experiment) ...90
Figure 4.11	Experiment setup of SLDV measurement of lung surface motion.....91
Figure 4.12	Human lung geometry from the Visible Human Project92

LIST OF FIGURES (Continued)

FIGURE	PAGE
Figure 4.13	(a) Computer generated airway tree with around 55000 segments (b) Details of the same airway tree.....93
Figure 4.14	(a) Geometry of the simplified airway tree with a total of 255 segments (b) Detail of the terminal airway segment.....94
Figure 4.15	(a) Simplified airway tree integrated into the lung (b) Mesh of the lung and airways.....95
Figure 4.16	Lung surface velocity at 300 Hz (a) Experiment (b) Simulation.....98
Figure 4.17	Lung surface velocity at 500 Hz (a) Experiment (b) Simulation.....98
Figure 4.18	Lung surface velocity from simulation (only areas within data range plotted) (a) 300 Hz (b) 500 Hz.....99
Figure 5.1	Schematic diagram of SLDV measurements on the back of the human subject. (adapted from [18])105
Figure 5.1	Human subject with bands of retro-reflective tape adhered to the back.....105
Figure 5.2	FRF of scanning points, — point on left back, — point on right back.....106
Figure 5.3	Coherence of scanning points, — point on left back, — point on right back.....106
Figure 5.4	FRF at 210 Hz, colorbar in dB, (a) FRF amplitude at the individually measured points (b) interpolated FRF amplitude contour plot.....108
Figure 5.5	FRF at 440 Hz, colorbar in dB, (a) FRF amplitude at the individually measured points (b) interpolated FRF amplitude contour plot.....108
Figure 5.6	(a) Silicone gel coupled piezodisk sensor (b) schematic diagram of the sensor.....109
Figure 5.7	Schematic diagram of piezodisk sensor calibration setup.....110
Figure 5.9	FRF of 3 piezodisk sensors from calibration.....110
Figure 5.10	Piezodisk sensors imbedded on a chair.....111
Figure 5.11	Schematic diagram Piezodisk sensor measurements (adapted from [18])112
Figure 5.12	FRF of scanning points, — point on left back, — point on right back.....112
Figure 5.13	Coherence of scanning points, — point on left back, — point on right back.....113
Figure 5.14	FRF at 352 Hz, colorbar in dB, (a) FRF amplitude at each sensor point (b) interpolated FRF amplitude contour plot.....114

LIST OF FIGURES (Continued)

FIGURE	PAGE
Figure 5.15	FRF at 512 Hz, colorbar in dB, (a) FRF amplitude at each sensor point (b) interpolated FRF amplitude contour plot.....114
Figure 5.16	Comparison of interpolated FRF amplitude contour plot at 352.5/352 Hz, (a) SLDV measurement (b) sensor array measurement.....115
Figure 5.17	Comparison of interpolated FRF amplitude contour plot at 440Hz, (a) SLDV measurement (b) sensor array measurement116

SUMMARY

Auscultation has been used qualitatively by physicians for hundreds of years to aid in the monitoring and diagnosis of pulmonary diseases. Alterations in the structure and function of the pulmonary system that occur in disease or injury often give rise to measurable changes in lung sound production and transmission. Numerous acoustic measurements have revealed the differences of breath sounds and transmitted sounds in the lung under normal and pathological conditions. Compared to the extensive cataloging of lung sound measurements, the mechanism of sound transmission in the pulmonary system and how it changes with alterations of lung structural and material properties has received less attention. A better understanding of sound transmission and how it is altered by injury and disease might improve interpretation of lung sound measurements, including new lung imaging modalities that are based on an array measurement of the acoustic field on the torso surface via contact sensors or are based on a 3-dimensional measurement of the acoustic field throughout the lungs and torso using magnetic resonance elastography.

A long-term goal of the **Audible Human Project (AHP)** is to develop a computational acoustic model that would accurately simulate generation, transmission and noninvasive measurement of sound and vibration within the pulmonary system and torso caused by both internal (e.g. respiratory function) and external (e.g. palpation) sources. The goals of this dissertation research, fitting within the scope of the AHP, are to develop specific improved theoretical understandings, computational algorithms and experimental methods aimed at transmission and measurement. The research objectives undertaken in this dissertation are as follows. (1) Improve theoretical modeling and experimental identification of viscoelasticity in soft biological tissues. (2) Develop a poroviscoelastic model for lung tissue vibroacoustics. (3) Improve lung airway acoustics modeling and its coupling to the lung parenchyma; and (4) Develop improved techniques in array acoustic measurement on the torso surface of sound transmitted through the pulmonary system and torso.

Tissue Viscoelasticity. Two experimental identification approaches of shear viscoelasticity were used. The first approach is to directly estimate the frequency-dependent surface wave speed and then to optimize the coefficients in an assumed viscoelastic model type. The second approach is to measure the complex-valued frequency response function (FRF) between the excitation location and points at known radial distances. The FRF has embedded in it frequency-dependent information about both surface wave phase speed and attenuation that can be used to directly estimate the complex shear modulus. The coefficients in an assumed viscoelastic tissue model type can then be optimized.

Poroviscoelasticity Model for Lung Vibro-acoustics. A poroviscoelastic model based on Biot theory of wave propagation in porous media was used for compression waves in the lungs. This model predicts a fast compression wave speed close to the one predicted by the effective medium theory at low frequencies and an additional slow compression wave due to the out of phase motion of the air and the lung parenchyma. Both compression wave speeds vary with frequency. The fast compression wave speed and attenuation were measured on an excised pig lung under two different transpulmonary pressures. Good agreement was achieved between the experimental observation and theoretical predictions.

Sound Transmission in Airways and Coupling to Lung Parenchyma. A computer generated airway tree was simplified to 255 segments and integrated into the lung geometry from the Visible Human Male for numerical simulations. Acoustic impedance boundary conditions were applied at the ends of the terminal segments to represent the unmodeled downstream airway segments. Experiments were also carried out on a preserved pig lung and similar trends of lung surface velocity distribution were observed between the experiments and simulations. This approach provides a feasible way of simplifying the airway tree and greatly reduces the computation time.

Acoustic Measurements of Sound Transmission in Human Subjects. Scanning laser Doppler vibrometry (SLDV) was used as a gold standard for transmitted sound measurements on a human subject. A low cost piezodisk sensor array was also constructed as an alternative to SLDV. The advantages and disadvantages of each technique are discussed.

CHAPTER 1

INTRODUCTION

1.1. Background and Motivation

Passive listening (auscultation) has been used qualitatively by physicians for hundreds of years to aid in the monitoring and diagnosis of a wide range of medical conditions, including those involving the pulmonary system (breath sounds), the cardiovascular system (e.g. heart sounds and bruits caused by partially occluded arteries and arteriovenous grafts) and the gastrointestinal system. There may be unique and diagnostically important information in audible frequency sound since characteristic times for many physiological processes and anatomical structural resonances are in that range [1, 2]. This approach offers several potential advantages including noninvasiveness, safety, availability, prompt results, and low cost, making it suitable for in-office check-ups, out-patient home monitoring, and field operations following natural or man-made catastrophes. Simple stethoscopic use is skill-dependent, provides qualitative rather than quantitative information at only a single location, and suffers from inherent limitations of human ability to discern certain acoustic differences. In recent years, many researchers have applied more quantitative measurement and analysis techniques to increase the diagnostic utility of this approach, utilizing electronic sensors and applying computational signal processing and statistical analyses to the measured signals to discern trends or biases correlated with pathologies [3-8].

Alterations in the structure and function of the pulmonary system that occur in disease or injury often give rise to measurable changes in lung sound production and transmission. Lung sounds are known to contain spatial information that can be accessed using simultaneous acoustic measurements at multiple locations. It has been shown that lung consolidation, pneumothorax, and airway obstruction, to name a few conditions, alter the production and/or transmission of sound with spectrally and regionally differing effects that, if properly quantified, might provide additional information about the severity and location of the trauma or pathology [3-6]. Indeed, simultaneous, multi-sensor auscultation methods have been developed to “map” sounds on the thoracic surface by several groups [5, 7-10], and in some cases to then

attempt to triangulate upon the interior location(s) of the sound sources by assuming that the sounds propagate away from the source with spherical symmetry in speed and attenuation [6].

1.2. Literature Review

Viscoelasticity of soft tissues and lung parenchyma. Soft biological tissues, including the lung, are known to be highly viscoelastic in nature. The lung exhibits creep and stress relaxation phenomenon. The viscoelasticity of lung tissue causes its dynamic elastic parameters to vary with frequency. Lung shear wave speed and attenuation at different frequencies are mainly affected by the lung tissue shear viscoelasticity. So, it is important to characterize the lung viscoelastic properties. An improved understanding of surface (Rayleigh) wave motion on viscoelastic soft tissue and lung is useful to identify their shear viscoelastic properties. In medical diagnostics research, linear surface and shear wave behavior – phase speed and attenuation rate – on and in soft biological tissues have been studied extensively as this behavior can be significantly altered by changes in the shear elasticity and viscosity of the tissue caused by various pathologies, trauma or remodeling [11-13]. For soft biological tissues (e.g. comparing muscle with fat), the X-ray attenuation coefficient varies only by a factor of two [14], while MR relaxation times vary by a factor of three [15]. The shear moduli, on the other hand, can vary by more than a factor of ten, potentially providing greater contrast [16-18].

A range of viscoelastic constitutive models have been proposed to interpret shear and surface wave measurements. These models attempt to relate measurable phenomena to the underlying elasticity and damping of the material, both of which are typically rate- (frequency-) dependent. Historically, many studies have often assumed a Voigt model of viscoelasticity. Recent studies have shown that such models have limitations in their ability to accurately capture dynamic phenomena over multiple time scales and/or with broad spectral content, particularly for biological tissues and tissue mimicking phantoms. One way to overcome such limitations is through the use of more complex models with a larger number of parameters to optimize; another approach is via fractional order models [19-23]. Fractional order viscoelastic models have shown the potential to yield new disease and treatment specific parameters that

more effectively predict underlying changes in tissue associated with developing pathology, such as liver cirrhosis and breast cancer.

Lung viscoelasticity has been extensively studied during the past few decades. Several groups studied the stress relaxation and the hysteretic properties of the lungs [24, 25], and an attempt to explain the results using spring-dashpot networks was given by Sharp et al. [26]. An extensive evaluation of lung viscoelasticity in human and in isolated cat lungs was presented by Hildebrandt [27] and Bachofen [28]. Suki et al. [29] used a fractional viscoelastic model to link lung viscoelasticity and its molecular basis. Zhang et al. [30] estimated the viscoelastic parameters of lung tissue with an assumed Voigt model by the surface wave method. Dai et al. [31] estimated the lung tissue viscoelastic parameters associated with different viscoelastic models by fitting the phase speed dispersion or by fitting the viscoelastic parameters estimated from surface wave measurements. Most of these studies reveal that the conventional Voigt model was not enough to represent the lung viscoelasticity.

Poroviscoelasticity modeling of wave propagation in the lung. The compression wave in the lung is very different from that in other human internal organs. For frequencies above 100 Hz and neglecting the larger segments of the bronchial airway tree, it has been proposed that parenchymal tissue can be modeled as a homogenous isotropic material supporting acoustic compression waves [32, 33]. The parenchymal region is defined by its density and a complex wave number, whose real part is linked to phase speed and whose imaginary part defines the attenuation. Compression wave numbers for the parenchymal material are quite different from those of the two components of which it is comprised, soft tissue and air; correspondingly, in the lung parenchyma sound travels much slower and attenuates rapidly. This approach is referred to as the effective medium theory which leads to a frequency independent compression wave speed. But recently it is reported that the compression wave speed changes with frequency from 500 to 5000 Hz [34]. Wodicka et al. [33] modeled the lung parenchyma as air bubbles (alveoli) in water (lung tissue) at low audible frequencies and proposed that the magnitude of thermal losses are theoretically much larger than those associated with scattering or viscous effects. The predicted

power spectra of acceleration at the human trachea and chest wall and the experimental measurements agreed well from 100 to 600 Hz, while the predicted attenuation has discrepancies with experimental measurements on the lung ex vivo, especially at frequencies above 600 Hz.

Biot theory [35, 36], which predicts the existence of two types of compression waves in fluid saturated porous media, has been widely used in many geophysical applications. Among biological tissues, the slow compression wave was first observed in water-saturated bovine plexiform and human Haversian bone in 1983 [37]. Since then there has been extensive research on ultrasonic wave propagation in human and bovine cortical and trabecular bones, also in both normal and cancellous bones [38, 39]. There have already been numerous studies on poroelastic and poroviscoelastic modeling of soft tissues. Mow et al. [40] first applied the biphasic theory to the articular cartilage which is a biphasic material composed of the solid matrix and interstitial fluid. General constitutive equations of the viscoelastic solid matrix and interstitial fluid were developed and applied to describe the experimentally obtained biphasic creep and stress relaxation data. Simon et al. [41, 42] proposed multiphase poroelastic finite element models for soft tissue structures and extended the model including transport and swelling in the tissue. Currently there have been limited studies on poroviscoelasticity modeling of lung acoustics. Siklosi et al. [43] modeled the lung parenchyma as a porous solid with air-filled pores by Biot theory as a model for its acoustic properties. The Biot theory yielded a frequency dependence of the speed of sound that was in qualitative agreement with the measurements.

Airway and lung acoustics modeling. In modeling the transmission of sound throughout the pulmonary system and chest region, the system may be viewed as having two main components:

- (1) transmission of sound through the tracheobronchial tree and,
- (2) coupling to and transmission through the surrounding biological tissues to reach the chest surface – namely the parenchyma, free air or water/blood region (in the case of a pneumothorax or hydro/hemothorax), surrounding muscle and rib cage regions, and outer soft tissues.

Many studies have focused on the transmission of sound in the respiratory tract, the tracheobronchial airway tree, with some also considering coupling to modes of wave propagation in the parenchyma [3, 4, 6, 44, 45]. Many have considered acoustic impedance of the tree, air excitation, and response measurement at the mouth or just below the glottis or some combination of these locations with and without endotracheal intubation, and/or resulting pressure distributions throughout the tree and parenchyma, itself. In these cases, it has been shown that a 1D branching waveguide representation of the trachea and bronchial airways with compliant walls reasonably approximates most of the dynamic behavior up to several kHz. At higher frequencies the 1D quasi-planar wave propagation assumption begins to lose validity in the larger airways. Also, from about 100 Hz to 10 kHz, wave propagation in the parenchyma away from the larger airways is reasonably approximated using a closed cell bubble swarm approach with gas elasticity and tissue density dominating. Below 100 Hz vibratory wave propagation in the parenchyma is more a function of the elastic and inertial properties of the solid tissue only and the acoustic response of the bronchial tree can be reasonably approximated as a capacitive load [10].

Transmission through the surrounding biological tissues to reach the chest surface has, arguably, received less attention. Previous studies of this part of the problem have assumed simplified geometries and homogenized material properties [33, 46, 47]. Wodicka et al. [33] assumed an axisymmetric cylindrical geometry, with the outer tissue regions of the chest treated simply as a mass load on the parenchyma. In Vovk et al. [46], an axisymmetric layered model for the torso region is used that includes annular regions for the parenchyma, rib cage region, soft outer tissue and skin. In Royston et al. [47], simplifications of both airway and tissue structures were imposed that resulted in an axisymmetric assumption or two-dimensional planar model assumption that could be easily handled with finite element analysis. The benefit of coupling an array measurement on the surface with an improved computational model of sound propagation within the torso was demonstrated fundamentally in Ozer et al. [48]. In phantom studies, it was shown that the use of a computational boundary element model of lung acoustics combined with a surface array measurement, was significantly superior in identifying the dominant source location of the sound as compared to a simple “ray acoustics” model that neglects the more complex

nature of sound transmission in a finite and complex dimensioned structure. In Acikgoz et al. [49] an acoustic boundary element model was used to simulate sound propagation in the lung parenchyma and surrounding chest wall. The simulations were compared with experimental studies on lung-chest phantom models that mimick the lung pathology of pneumothorax. Studies quantified the effect of the simulated lung pathology on the resulting acoustic field measured at the phantom chest surface. Wochner et al. [50] used a two-fold symmetric model to study lung response to underwater sound by the finite element method.

To model acoustic compression wave propagation in the surrounding tissues of the torso, the soft tissue regions composed of fat, muscle and connective / visceral material, can be defined by a density and a complex wave number. The shear wave is primarily governed by the density and the shear viscoelastic moduli. Shear wave lengths and propagation speeds at a given frequency are typically 3 orders of magnitude smaller than that of compression waves in the same soft tissue medium [51].

Acoustic measurements of sound transmission through the pulmonary system and torso. Mechanical compression waves (sound) travel in the lung much more slowly than in the air and soft tissue of which it is comprised; sound speed in the human lung [9, 10, 52, 53] and animal lung [32, 54-56] have been studied by several groups. In human studies, sound was usually introduced into the mouth; but, the sound speed range from each group has been very different. In animal studies, sound was usually applied to the lung surface. Sound speed ranges from all groups were fairly consistent even though the measurements were taken on different animals. Also, all these animal studies concluded that the sound speed depended on the lung volume as the lung volume change leads to the change of air volume fraction in the lung, thus affecting the sound speed. This is consistent with the theoretical prediction by the effective medium theory. Studies have also been carried out to estimate the attenuation associated with sound propagation through the parenchyma. Wodicka et al. [33] measured the power spectra of acceleration at the human trachea and chest wall and achieved good agreement between theoretical predictions and experimental

measurements from 100 to 600 Hz. Berger et al. [34] measured sound attenuation with respect to frequency in the isolated fetal lung at different inflation volumes.

To measure the response of the thorax to sonic perturbations of known input characteristics, a number of investigations have focused on the transmission of sound from introduction at the mouth to detection on the chest surface. In this manner, the static and even dynamic properties of the system can be measured and compared with model predictions and other hypotheses. Chest surface responses relative to a reference measurement over the extrathoracic trachea have been used to determine the amplitude and phase delay of transmission. The frequency-dependent decrease in amplitude agrees with models of the thorax that account for parenchymal losses [33, 46]. A strong spatial dependence of sound transmission from the mouth to the chest wall was reported by Kraman et al. [52, 57], and later confirmed by Wodicka et al. [58] and Pasterkamp et al. [44]. The changes in lung structure that occur in disease affect the amplitude and timing of sound transmission from the airways to the chest surface. In patients with emphysema [59] and in dogs with pneumothorax [3, 4], a decrease of transmitted amplitude at low frequencies was observed, which is qualitatively consistent with the common auscultatory finding of decreased lung sound intensity. In contrast, cardiogenic pulmonary edema was found to increase the amplitude of sound transmitted to the chest wall in dogs in a linear fashion over a wide frequency bandwidth relative to postmortem wet to dry weight ratios [60], a finding consistent with that of bronchial breathing heard over consolidated lung.

1.3. Research Objective

A long-term goal of the Audible Human Project (AHP) is to develop a computational acoustic model that would accurately simulate generation, transmission and noninvasive measurement of sound and vibration within the pulmonary system and torso caused by both internal (e.g. respiratory function) and external (e.g. palpation) sources. Benefits of the AHP are foreseen in terms of both enhanced medical education/training, and in catalyzing the development of improved diagnostic techniques. The goals of this dissertation research, fitting within the scope of the AHP, are to develop specific improved theoretical

understandings, computational models and experimental methods aimed at sound transmission and measurement. In order to achieve these goals, the following **specific aims** are undertaken:

- 1) Improve theoretical modeling and experimental identification of viscoelasticity in soft biological tissues.
- 2) Develop a poroviscoelastic model for lung tissue vibroacoustics.
- 3) Improve lung airway acoustics modeling and its coupling to the lung parenchyma.
- 4) Develop improved techniques in array acoustic measurement on the torso surface of sound transmitted through the pulmonary system and torso.

These proposed research developments are key components of the advancement of the **AHP**, which ultimately will simulate virtual patients with different pulmonary pathologies. In this dissertation improved theoretical modeling and experimental identification approaches of shear viscoelasticity will be explored. Biot theory will be applied to model the compression wave transmission in the lung. Measurements of compression wave speed and attenuation will be compared with Biot theory predictions. Due to the complexity of the bronchial airways, it is impossible to build an acoustic airway tree with millions of airway segments. The airway tree will be simplified to a network with upper large airways down to a few bifurcations from the trachea while mimicking the acoustic field of the original airway tree to the largest extent. The lung surface motion caused by airway insonification will be simulated by integrating the simplified airway tree into a real human lung geometry. Novel acoustic array measurements on human subjects will also be explored.

1.4. Dissertation Overview

The background, motivation and research objectives of this dissertation are presented in Chapter 1. The state of the art of research on related topics is also reviewed in Chapter 1. The four specific aims in the research objectives of this dissertation are presented in Chapters 2-5. Chapter 2 focuses on improved

theoretical modeling and experimental identification approaches of viscoelastic properties of the tissue-mimicking phantom and ex vivo lung based on surface wave measurements. Modeling lung parenchyma as a poroviscoelastic medium and exploring different wave types and their respective properties, including wave speed and attenuation, are presented in Chapter 3. Modeling of sound transmission in the airway tree and its coupling into the lung parenchyma are covered in Chapter 4. Experiments and simulations are performed on tissue mimicking phantoms. Then the computer generated airway tree was integrated into a real human lung geometry. Simulations on lung excitation through airway insonification were carried out and compared with SLDV measurements on a preserved pig lung. Improved techniques in array acoustic measurement on the torso surface of sound transmitted through the pulmonary system and torso are presented in Chapter 5. The sound transmission in a human subject is measured by the SLDV and piezodisk sensors and their comparisons are discussed. Chapter 6 summarizes the accomplishments of this dissertation and presents the topics for future research.

1.5. References

1. Pasterkamp H, Kraman SS, Wodicka, GR, 1997, Respiratory sounds-advances beyond the stethoscope, *Am. J. Respir. Crit. Care Med.* 156(3), pp. 974-987.
2. Sarvazyan AP, Rudenko OV, Swanson SD, Fowlkes JB, Emelianov SY, 1998, Shear wave elasticity imaging: a new ultrasonic technology of medical diagnostics, *Ultrasound in Med. & Biol.* 24, pp. 1419–1435.
3. Mansy HA, Balk R, Royston TJ, Sandler RH, 2002, Pneumothorax detection using pulmonary acoustic transmission measurements, *Med. Biol. Eng. Comput.* 40, pp. 520 – 525.
4. Mansy HA, Balk R, Royston TJ, Sandler RH, 2002, Pneumothorax detection using computerized analysis of breath sounds, *Med. Biol. Eng. Comput.* 40, pp. 526 – 532.
5. Pasterkamp H, Consunji-Araneta R, Oh Y, Holbrow J, 1997, Chest surface mapping of lung sounds during methacholine challenge, *Pediatric Pulmonology*, 23, pp. 21 – 30.

6. Kompis M, Pasterkamp H, Wodicka GR, 2001, Acoustic imaging of the human chest, *Chest*, 120, pp. 1309-1321.
7. Benedetto G, Dalmasso F, Spagnolo R, 1988, Surface distribution of crackling sounds, *IEEE Trans. Biomed. Eng.* 35, pp. 406-412.
8. Charleston-Villalobos S, Cortes-Rubiano S, Gonzalez-Camarena R, Chi-Lem G, and Aljama-Corrales T, 2004, Respiratory acoustic thoracic imaging (RATHI): assessing deterministic interpolation techniques, *Med. & Biol. Eng. & Comput.* 42, pp. 618-626.
9. Bergstresser T, Ofengeim D, Vyshedskiy A, Shane J, Murphy R, 2002, Sound transmission in the lung as a function of lung volume, *J. Appl. Physiol.* 93, pp. 667-674.
10. Paciej R, Vyshedskiy A, Shane J, Murphy R, 2003, Transpulmonary speed of sound input into the supraclavicular space, *J. Appl. Physiol.* 94, pp. 604-611.
11. Yamakoshi Y, Sato J, Sato T, 1990, Ultrasonic imaging of internal vibration of soft tissue under forced vibration, *IEEE Trans. Ultrason. Ferroelectr. Freq. Contr.* 37, pp. 45–53.
12. Muthupillai R, Lomas DJ, Rossman PJ, Greenleaf JF, Manduca A, Ehman, RL, 1995, Magnetic resonance elastography by direct visualization of propagating acoustic strain waves, *Science*, 269, pp. 1854–1857.
13. Zhang XM, Greenleaf JF, 2007, Estimation of tissue's elasticity with surface wave speed, *J. Acoust. Soc. Am.* 122, pp. 2522–2525.
14. Duck FA, 1990, *Physical properties of tissue: a comprehensive reference book*, Academic Press, New York, NY.
15. Kuperman V, 2000, *Magnetic resonance imaging: physical principles and applications*, Academic Press, New York.
16. Hoyt K, Kneezel T, Castaneda B, Parker KJ, 2008, Quantitative sonoelastography for the in vivo assessment of skeletal muscle viscoelasticity, *Phys. Med. Biol.* 53, pp. 4063–4080.

17. Fung YC, 1993, *Biomechanics: mechanical properties of living tissues*, 2nd Ed., Springer-Verlag, New York.
18. Sarvazyan AP, Rudenko OV, Swanson SD, Fowlkes JB, Emelianov SY, 1998, Shear wave elasticity imaging: a new ultrasonic technology of medical diagnostics, *Ultrasound in Med. & Biol.* 24, pp. 1419–1435.
19. Chan RW, Titze IR, 2003, Effect of postmortem changes and freezing on the viscoelastic properties of vocal fold tissues, *Ann. Biomed. Eng.* 31, pp. 482–491.
20. Craiem D, Armentano R, 2007, A fractional derivative model to describe arterial viscoelasticity, *Biorheol.* 44, pp. 251–263.
21. Kiss MZ, Varghese T, Hall TJ, 2004, Viscoelastic characterization of in vitro canine tissue, *Phys. Med. Biol.* 49, pp. 4207–4218.
22. Klatt D, Hamhaber U, Asbach P, Braun J, Sack I, 2007, Noninvasive assessment of the rheological behavior of human organs using multifrequency MR elastography: a study of brain and liver viscoelasticity, *Phys. Med. Biol.* 52, pp. 7281–7294.
23. Riek K, Klatt D, Nuzha H, Mueller S, Neumann U, Sack I, Braun J, 2011, Wide-range dynamic magnetic resonance elastography, *J. Biomech. Eng.* 44, pp. 1380–1386.
24. Marshall R, Widdicombe JG, 1960, Stress relaxation of the human lung, *Clin. Sci. Lond.* 20, pp. 19–31.
25. Saibene F, Mead J, 1969, Frequency dependence of pulmonary quasi-static hysteresis, *J. Appl. Physiol.* 26, pp. 732–737.
26. Sharp JT, Johnson FN, Goldberg NB, Van Lith P, 1967, Hysteresis and stress adaptation in the human respiratory system, *J. Appl. Physiol.* 23, pp. 487–497.
27. Hildebrandt J, 1970, Pressure-volume data of cat lung interpreted by a plastoelastic, linear viscoelastic model, *J. Appl. Physiol.* 28, pp. 365–372.
28. Bachofen H, 1968, Lung tissue resistance and pulmonary hysteresis, *J. Appl. Physiol.* 24, pp. 296–301.

29. Suki B, Barabasi AL, Lutchen KR, 1994, Lung tissue viscoelasticity: a mathematical framework and its molecular basis, *J. Appl. Physiol.* 76, pp. 2749-2759.
30. Zhang XM, Qiang B, Urban MW, Kinnick R, Hubmayr R, Greenleaf JF, 2009, Quantitative surface wave method for measuring local viscoelasticity of lungs, *IEEE International Ultrasonics Symposium Proceedings*, pp.479-482.
31. Dai Z, Peng Y, Mansy HA, Royston TJ, Sandler RH, 2011, Estimation of local viscoelasticity of lungs based on surface waves, *ASME IMECE* (November 11 – 17, 2011, Denver, CO).
32. Rice DA, 1983, Sound speed in pulmonary parenchyma, *J. Appl. Physiol.* 54, pp. 304–308.
33. Wodicka GR, Stevens KN, Golub HL, Cravalho EG, Shannon DC, 1989, A model of acoustic transmission in the respiratory system, *IEEE Trans. Biomed. Eng.* 36, pp. 925 – 34.
34. Berger PJ, Skuza EM, Ramsden CA, Wilkinson MH, 2005, Velocity and attenuation of sound in the isolated fetal lung as it is expanded with air, *J. Appl. Physiol.* 98(6), pp. 2235-2241.
35. Biot MA, 1956, Theory of propagation of elastic waves in a fluid saturated porous solid. I Low frequency range, *J. Acous. Soc. Amer.* 28(2), pp. 168-178.
36. Biot MA, 1956, Theory of propagation of elastic waves in a fluid saturated porous solid. II Higher frequency range, *J. Acous. Soc. Amer.* 28(2), pp. 179-191.
37. Lakes R, Yoon HS, Katz JL, 1983, Slow compressional wave propagation in wet human and bovine cortical bone, *Science*, 220(4596), pp. 513-515.
38. Hosokawa A, Otani T, 1997, Ultrasonic wave propagation in bovine cancellous bone, *J. Acoust. Soc. Am.* 101(1), pp. 558-562.
39. Williams JL, 1992, Ultrasonic wave propagation in cancellous and cortical bone: prediction of some experimental results by Biot's theory, *J. Acoust. Soc. Am.* 91(2), pp. 1106-1112.
40. Mow VC, Kuei SC, Lai WM, Armstrong CG, 1980, Biphasic creep and stress relaxation of articular cartilage in compression: theory and experiments, *J. Biomech. Eng.* 102(1), pp. 73-84.
41. Simon BR, 1992, Multiphase poroelastic finite element models for soft tissue structures, *Appl. Mech. Rev.* 45, pp. 191-218.

42. Simon BR, Liable JP, Pflaster D, Yuan Y, Krag MH, 1996, A poroelastic finite element formulation including transport and swelling in soft tissue structures, *J. Biomech. Eng.* 118, pp. 1-9.
43. Siklosi M, Jensen OE, Tew RH, Logg A, 2008, Multiscale modeling of the acoustic properties of lung parenchyma, *ESAIM: Proc.* 23, pp. 78-97.
44. Pasterkamp H, Patel S, Wodicka GR, 1997, Asymmetry of respiratory sounds and thoracic transmission, *Med. Biol. Eng. Comput.* 35, pp. 103–106.
45. Ionescu CM, Muntean I, Tenreiro-Machado JA, De Keyser R, Abrudean M, 2010, A theoretical study on modeling the respiratory tract with ladder networks by means of intrinsic fractal geometry, *IEEE Trans. Biomed. Eng.* 57(2), pp. 246-253.
46. Vovk IV, Grinchenko VT, Oleinik VN, 1995, Modeling the acoustic properties of the chest and measuring breath sounds, *Acous. Phys.* 41, pp. 667 – 76.
47. Royston TJ, Zhang X, Mansy HA, Sandler RH, 2002, Modeling sound transmission through the pulmonary system and chest with application to diagnosis of a collapsed lung, *J. Acous. Soc. Amer.* 111, pp. 1931 – 1946.
48. Ozer MB, Acikgoz S, Royston TJ, Mansy HA, Sandler RH, 2007, Boundary element model for simulating sound propagation and source localization within the lungs, *J. Acous. Soc. Amer.* 122 (1), pp. 657 – 671.
49. Acikgoz S, Ozer MB, Royston TJ, Mansy HA, Sandler RH, 2008, Experimental and computational models for simulating sound propagation within the lungs, *ASME J. Vib. & Acous.* 130 (2), pp. 021010-1 – 021010-10.
50. Wochner MS, Ilinskii YA, Hamilton MF, Zabolotskaya EA, 2009, Model for fatigue and failure of human lung tissue subjected to low-frequency underwater sound, *Underwater Acoustics Measurements: Technologies and Results 2009 conference*, Nafplion, Greece.
51. Royston TJ, Yazicioglu Y, Loth F, 2003, Surface response of a viscoelastic medium to subsurface acoustic sources with application to medical diagnosis, *J. Acous. Soc. Amer.* 113, pp. 1109 – 1121.

52. Kraman SS, Austrheim O, 1983, Comparison of lung sound and transmitted sound amplitude in normal men, *Am. Rev. Respir. Dis.* 128, pp. 451–454.
53. Mahagnah M, Gavriely N, 1995, Gas density does not affect pulmonary acoustic transmission in normal men, *J. Appl. Physiol.* 78, pp. 928–937.
54. Jahed M, Lai-Fook SJ, Bhagat PK, Kraman SS, 1989, Propagation of stress waves in inflated sheep lungs, *J. Appl. Physiol.* 66, pp. 2675–2680.
55. Jahed M, Lai-Fook SJ, 1994, Stress wave velocity measured in intact pig lungs with cross-spectral analysis, *J. Appl. Physiol.* 76, pp. 565–571.
56. Yen RT, Fung YC, Ho HH, Butterman G, 1986, Speed of stress wave propagation in lung, *J. Appl. Physiol.* 61, pp. 701–705.
57. Kraman SS, Bohadana AB, 1989, Transmission to the chest of sound introduced at the mouth, *J. Appl. Physiol.* 66, pp. 278–281.
58. Wodicka GR, DeFrain PD, Kraman SS, 1994, Bilateral asymmetry of respiratory acoustic transmission, *Med. Biol. Eng. Comput.* 32, pp. 489–494.
59. Böhme HR, Böhme H, 1972, Variable low-frequency sound conduction of the lung in pulmonary emphysema, *Z. Gesamte Inn. Med.* 27, pp. 765–770.
60. Donnerberg RL, Druzgalski CK, Hamlin RL, Davis GL, Campbell RM, Rice DA, 1980, Sound transfer function of the congested canine lung, *Br. J. Dis. Chest*, 74, pp. 23–31.

CHAPTER 2

LUNG TISSUE VISCOELASTICITY

2.1. Introduction

Like most other biological soft tissues, the lung is viscoelastic as it exhibits creep, stress relaxation and hysteresis, so it has the properties of both viscous and elastic materials. The two major wave types propagating in the lung are the compression and the shear wave. The shear wave speed and attenuation at different frequencies are mainly affected by the lung tissue shear viscoelasticity. The mechanical properties of lung tissue are of interest in medicine as they have been shown to be affected by various pathologies, including interstitial lung diseases, such as pulmonary fibrosis. Identifying the mechanical properties of lung tissue first requires a means of quantitatively measuring phenomena that are affected by these properties. One approach to measure tissue mechanical properties is by mechanical wave motion [1]. It also is of benefit to have appropriate constitutive models that lead to an accurate simulation of dynamic behavior over as wide of spatial and temporal scales as possible using the least number of modeling parameters. Both internal (shear) and surface wave motion are currently being used by several groups to study lung mechanical properties [1].

An improved understanding of surface (Rayleigh) wave motion on a viscoelastic material is essential to developments in many areas including medicine, geophysics, infrastructure and manufacturing. For example, in medical diagnostics research, linear surface and shear wave behavior – phase speed and attenuation rate – on and in soft biological tissues have been studied extensively as this behavior can be significantly altered by changes in the shear elasticity and viscosity of the tissue caused by various pathologies, trauma or remodeling [2-4]. For soft biological tissues (e.g. comparing muscle with fat), the X-ray attenuation coefficient varies only by a factor of two [5], while MR relaxation times vary by a factor of three [6]. The shear moduli, on the other hand, can vary by more than a factor of ten, potentially providing greater contrast [7-9].

A range of viscoelastic constitutive models have been proposed to interpret shear and surface wave measurements. These models attempt to relate measurable phenomena to the underlying elasticity

and damping of the material, both of which are typically rate- (frequency-) dependent. Historically, many studies have often assumed a Voigt model of viscoelasticity. Recent studies have shown that such models have limitations in their ability to accurately capture dynamic phenomena over multiple time scales and/or with broad spectral content, particularly for biological tissues and tissue mimicking phantoms. One way to overcome such limitations is through the use of more complex models with a larger number of parameters to optimize; another approach is via fractional order models [10-15]. Fractional order viscoelastic models have shown the potential to yield new disease and treatment specific parameters that more effectively predict underlying changes in tissue associated with developing pathology, such as liver cirrhosis and breast cancer. As an example, in Sinkus et al. [15] a relatively simple power law relationship was fit to the complex shear modulus of human breast tissue and tumors measured by magnetic resonance elastography. The results, when plotted as the fractional power exponent versus the fractional order attenuation, separated benign from malignant tumors with an increase in specificity and sensitivity.

In Royston et al. [16, 17] there has been an emphasis on understanding the surface wave field created in a material like biological tissue by canonical vibratory sources. The improved solution was tested experimentally using a viscoelastic phantom with material properties comparable to biological soft tissue. Some agreement could be achieved over a limited frequency range (20 – 100 Hz) using a Voigt model. In a more recent study revisiting the same canonical system on a different phantom material it appeared that an improved match could be achieved over a broader frequency range by using a fractional order viscoelastic model [18]. In this chapter of the dissertation two experimental identification approaches of shear viscoelasticity are explored. The first approach is to directly estimate the frequency-dependent surface (Rayleigh) wave speed from experimental data and then to optimize the coefficients in an assumed viscoelastic model type to minimize the difference between the measured and predicted values of wave speed [1, 4, 19, 20]. In an analogous manner, shear wave speed dispersion derived from elastography techniques has been used to estimate the shear viscoelasticity with an assumed viscoelastic model type [21-26]. The second approach is to measure the complex-valued frequency response function (FRF) between the excitation location and points at known radial distances from the excitation location.

The FRF has embedded in it frequency-dependent information about both surface wave phase speed and attenuation that can be used to directly estimate the real and imaginary parts of the complex shear modulus (storage and loss shear moduli). The coefficients in an assumed viscoelastic tissue model type can then be optimized to minimize the differences in the predicted and experimentally determined values of the complex shear modulus. The relative merits of these approaches are explored theoretically, computationally and experimentally on a tissue-mimicking phantom and evaluated experimentally on excised pig lungs.

2.2. Theory

2.2.1 Viscoelastic Continuum: Equation of Motion

For an isotropic, homogenous, viscoelastic compressible medium one can use the following formulation of the equation of motion for small perturbations about an operating point

$$(\lambda + \mu) \nabla \nabla \cdot \mathbf{u} + \mu \nabla^2 \mathbf{u} = \rho \frac{\partial^2 \mathbf{u}}{\partial t^2}. \quad (2.1)$$

Here, \mathbf{u} is the displacement vector, ρ is the density of the medium, $\partial/\partial t$ denotes a derivative with respect to time, ∇ is the spatial Laplacian operator dependent upon the chosen coordinate system, and λ and μ are the Lamé constants of the medium. For a linear viscoelastic Voigt material model, the rate-dependent Lamé “constants” are expressible as $\lambda(t) = \lambda_0 + \lambda_1 \partial/\partial t$ and $\mu(t) = \mu_0 + \mu_1 \partial/\partial t$ where λ_0 , λ_1 , μ_0 and μ_1 are coefficients of volume compressibility, volume viscosity, shear elasticity and shear viscosity, respectively [27]. Other shear viscoelastic models will lead to different rate-dependence relations.

With regard to μ , it has been observed in many materials that the simple two-element Voigt model for shear viscoelasticity (μ_0 , μ_1) does not accurately capture material shear dynamic behavior, in terms of its experimentally-measured response to various elementary excitation waveforms, such as step inputs or periodic or random inputs with broad spectral content. More complex arrangements of multiple elastic (springs) and viscous (dashpot) components may then be employed empirically in order to more

closely match what is observed. For example, the Standard Linear Solid (SLS) Model, also known as the Kelvin or Zener model, consists of a parallel combination of a Maxwell element (spring and dashpot in series) with a spring. The three-element SLS model has more flexibility in representing dynamic viscoelasticity as compared to the Voigt model. Instead of increasing the constitutive model complexity by increasing the number of components that comprise it, an alternative is to consider that the material may exhibit rate-dependent shear deformation that is best described by a single element, comprised of two constants, μ_α and α , whose behavior lies somewhere between Hookean solid and Newtonian fluid. Specifically, fractional order viscoelasticity (a springpot) can be specified as shown in the second term of the following:

$$\mu = \mu_0 + \mu_\alpha \frac{\partial^\alpha}{\partial t^\alpha}, \quad 0 < \alpha \leq 1. \quad (2.2)$$

Equation (2.2) is referred to as a fractional order Voigt model for $\alpha < 1$. While such a mathematical construction may seem to lack physical meaning, it can be shown that this type of relation results asymptotically when using a ladder-like fractal arrangement of integer-order elastic and viscous components, as depicted in Figure 2.1 [28]. Indeed, such an arrangement might be rationalized on the grounds that it represents multiscale rate-dependent stress-strain interactions that one would inherently expect in some materials with complex multiscale cellular and extracellular structure, such as biological tissues. Furthermore, suitably defined fractional derivatives do not pose significant difficulty mathematically for well-conditioned functions. (Here we have chosen to use the Weyl definition of the fractional order derivative, which for harmonic functions such as $f(t) = e^{j\omega t}$, has the property that $\partial^\alpha / \partial t^\alpha [e^{j\omega t}] = (j\omega)^\alpha e^{j\omega t}$.) The expression in Equation (2.2) is still linear in nature and thus all rules and techniques afforded such relations, such as the validity of superposition, reciprocity, the Laplace and Fourier transforms, with associated transfer and frequency response functions, are all still valid [28-31]. In the Laplace (s) and frequency ($j\omega$) domains where $j = \sqrt{-1}$ and ω is the circular frequency, Equation (2.2) respectively becomes

$$\mu = \mu_0 + \mu_\alpha(s)^\alpha, \quad \mu = \mu_0 + \mu_\alpha(j\omega)^\alpha. \quad (2.3a-b)$$



Figure 2.1 A tree arrangement of springs and dashpots (left) resulting in a fractional order element, called a springpot (middle). Schematic representation of a fractional order Voigt model (right); the dashpot is replaced with a springpot.

Note, a significant attribute of such fractional representations is that the temporal response takes on characteristics of power-law behavior as opposed to the exponential response that one obtains with the conventional Voigt representation. A power-law response in fact has been observed in a number of biological and nonbiological materials, further motivating this type of model [11, 12].

When a viscoelastic body is suddenly strained and then the strain is maintained constant afterward, the corresponding stresses induced in the viscoelastic body decrease with time. This phenomenon is called stress relaxation. Most mechanical models used to describe the viscoelastic behavior of materials are composed of combinations of linear springs and dashpots. In stress relaxation, as $t \rightarrow \infty$, the dashpot is completely relaxed and the load-deflection relation becomes that of the springs, as characterized by the constant which is called the relaxed elastic modulus [8]. The relaxed elastic modulus is denoted by μ_0 for each viscoelastic model in Figure 2.2.

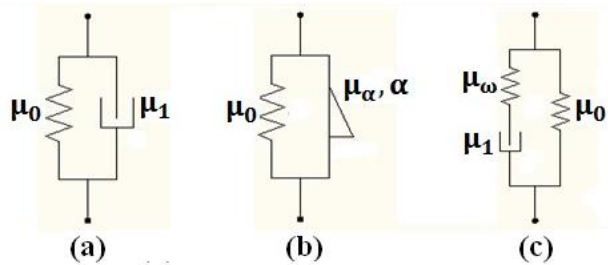


Figure 2.2 Different viscoelastic models: (a) Voigt (b) Fractional Voigt (c) Standard Linear Solid (SLS).

In the frequency domain, we have $\mu(\omega) = \mu_R(\omega) + j\mu_I(\omega)$ (storage and loss shear moduli) and both μ_R and μ_I are independent of whether the time derivative part of the Voigt model is of integer or

fractional order. They are equal to μ_0 and $\omega\mu_1$, shear elasticity and shear viscosity multiplied with circular frequency, if a conventional integer order Voigt model is used. In the case of a fractional order Voigt model since $(j\omega)^\alpha = \omega^\alpha(\cos[\alpha\pi/2] + j\sin[\alpha\pi/2])$ the storage modulus and loss modulus are defined, respectively, as

$$\mu_R = \mu_0 + \mu_\alpha \omega^\alpha \cos\left(\frac{\pi}{2}\alpha\right), \quad \mu_I = \mu_\alpha \omega^\alpha \sin\left(\frac{\pi}{2}\alpha\right). \quad (2.4a-b)$$

Alternatively, from Figure 2.2 (c) the SLS model yields:

$$\mu_R = \frac{\mu_0 \mu_\omega^2 + \omega^2 \mu_1^2 (\mu_0 + \mu_\omega)}{\mu_\omega^2 + \omega^2 \mu_1^2}, \quad \mu_I = \frac{\omega \mu_\omega^2 \mu_1}{\mu_\omega^2 + \omega^2 \mu_1^2}. \quad (2.5a-b)$$

Here μ_0 denotes the relaxed stiffness (relaxed elastic modulus), μ_1 denotes the viscous damping coefficient multiplied with the first order time derivative of the displacement (thus α is equal to 1), and μ_ω denotes the dynamic stiffness, which is only effective when the loading has a non-zero time derivative.

Regardless of whether an “integer order” or fractional order Voigt model or a Standard Linear Solid model is used, wave motion in the infinite 3-dimensional viscoelastic medium consists of a superposition of dilatational and shear wave displacements, $\mathbf{u} = \mathbf{u}_P + \mathbf{u}_S$, respectively. For the semi-infinite halfspace problem an additional surface (Rayleigh) wave \mathbf{u}_{Su} will exist.

2.2.2. Relaxed Elastic Moduli Estimation of Viscoelastic Medium by Indentation

The relaxed shear modulus μ_0 of the viscoelastic medium can be measured by indenting a rod with a spherical or cylindrical end into the medium and calculated from the indentation depth into the medium and the indentation force measured at the time when the viscous components (dashpots) in the viscoelastic medium are relaxed. Indenting a spherical-ended rod into an elastic half-space is assumed to be a Hertzian contact problem and the solution is given by Timoshenko [32]

$$a = \sqrt[3]{\frac{9\pi^2}{16} \frac{P^2 (k_1 + k_2)^2 (R_1 + R_2)}{R_1 R_2}}, \quad (2.6)$$

where

$$k_i = \frac{1 - \nu_i^2}{\pi E_i}, i = 1, 2. \quad (2.7)$$

Here, P is the indentation force, E_i and ν_i are the relaxed Young's modulus and Poisson's ratio, respectively, of the two materials in contact, a is the indentation depth, R_1 and R_2 are the radii of two spherical bodies; in our case one of the bodies was an infinite half-space, yielding $R_1 = \infty$. Also the indenter is so stiff compared to the medium being indented that $E_2 = \infty$. With these assumptions, from Equation (2.6) the relaxed Young's modulus of the medium can be simplified as

$$E_1 = \sqrt{\frac{9}{16} \frac{P^2 (1 - \nu_1^2)^2}{a^3 R_2}}. \quad (2.8)$$

The bulk modulus of the medium is also related to the relaxed Young's modulus and Poisson's ratio by

$$K_1 = \frac{E_1}{3(1 - 2\nu_1)}. \quad (2.9)$$

For most human soft tissues, its bulk modulus is reported to be very close to that of the water, $2.2 \times 10^9 Pa$. So with Equations (2.8) and (2.9) the relaxed Young's modulus and Poisson's ratio of the soft tissue can be calculated. The bulk modulus of the lung is about four times of order smaller than that of the water due to the presence of air in the lung and it also depends on the air volume fraction in the lung. While the Poisson's ratio of the lung changes very little with the air volume fraction and it is round 0.42 [33]. So the relaxed Young's modulus of the lung can be calculated from Equation (2.8). Finally the relaxed shear modulus of the soft tissue or the lung can be obtained by

$$\mu_0 = \frac{E_1}{2(1 + \nu_1)}. \quad (2.10)$$

When a rigid cylindrical indenter indents into a viscoelastic half-space, the relaxed Young's modulus is given by

$$E_1 = \frac{P(1 - \nu_1^2)}{2R_2 a}. \quad (2.11)$$

where R_2 is the radius of the cylindrical indenter. Similarly the relaxed shear modulus of the soft tissue or the lung can be estimated by the method mentioned above.

2.2.3. Surface Wave Propagation on a Half-Space due to a Surface Source

In Royston et al. [16], a simplified analytical solution was derived for Rayleigh wave propagation on the surface of an isotropic homogeneous viscoelastic half-space caused by normal force excitation over a circular region of radius “ a ” on the surface of amplitude per unit area P_{in} with harmonic time dependence $e^{j\omega t}$ as depicted in Figure 2.3. The analytical solution is

$$\frac{u_z}{P_{in}} = -\frac{2a}{\mu} \frac{J_1(pak_p) \sqrt{p^2 - 1}}{F'_o(-p)} \eta^2 K_0(jprk_p) e^{j\omega t}, \quad (2.12a)$$

where

$$F'_o(-p) = \left. \frac{\partial F_o}{\partial \zeta} \right|_{\zeta=-p}, \quad F_o(\zeta) = (2\zeta^2 - \eta^2)^2 - 4\zeta^2 \sqrt{\zeta^2 - \eta^2} \sqrt{\zeta^2 - 1}, \quad (2.12b-c)$$

$$\eta = \sqrt{(\lambda + 2\mu)/\mu}, \quad k_p = \omega \sqrt{\rho/(\lambda + 2\mu)}. \quad (2.12d-e)$$

Here, u_z is out-of-plane surface displacement, p is the ratio of compression wave speed to surface wave speed and is a root of the function F_o that is associated with Rayleigh wave motion, k_p is the compression wave number, r is the radial distance from center of the driving disk, J_1 is the Bessel function of the first kind (order 1), and K_0 is the modified Bessel function of the second kind (order 0); K_0 can also be written in terms of Bessel functions of the first and second kind (order 0) such as

$$K_0(x) = \frac{\pi}{2} j \{ J_0(jx) + jY_0(jx) \}. \quad \text{Equation (2.12c) links compression, shear and surface wave}$$

behavior to material viscoelastic properties; the roots of this equation yield compression, shear and surface wave numbers, which are complex-valued for a viscoelastic material, due to its rate-dependent stress-strain behavior.

Shear wave speed at frequency ω , given by $\omega/\text{Re}[k_s]$ where $k_s = \omega/c_s$ is the complex valued shear wave number, is related to the real (storage) and imaginary (loss) parts of the shear modulus, μ_R and μ_I , respectively, and the material density ρ as

$$\frac{\omega}{\text{Re}[k_s]} = \sqrt{\frac{2}{\rho} \frac{\mu_R^2 + \mu_I^2}{\mu_R + \sqrt{\mu_R^2 + \mu_I^2}}} . \quad (2.13)$$

Complex-valued surface (Rayleigh) wave number k_{Su} can be related to k_s through the following

$$k_{Su} = k_s \frac{p}{\eta} . \quad (2.14)$$

In soft biological tissues, or cases where $|\lambda| \gg |\mu|$ we have $|\eta/p| \approx 0.955$; but, due to the dispersive nature of viscoelastic materials there can be some slight variation of this ratio with frequency.

Note, the solution provided in equation (2.12a) [16], derived from the seminal works of Miller and Pursey [34, 35] indicates that only Rayleigh waves are present on the surface of the half space in the steady state. However, other theoretical treatments have indicated that effects from compression and shear waves can also be felt at the surface via “head waves”, at least under transient excitation conditions [36-38]. Given that all of this is linear system theory, it stands to reason that even in the steady state the effect of these head waves should be present, which may complicate the following analysis.

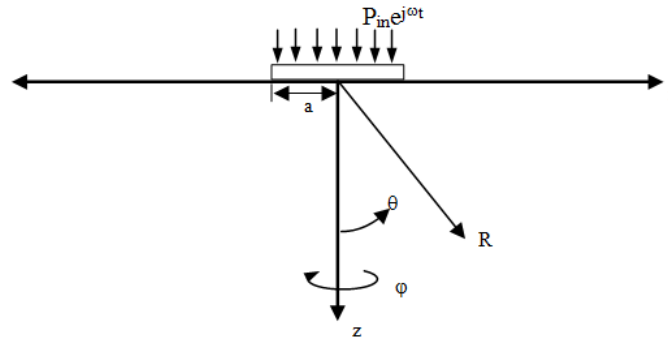


Figure 2.3 Ideal viscoelastic halfspace with finite surface source.

2.2.4. Viscoelasticity Estimation from Surface Wave Measurements

Approach 1: Measurement of surface wave speed as a function of frequency

The Rayleigh wave speed can be estimated from experimental measurements of the response to normal excitation as described in Section 2.2.3,

$$c_{Su} = \frac{\omega}{Re[k_{Su}]} = \omega |\Delta r / \Delta \phi|, \quad (2.15)$$

where Δr is the distance of two measuring positions along a radial line away from the source of surface waves, $\Delta \phi$ is the wave phase change over this distance, and ω is the circular frequency in radians/second. Having measured phase speed at multiple frequencies via this approach, assuming $|p/\eta| = 1.05$, and by assuming a specific viscoelastic model type that expresses $\mu_R(\omega)$ and $\mu_I(\omega)$ in terms of unknown coefficients, one can then use Equation (2.13) to optimize the values of these unknown coefficients to minimize the least square error between measured c_{Su} and calculated c_{Su} . Given the nonlinear dependence of the value in Equation (2.13) with respect to $\mu_R(\omega)$ and $\mu_I(\omega)$ it is expected that multiple local optima may exist and care must be taken in terms of an initial guess in the optimization routine. Theoretical, numerical and experimental example cases applications of this approach are described in the following sections below.

Approach 2: Measurement of the frequency response function

Measurement of the complex-valued frequency response function (FRF) between the driven oscillating disk and normal motion at a radial distance r from the center of the disk is accomplished as described in Section 2.3.3 below. Referring to Equation (2.12) and taking the ratio of the motion at the radial location r to that on the disk at radial location “ a ”, we have

$$FRF = \frac{u_z(r)}{u_z(a)} = \frac{K_0(jprk_p)}{K_0(jpak_p)} = \frac{K_0(jrk_{Su})}{K_0(jak_{Su})}. \quad (2.16)$$

Note, under the assumption that $|jak_{Su}| \gg 1/4$ and using Bessel function asymptotic limits we have that

$$FRF = \frac{u_z(r)}{u_z(a)} \approx \sqrt{\frac{a}{r}} e^{jk_{Su}(a-r)}. \quad (2.17)$$

Asymptotic Equation (2.17) clearly shows the geometric attenuation of the ratio of displacement amplitudes depending on radial distance r raised to the half power. Attenuation due to viscosity will manifest in the imaginary part of k_{su} . In Approach 2, the real and imaginary part of measured FRF (produced analytically, numerically or experimentally) are fit with Equation (2.16) in a least square error sense. First p is calculated from the fitting. From Equation (2.12c) η is solved. Multiple solutions exist in Equation (2.12c), but the only η that makes sense is the one whose real part is slightly smaller in amplitude than that of p as the surface wave speed is a slightly less than the shear wave speed. The complex shear modulus is calculated from Equation (2.12d). Finally, the viscoelastic parameters (except for the relaxed shear modulus μ_0 for each model assumed to be measured) are estimated by fitting μ_R , μ_I/ω based on the assumed viscoelastic model, such as fractional Voigt – Equations (2.4a-b), or SLS – Equations (2.5a-b). Here, μ_I/ω is listed instead of μ_I as a way to quickly assess the appropriateness of the integer Voigt model (μ_I/ω independent of frequency). μ_0 is chosen to be the actual value used in the analytical or numerical study and it is measured in the experimental study. Theoretical, computational and experimental example cases studies are described in the sections below.

Initial Comparison of Approaches 1 and 2.

The inherent difference between the two approaches described above is that, while Approach 1 only uses the measured surface wave speed as a function of frequency, Approach 2 effectively uses both the surface wave speed and attenuation as a function of frequency. Thus, one may expect that Approach 2 will provide more information in terms of both helping to determine the appropriate viscoelastic model type, as well as the optimal coefficient values for that type. However, in terms of practical implementation, it may be more difficult to acquire accurate measurements of attenuation, especially given that the above analyses are predicated on the fictional notion of an infinite half-space. Actual applications will involve finite boundaries, and the possibility of the contamination of the FRF with other wave types, e.g. compression waves, and multi-path reflections. Of course, these complexities may also

affect the accuracy of Approach 1.

2.3. Viscoelasticity Identification of a Tissue-Mimicking Phantom

2.3.1. Analytical Case Studies

With each of the material cases depicted in Table 2.1, consider a half-space of a linear viscoelastic isotropic material with density $\rho = 1,000 \text{ kg/m}^3$. Consider that surface wave excitation is initiated via a disk of radius $a = 1 \text{ cm}$ over the frequency range of 100 to 600 Hz and that phase speed is determined per Equation (2.15) and the FRF is determined per Equation (2.16). The FRF is plotted for two frequencies in Figure 2.4. Approaches 1 and 2 of the previous section are used to identify the optimal coefficients for an assumed viscoelastic model using response data at eleven frequencies spaced in 50 Hz increments from 100 to 600 Hz.

Specifically, *per Approach 1*, it is assumed that μ_0 is already known from the indentation measurement. Using Equation (2.13) and assuming a Voigt model, in MATLAB the `createOptimProblem` and `GlobalSearch` commands are used to optimize the estimate of μ_l to minimize the error between measured and calculated phase speeds in a least square error sense (summing the squares of the difference between the calculated and measured phase speed at each frequency). This processing is then repeated, but instead assuming a Fractional Voigt model or a SLS model. In the case of the Fractional Voigt model, estimates of α and μ_α are optimized. For the SLS model assumption, estimates of μ_ω and μ_l are optimized.

Table 2.1 Viscoelastic material models used in analytical and numerical case studies

	Voigt ($\alpha = 1$)	Fractional Voigt	SLS ($\alpha = 1$)
μ_0 (kPa)	23.9	14.0	14.0
μ_α (Pa.s $^\alpha$)	6.60	140	12.0
	—	$\alpha = 0.60$	$\mu_\omega = 16.0 \text{ kPa}$

Per **Approach 2**, it is also assumed that μ_0 is already known from the indentation measurement. First assuming a Voigt model, the same MATLAB commands are used to optimize an estimate of μ_l to minimize the error between measured and calculated $\mu_R(\omega)$ and $\mu_l(\omega)/\omega$ (summing the squares of the difference between the calculated and measured values of $\mu_R(\omega)$ and $\mu_l(\omega)/\omega$). In the case of the Fractional Voigt model, estimates of α and μ_α are optimized. Finally estimates of μ_ω and μ_l are optimized for the SLS model assumption.

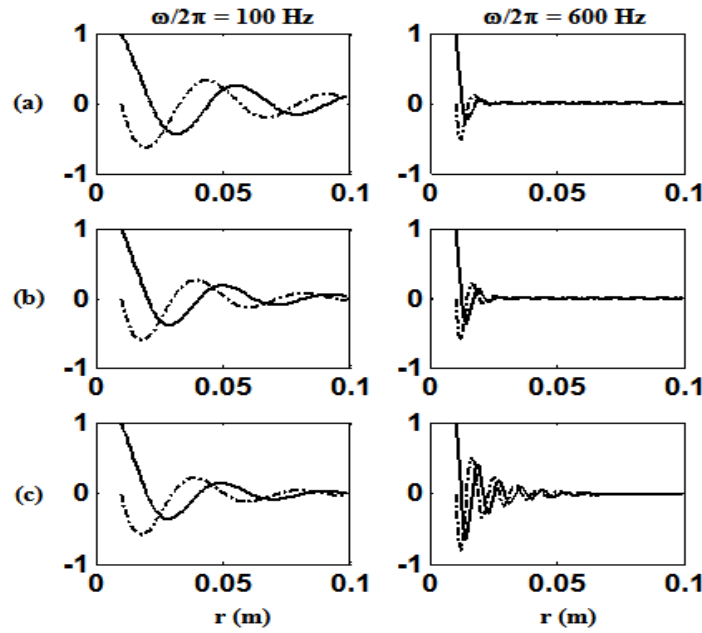


Figure 2.4 Theoretical studies. FRF at $\omega/2\pi = 100$ and 600 Hz for (a) Voigt, (b) fractional Voigt, and (c) SLS material studies. Key: — Real part, - • - Imaginary part. Material property values given in Table 2.1.

Results of the best fits using Approaches 1 and 2 are provided in Table 2.2 and in Figures 2.5 – 2.7. Referring to Table 2.2, it is seen that Approach 2 generally outperforms Approach 1, minimizing error to machine tolerance when the appropriate model type is selected. It may also be observed from the figures that, generally, being able to compare estimates of $\mu_R(\omega)$ and $\mu_l(\omega)/\omega$ to measured values more clearly identifies which viscoelastic model type is appropriate, relative to comparing estimates of phase speed to measured values. (Note, for the Voigt material model, Approach 2 correctly drives the fractional Voigt and SLS models to that of a Voigt model by driving α to 1 and μ_ω to the upper limit allowed in the

optimization routine, respectively.)

Table 2.2 Estimated viscoelastic coefficients and residual error in analytical case studies

Approach 1						Approach 2					
Residual Error ($\times 10^3$)						Residual Error ($\times 10^3$)					
μ_R μ_I μ						μ_R μ_I μ					
Actual material: Voigt						Actual material: Voigt					
Voigt	μ_0 [kPa]	μ_I [Pa.s]				Voigt	μ_0 [kPa]	μ_I [Pa.s]			
	23.9	6.66					23.9	6.6			
Fractional	μ_0 [kPa]	μ_α [Pa.s $^\alpha$]	α			Fractional	μ_0 [kPa]	μ_α [Pa.s $^\alpha$]	α		
Voigt	23.9	6.86	0.99			Voigt	23.9	6.6	1		
SLS	μ_0 [kPa]	μ_ω [kPa]	μ_I [Pa.s]			SLS	μ_0 [kPa]	μ_ω [kPa]	μ_I [Pa.s]		
	23.9	741	6.5				23.9	1e6	6.6		
Actual material: Fractional Voigt						Actual material: Fractional Voigt					
Voigt	μ_0 [kPa]	μ_I [Pa.s]				Voigt	μ_0 [kPa]	μ_I [Pa.s]			
	14	6.4					14	5.62			
Fractional	μ_0 [kPa]	μ_α [Pa.s $^\alpha$]	α			Fractional	μ_0 [kPa]	μ_α [Pa.s $^\alpha$]	α		
Voigt	14	141.7	0.59			Voigt	14	140	0.6		
SLS	μ_0 [kPa]	μ_ω [kPa]	μ_I [Pa.s]			SLS	μ_0 [kPa]	μ_ω [kPa]	μ_I [Pa.s]		
	14	21.8	8.9				14	11.6	9.69		
Actual material: SLS						Actual material: SLS					
Voigt	μ_0 [kPa]	μ_I [Pa.s]				Voigt	μ_0 [kPa]	μ_I [Pa.s]			
	14	6					14	4.17			
Fractional	μ_0 [kPa]	μ_α [Pa.s $^\alpha$]	α			Fractional	μ_0 [kPa]	μ_α [Pa.s $^\alpha$]	α		
Voigt	14	808	0.36			Voigt	14	151	0.63		
SLS	μ_0 [kPa]	μ_ω [kPa]	μ_I [Pa.s]			SLS	μ_0 [kPa]	μ_ω [kPa]	μ_I [Pa.s]		
	14	16.1	12.08				14	16	12		

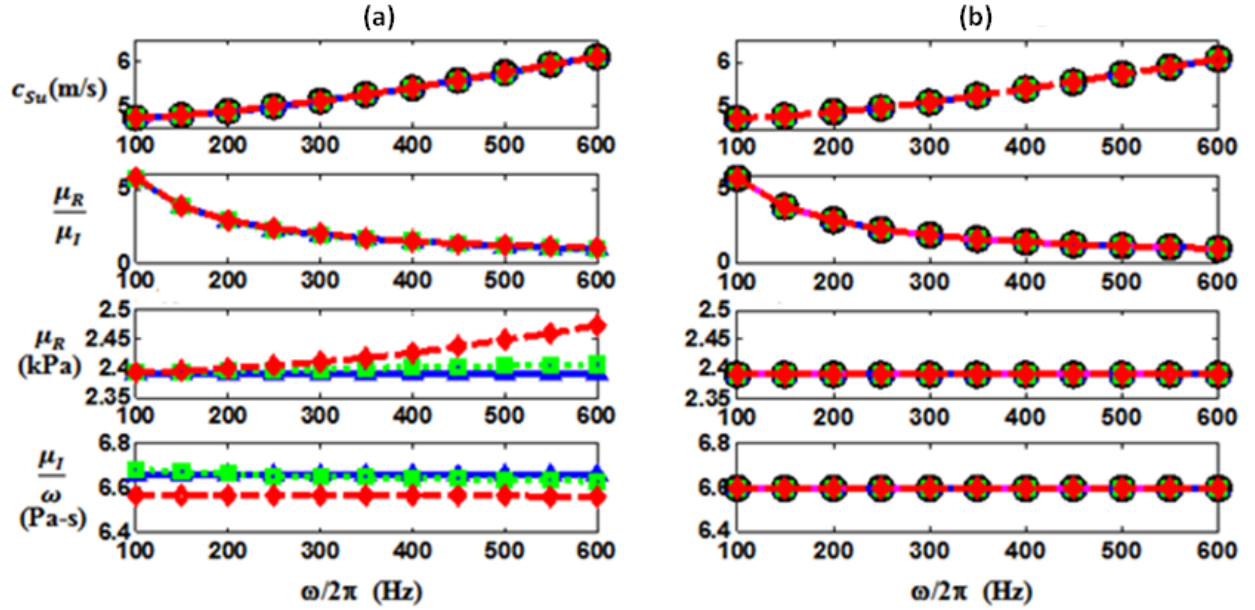


Figure 2.5 Voigt material study. Best fit Voigt, Fractional Voigt and SLS models based on (a) Approach 1 and (b) Approach 2. Key: $\circ \circ \circ$ actual value, — estimated value based on Approach 1 or Approach 2, $\Delta - \Delta$ best fit Voigt, $\square \cdots \square$ best fit Fractional Voigt, $\diamond - \diamond$ best fit SLS.

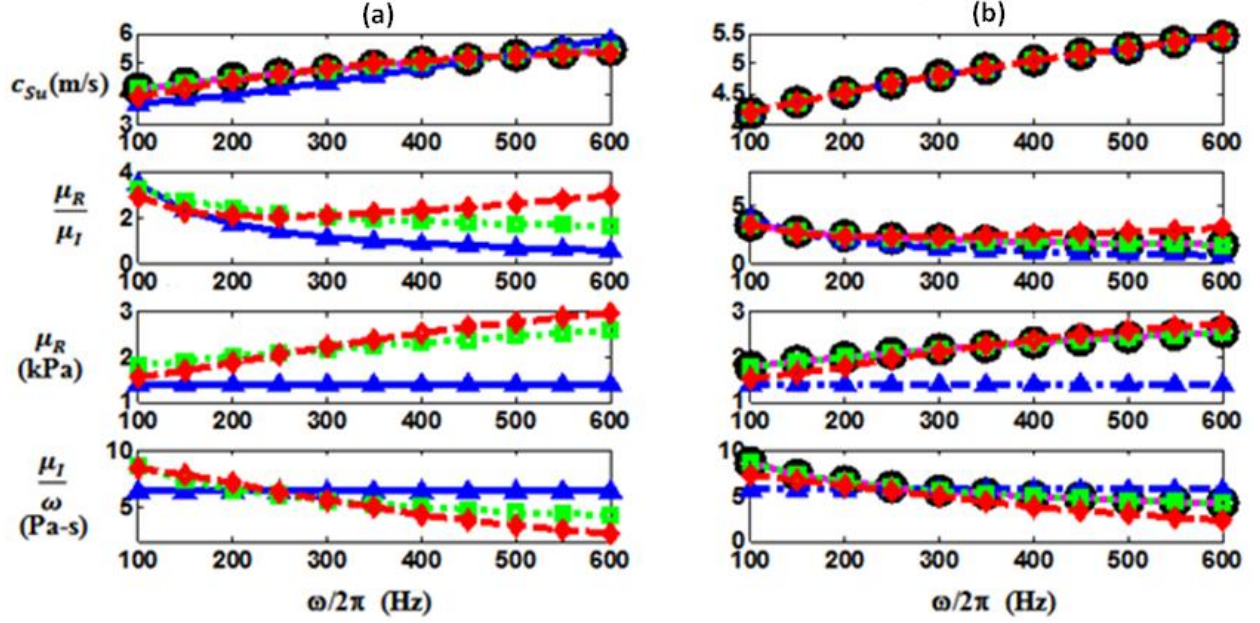


Figure 2.6 Fractional Voigt material study. Best fit Voigt, Fractional Voigt and SLS models based on (a) Approach 1 and (b) Approach 2. Key: $\circ \circ \circ$ actual value, — estimated value based on Approach 1 or Approach 2, $\Delta - \cdot - \Delta$ best fit Voigt, $\square \cdots \cdots \square$ best fit Fractional Voigt, $\diamond - - \diamond$ best fit SLS.

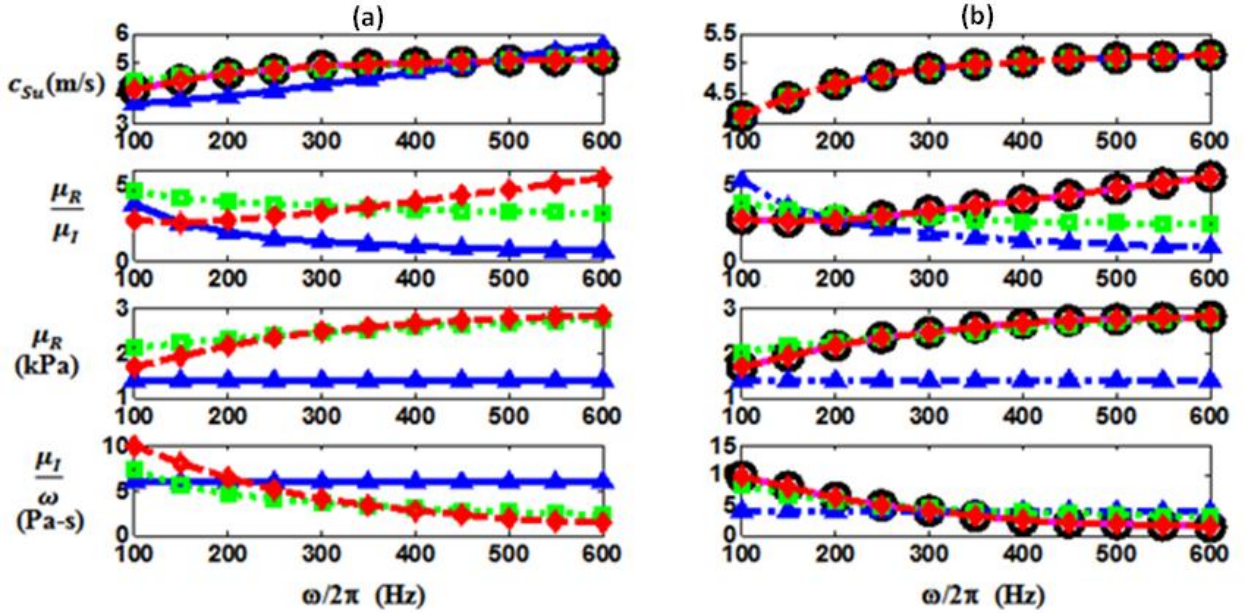


Figure 2.7 SLS material study. Best fit Voigt, Fractional Voigt and SLS models based on (a) Approach 1 and (b) Approach 2. Key: $\circ \circ \circ$ actual value, — estimated value based on Approach 1 or Approach 2, $\Delta - \cdot - \Delta$ best fit Voigt, $\square \cdots \cdots \square$ best fit Fractional Voigt, $\diamond - - \diamond$ best fit SLS.

2.3.2. Numerical Case Studies

The three material property cases of the previous section are next simulated in a finite element (FE) environment using harmonic analysis, except with the important caveat that we no longer have an infinite half space. Rather, we have a cylinder of material, as depicted in Figure 2.8, with finite boundaries. This can be treated as an axisymmetric problem in FE analysis. A 4 node quadrilateral element in the multiphysics finite element software Comsol 4.2 structural mechanics module was used to generate the FRF (displacement/displacement) shown in Figure 2.9. Studies with various element resolutions and other types (e.g. plane triangular element) confirmed that we had asymptotically reached a solution independent of element size/type. (Complementary studies conducted in ANSYS 11.0 that matched the Comsol results, but are not presented here, further verified the numerical approach taken.) While the theoretical analysis of the previous section was for a disk imparting a uniform pressure, a uniform displacement rather than uniform pressure was imparted because: (i) differences in FRFs between the two approaches appeared minimal, and, (ii) uniform displacement loading is closer to the actual loading in the experimental study in Section 2.3.3. In the FE solutions, the following parameter values were held constant: density $\rho = 1,000 \text{ kg/m}^3$ and bulk modulus $K = 2.2 \text{ GPa}$. The viscoelastic coefficients of each model listed in Table 2.1 are specified, per Equations (2.4a-b) and (2.5a-b), which relate them to the complex shear modulus, $\mu = \mu_R + j\mu_I$, another input parameter in the FE simulation.

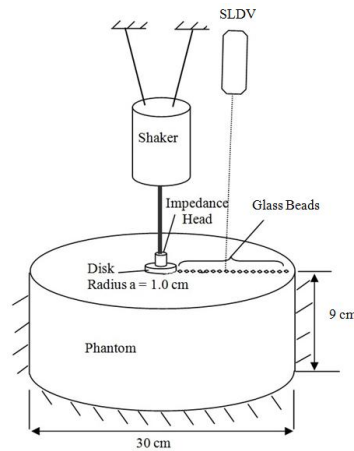


Figure 2.8 Experimental schematic for measurement of surface wave motion caused by a surface source using a scanning laser Doppler vibrometer (SLDV).

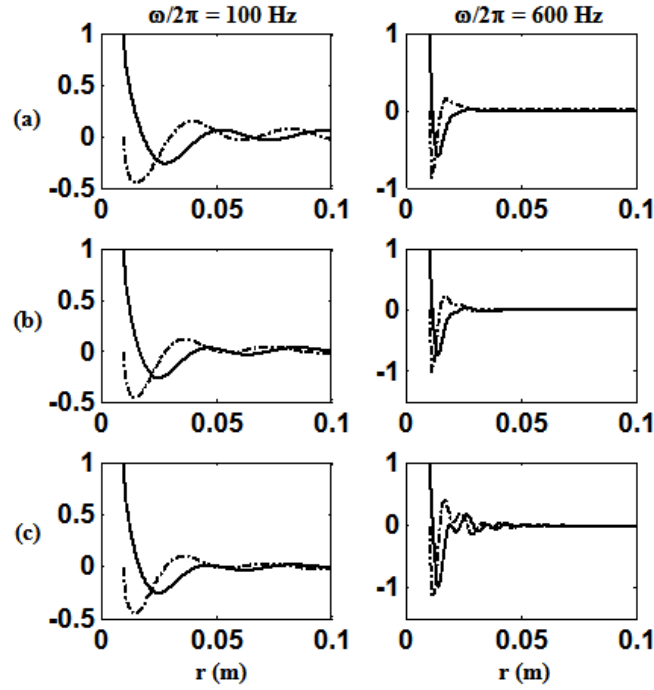


Figure 2.9 Numerical Studies FRF at $\omega/2\pi = 100$ and 600 Hz for (a) Voigt (b) fractional Voigt and (c) SLS material studies. Key: — Real part, — • — Imaginary part. Material property values given in Table 2.1.

Due to finite boundaries and possibly head wave effects mentioned in the previous section, FE simulations do not result in the same FRF responses predicted by theory. Likely, other wave types or wave reflections are present to varying degrees at different radial distances, which will alter predictions of the viscoelastic model based on Approaches 1 and 2. Further analysis of the FE simulation data and calculation of best fit viscoelastic models per Approaches 1 and 2 are conducted as described below.

Results of the best fits using Approaches 1 and 2 are provided in Table 2.3 and in Figures 2.10 – 2.12. Comparing Figures 2.10 – 2.12 (FEA) with 2.5 – 2.7 (theory), it becomes clear that the matter of extracting the correct viscoelastic model type and associated material property values based on surface motion measurements is more challenging than the infinite half-space theory would suggest. From Approach 1 for the Voigt and fractional Voigt cases, a Voigt model assumption essentially yields the best fit as the fractional Voigt and SLS optimizations converge to the Voigt case ($\alpha = 1$ and μ_ω large). For the SLS case, the SLS model assumption fits the phase speed well only from 100 to 300 Hz. This shows the

limitation of Approach 1 and the complexity caused by the finite boundary as the calculated phase speed based on Equation (2.15) is not that accurate. From Approach 2, the best fit model is usually the correct one except for the fractional Voigt case, where the SLS model does slightly better. For the Voigt model case, both the fractional Voigt and SLS models converge to the Voigt model as seen from their respective estimated parameters. For the SLS case, the SLS model is the best fit as the residual error of the estimated shear modulus relative to the actual shear modulus is the smallest.

Table 2.3 Estimated viscoelastic coefficients and residual error in numerical case studies

Approach 1							Approach 2						
			Residual Error ($\times 10^5$)							Residual Error ($\times 10^5$)			
			μ_R	μ_I	μ					μ_R	μ_I	μ	
Actual material: Voigt							Actual material: Voigt						
Voigt	μ_0 [kPa]	μ_I [Pa.s]	0	4.6	4.6		Voigt	μ_0 [kPa]	μ_I [Pa.s]	0	0.02	0.02	
	23.9	81.7						23.9	6.94				
Fractional Voigt	μ_0 [kPa]	μ_x [Pa.s ²]	α	0	4.6	4.6	Fractional Voigt	μ_0 [kPa]	μ_x [Pa.s ²]	α	0	0.02	0.02
	23.9	81.7	1					23.9	6.94	1			
SLS	μ_0 [kPa]	μ_{ω} [kPa]	μ_I [Pa.s]	0.1	4.6	4.6	SLS	μ_0 [kPa]	μ_{ω} [kPa]	μ_I [Pa.s]	0	0.02	0.02
	23.9	1e6	81.7					23.9	1e6	6.86			
Actual material: Fractional Voigt							Actual material: Fractional Voigt						
Voigt	μ_0 [kPa]	μ_I [Pa.s]	0.23	5.7	5.7		Voigt	μ_0 [kPa]	μ_I [Pa.s]	0.27	0.1	0.29	
	14	98.7						14	5.88				
Fractional Voigt	μ_0 [kPa]	μ_x [Pa.s ²]	α	0.23	5.7	5.7	Fractional Voigt	μ_0 [kPa]	μ_x [Pa.s ²]	α	0.11	0.07	0.13
	14	98.7	1					14	36.78	0.77			
SLS	μ_0 [kPa]	μ_{ω} [kPa]	μ_I [Pa.s]	0.10	5.7	5.7	SLS	μ_0 [kPa]	μ_{ω} [kPa]	μ_I [Pa.s]	0.11	0.06	0.12
	14	1e6	98.7					14	42	6.6			
Actual material: SLS							Actual material: SLS						
Voigt	μ_0 [kPa]	μ_I [Pa.s]	0.30	0.40	0.50		Voigt	μ_0 [kPa]	μ_I [Pa.s]	0.36	0.26	0.45	
	14	9.3						14	5.42				
Fractional Voigt	μ_0 [kPa]	μ_x [Pa.s ²]	α	0.32	0.11	0.35	Fractional Voigt	μ_0 [kPa]	μ_x [Pa.s ²]	α	0.13	0.23	0.27
	14	9.7	0.1					14	75	0.67			
SLS	μ_0 [kPa]	μ_{ω} [kPa]	μ_I [Pa.s]	0.32	0.09	0.33	SLS	μ_0 [kPa]	μ_{ω} [kPa]	μ_I [Pa.s]	0.12	0.17	0.21
	14	21.5	61.7					14	26	7.2			

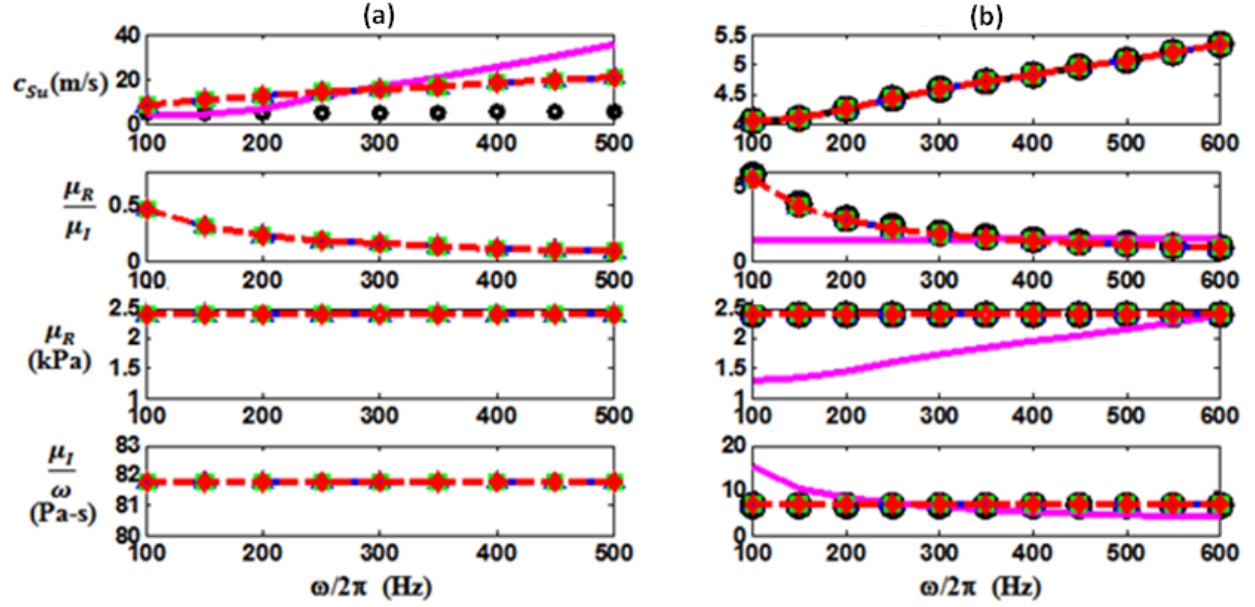


Figure 2.10 Voigt numerical study. Best fit Voigt, Fractional Voigt and SLS models based on (a) Approach 1 and (b) Approach 2. Key: $\circ \circ \circ$ actual value, — estimated value based on Approach 1 or Approach 2, $\Delta - \Delta$ best fit Voigt, $\square \cdots \square$ best fit Fractional Voigt, $\diamond - \diamond$ best fit SLS.

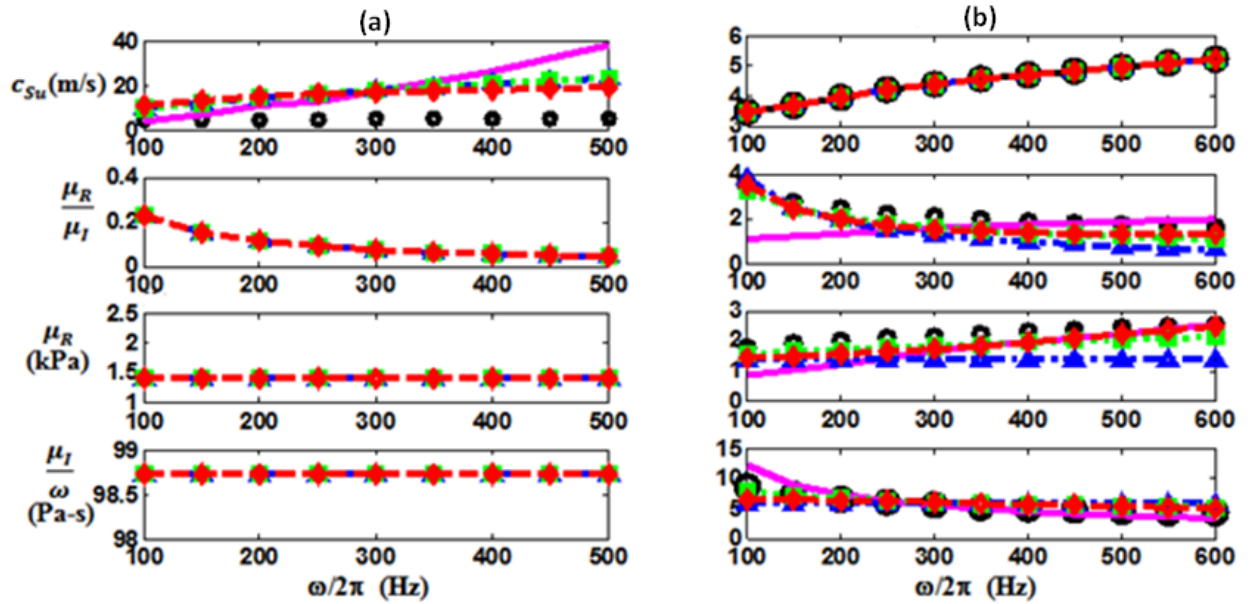


Figure 2.11 Fractional Voigt numerical study. Best fit Voigt, Fractional Voigt and SLS models based on (a) Approach 1 and (b) Approach 2. Key: $\circ \circ \circ$ actual value, — estimated value based on Approach 1 or Approach 2, $\Delta - \Delta$ best fit Voigt, $\square \cdots \square$ best fit Fractional Voigt, $\diamond - \diamond$ best fit SLS.

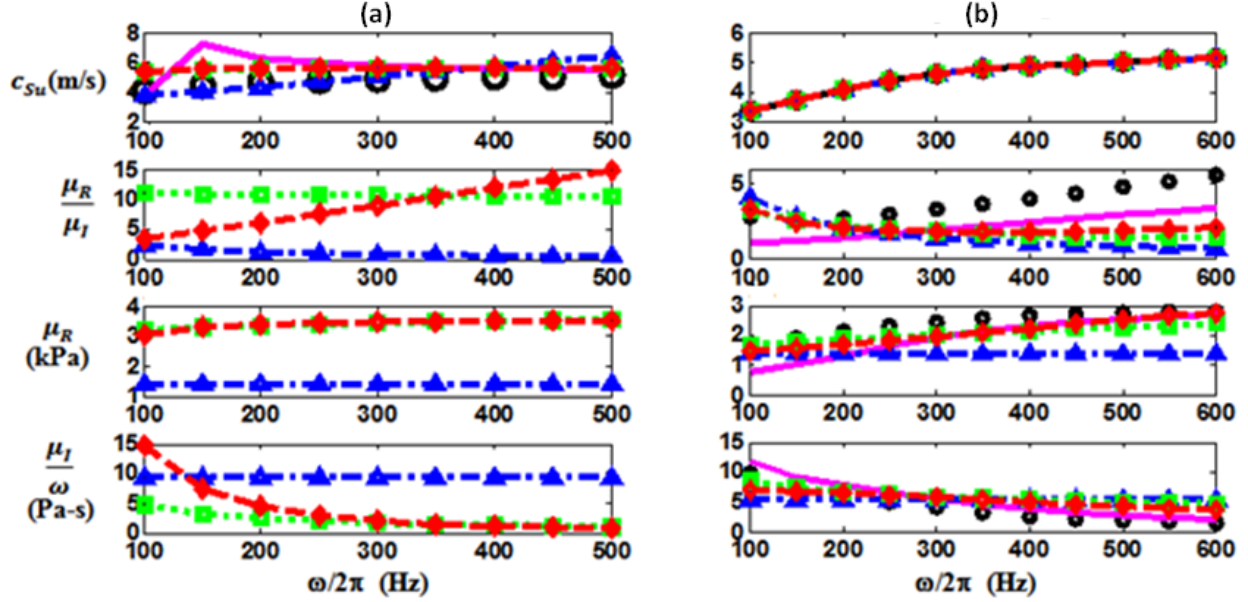


Figure 2.12 SLS numerical study. Best fit Voigt, Fractional Voigt and SLS models based on (a) Approach 1 and (b) Approach 2. Key: $\circ \circ \circ$ actual value, — estimated value based on Approach 1 or Approach 2, $\Delta - \Delta$ best fit Voigt, $\square \cdots \square$ best fit Fractional Voigt, $\diamond - \diamond$ best fit SLS.

2.3.3. Experimental Studies

Surface wave experiments were conducted as depicted in Figure 2.8 on a silicone polymer, Ecoflex 00-10 (NuSil Technology, Carpinteria, CA), which has a density of 965 kg/m^3 calculated through basic mass volume measurements of small test specimens. While in liquid form, the material is poured into the container and then cures at room temperature. Once cured, the material is removed from the container and mounted on a vibration isolated optics bench. A plexiglass disk, driven by a mechanical shaker (ET-132, LabWorks Inc., Mesa Costa, CA) that is supported by a separate structure, is positioned on the surface of the phantom with a sufficient preload to ensure contact during excitation. The shaker is driven via an amplifier (Type 2076, Bruel & Kjaer, Denmark) with a signal input from a dynamic signal analyzer (35670A, Agilent Technologies, Santa Clara, CA). The force and acceleration of the disk is measured with an impedance head (288D01, PCB Piezotronics, Depew, NY), and the out-of-plane velocity at discrete points on the surface are measured using a scanning laser Doppler vibrometer (SLDV: PSV-400, Polytec, Irvine, CA). P-RETRO-250 glass beads ($45 - 63 \text{ } \mu\text{m}$ dia., Polytec, Irvine, CA) are spread on and adhered to the semi-translucent phantom material to aid in SLDV measurement. Scanning

was along a line radially outward from the excitation over a distance of 50 mm with a 1 mm increment and the measurement point closest to the excitation was 5 mm from the rim of the plexiglass disk. Measurement signals are recorded and the frequency response function (FRF) between the output (vertical velocity of the surface points) and input (motion input of the disk) is calculated by the dynamic signal analyzer. Measurements of FRF (velocity/acceleration) are shown in Figure 2.13. The viscoelastic parameters estimation procedure here is essentially the same as the one for FE simulation.

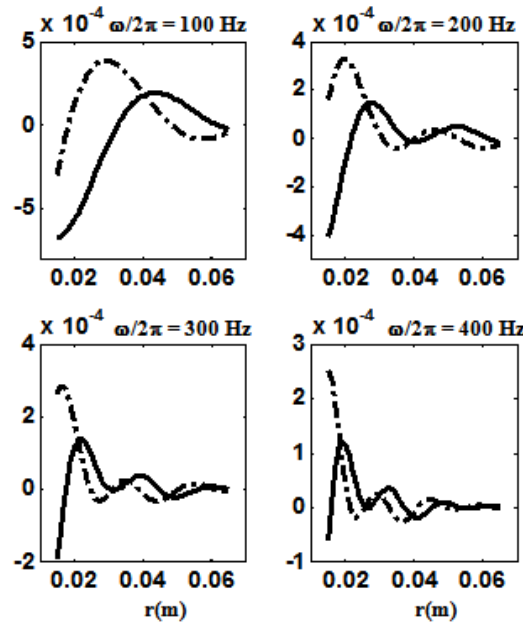


Figure 2.13 Experimental study. FRF at $\omega/2\pi = 100, 200, 300$ and 400 Hz. Key: — Real part, - • - Imaginary part.

A measurement of the phantom relaxed shear modulus was made by indenting an indenter with a spherical end (9.525 mm in diameter) into the phantom. Indentation forces were measured for different indentation depths using a force gauge (Model DPS, Imada, Northbrook, IL). From Equations (2.8) and (2.10), the relaxed shear modulus μ_0 is estimated to be 13.3 kPa.

Results of the best fits using Approach 1 and 2 are shown in Table 2.4 and Figure 2.14. The phase speed estimated by Approach 1 is plotted in a narrower frequency range than that by Approach 2 as the phase speed measured between 100 Hz and 200 Hz deviated too much from the normally expected value. It is shown from Figure 2.14(a) that by Approach 1, a good match to frequency-dependent phase speed is

possible for both the fractional Voigt and SLS model. This again leads to the same conclusion as in Section 2.3.1 that matching phase speed dispersion alone over an order or less of magnitude in frequency probably does not discern which model type is appropriate. While from Figure 2.14(b), the more appropriate model can be identified from μ_R/μ_I versus frequency even though different models lead to almost the same fitting curves for phase speed, μ_R , and μ_I/ω . Thus one may be able to use Approach 2 to better assess which model type is appropriate.

Table 2.4 Estimated viscoelastic coefficients and residual error in experimental studies

Approach 1				Approach 2							
				Residual Error ^a			Residual Error ($\times 10^5$) ^a				
				$Re [K_{su}]$							
Voigt	μ_0 [kPa]	μ_I [Pa.s]		66.19	Voigt	μ_0 [kPa]	μ_I [Pa.s]		0.35	0.18	0.39
	13.3	11.77				13.3	9.96				
Fractional Voigt	μ_0 [kPa]	μ_z [Pa.s ^z]	α	16.67	Fractional Voigt	μ_0 [kPa]	μ_z [Pa.s ^z]	α	0.06	0.11	0.13
	13.3	535	0.49			13.3	350.77	0.55			
SLS	μ_0 [kPa]	μ_ω [kPa]	μ_I [Pa.s]	17.19	SLS	μ_0 [kPa]	μ_ω [kPa]	μ_I [Pa.s]	0.02	0.04	0.04
	13.3	29.5	18.97			13.3	27.25	17.77			

^aHere, residual error is with respected to the calculated values of $Re[K_{su}]$ (Approach 1) and complex μ (Approach 2), as the actual values and type of viscoelastic model are unknown.

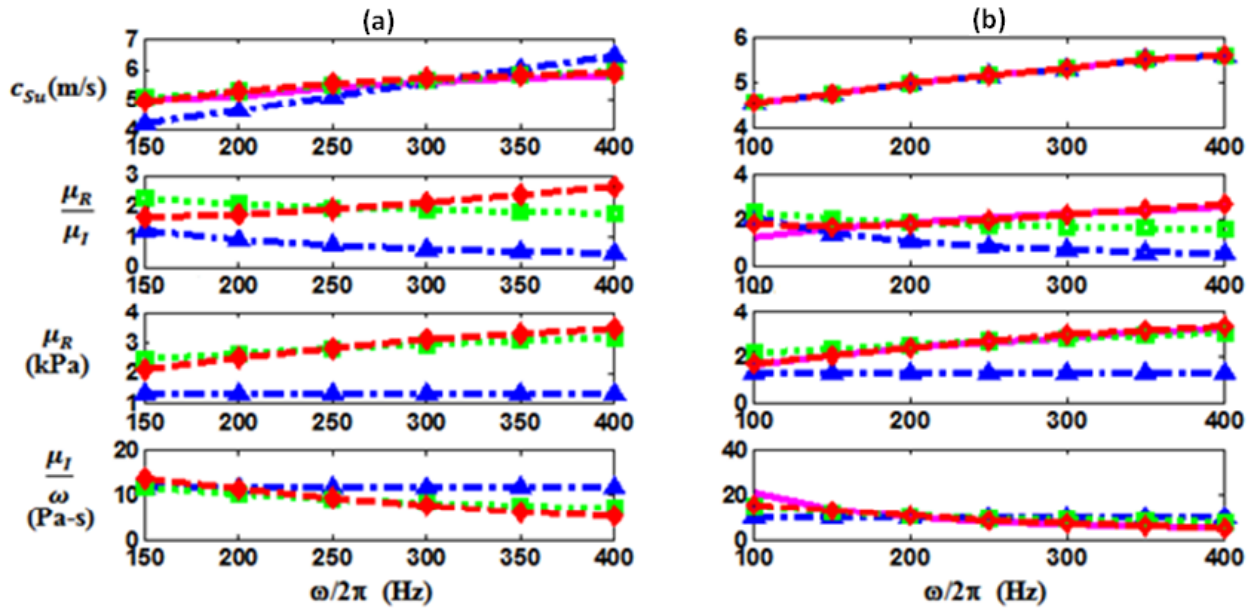


Figure 2.14 Experimental study. Best fit Voigt, Fractional Voigt and SLS models based on (a) Approach 1 and (b) Approach 2. Key: — estimated value based on Approach 1 or Approach 2, Δ — Δ best fit Voigt, \square — \square best fit Fractional Voigt, \diamond — \diamond best fit SLS.

2.4. Viscoelasticity Identification of Ex vivo Pig Lung

2.4.1. Compression Wave, Shear Wave and Surface Wave in the Lung

The lung parenchyma is comprised of soft biological tissue and vasculature, as well as millions of microscopic air sacs (alveoli) that are connected through a complex branching airway structure. Thus, microscopically the lungs are highly heterogeneous in terms of their physical properties, combining gas (air) that is linked through a complex and tortuous network of channels and microscopic sacs, non-Newtonian liquid (blood) that flows through an equally complex network of vessels of wide-ranging dimensions, and solid tissue structure comprised of a mixture of viscoelastic soft tissues that exhibit nonlinear behavior under large deformation. Previously, it has been proposed that, for the purpose of calculating compression wave behavior over the audible frequency range, parenchymal tissue can be modeled as a homogenous isotropic material with properties analogous to those observed in water that is uniformly populated with small gas bubbles [39-41]. This is a “closed cell” approximation, meaning that it assumes that the oscillating motion caused by the compression wave is so fast that the air in the lungs does not have time to flow between different regions. It has been estimated that such an assumption will only be valid above ~100 Hz. For compression wavelengths much larger than alveoli size (which will be the case in the low audible frequency range considered here up to several kHz), compression wave speed c_p is approximated as

$$c_p = \sqrt{K/\rho}, \quad (2.18a)$$

with

$$\frac{1}{K} = \phi \frac{1}{K_f} + (1 - \phi) \frac{1}{K_s}, \quad (2.18b)$$

$$\rho = \rho_s(1 - \phi) + \rho_f \phi. \quad (2.18c)$$

where K is the bulk modulus of the composite mixture, an effective bulk modulus comprised of a reciprocal of bulk moduli of the non-gaseous (soft tissue and blood) (K_s) and gaseous (air) (K_f) components of the lung. Here, ϕ denotes the volume fraction of the gas portion of the lungs and is defined as $\phi = V_f/V_T$, where V_f is the volume of the gas in the lungs and V_T is the total volume of the

lung. In a similar manner the composite density of the lungs ρ is a weighted sum of the densities of the gas portion (ρ_f) and the non-gaseous portion (ρ_s). The above equation is sometimes referred to as Wood's formula [39]. As frequency increases and compression wavelength approaches that of alveoli size, the resonant behavior of the individual alveoli adds more complexity to the calculation of the wave speed. See Wodicka et al. [40] for a detailed discussion.

As the gas component is air, we assume $K_f = nP$, where n is the polytropic constant and P denotes the pressure in the lungs (atmospheric pressure plus the lung inflation pressure). The polytropic constant n will be somewhere between 1 (isothermal process) and the ratio of specific heats of air, which is 1.41 (adiabatic process). As frequency increases and the speed of fluctuations in local temperature and motion in the gas associated with wave passage increase, it is expected that the process will transition from being closer to isothermal to become closer to adiabatic.

Attenuation of compression waves as they propagate is driven by both thermal dissipation (if nonadiabatic) and viscous (solid and fluid) effects. Wodicka et al. [40] modeled the lung parenchyma as air bubbles (alveoli) in water (lung tissue) at low audible frequencies and proposed that the magnitude of thermal losses are theoretically much larger than those associated with scattering or viscous effects. The thermal dissipation also varies with frequency as wavelength approaches that of the alveoli size. For harmonic motion and time dependence $e^{j\omega t}$, the resulting complex-valued compression wave number k_p can be expressed as [41]

$$k_p = \omega/c_p - j\alpha_p, \quad (2.19a)$$

$$\text{with} \quad \alpha_p = N\sigma/2. \quad (2.19b)$$

Here, N is the number of bubbles (alveoli) per unit volume and σ , which is frequency-dependent, is the extinction cross section for each bubble. For frequencies such that wavelengths are much larger than the alveoli size the value of σ is proportional to ω^2 [40]. Here, the real part of k_p is related to compression wave speed c_p and the imaginary part defines the attenuation.

The above effective medium analogy is only useful in calculating compression wave behavior, not shear wave behavior. However, a decoupled equation for shear wave motion can be formulated based on using the above average lung density value ρ combined with a value for shear viscoelasticity of the lungs μ , which may be rate-dependent due to shear viscosity such that, in the frequency domain, the complex-valued wave speed c_s and shear wave number k_s are

$$c_s = \sqrt{\mu/\rho}, \quad (2.20a)$$

$$k_s = \omega/c_s. \quad (2.20b)$$

Here, the real part of k_s governs shear wave speed and the imaginary part defines the attenuation. The appropriate form of a shear viscoelastic model for soft biological tissues, let alone the lung parenchyma, is still a subject of much research, particularly in the elastography literature. Suffice it to say, the model choices are empirical, based on their ability to match experimental measurements over a range of frequencies. This will be investigated further with regard to experimental studies in Section 2.4.2 .

2.4.2. Experimental Studies

Experiments were carried out on the lung of a freshly sacrificed pig that weighed 50 kg. Immediately upon sacrifice the lung was inflated by air with positive pressure of 25 cm H₂O gage. As the chest cavity was surgically opened and pleural pressure became atmospheric pressure, the transpulmonary pressure (P_{tp} , airway pressure relative to pleural or atmospheric pressure) was maintained at 25 cm H₂O. It was observed that all the lung lobes were uniformly inflated and no noticeable amounts of gas trapping were found under the pleural membrane. The lung was removed from the chest of the pig, blood drained, and placed on a vibration isolated test bench in a room maintained at 20°C. The sequence of experiments on the lung included: surface wave measurements and mechanical indentation measurements. The time range of these measurements postmortem was about 0.5-1 hours and 1-1.5 hours respectively. During this time the lung was periodically sprayed with water to keep the surface moist.

From the mechanical indentation measurements, the relaxed shear modulus of the lung μ_0 is estimated to be 3.76 KPa. The experimental setup described in Section 2.3.3 was mainly followed. A plexiglass disk with radius of 10 mm was driven by an electromagnetic shaker (ET-132, Lab-Works Inc., Mesa Costa, CA). A harmonic force with frequency from 100 Hz to 500 Hz was applied on the lung surface by the plexiglass disk. An impedance head (288D01, PCB Piezotronics, Depew, NY) was mounted on the plexiglass disk to measure its acceleration. Out-of-plane velocity of the points on the lung surface was measured by a scanning laser Doppler vibrometer (SLDV) (PSV-400, Polytec, Tustin, CA). The experimental setup is shown in Figure 2.15.



Figure 2.15 Experimental setup of ex vivo pig lung surface wave measurement.

The frequencies of excitation force were from 100 Hz to 500 Hz with an increment of 50 Hz. Scanning was along a line radially outward from the excitation area over a distance of 30 mm with a 3mm increment and the measurement point closest to the excitation was 5 mm from the rim of the plexiglass disk. The real part, imaginary part and amplitude (in dB) of the FRF as a function of the distance from the source at 100 Hz and 500 Hz are shown in Figure 2.16.

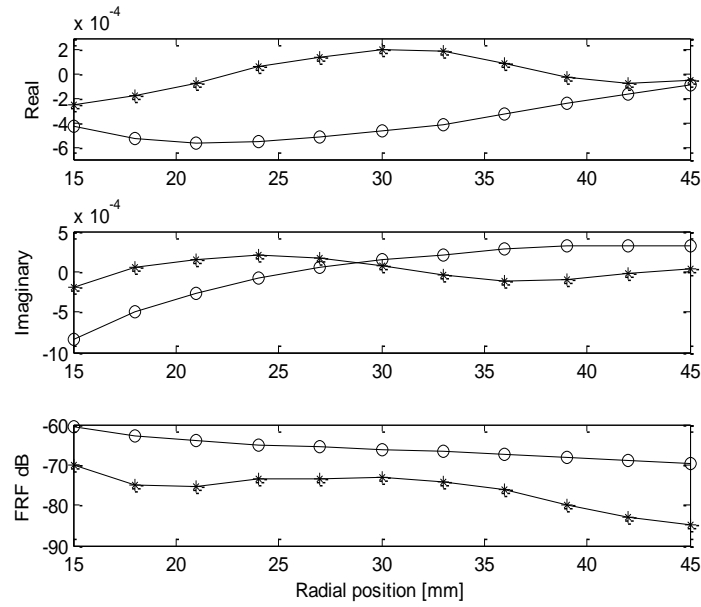


Figure 2.16 Frequency response function versus radial position, $\circ\circ\circ$ 100 Hz, $***$ 500 Hz.

Results of the best fits using Approach 1 and 2 are shown in Table 2.5 and Figure 2.17. It is shown from Table 2.5 that by Approach 1, the SLS model is almost as good as the fractional Voigt model in terms of the shear modulus residual error. While by Approach 2, the fractional Voigt leads to the smallest shear modulus residual error. Thus one may be able to use Approach 2 to better assess which model type is appropriate. Even though none of the models match perfectly with the calculated μ_R and μ_I/ω from Figure 2.17(b), this may be due to the following factors. The excised lung is not a semi-infinite half space, this will cause some inaccuracies in the FRF fitting. The inhomogeneity on the lung surface leads to some deviations in the measurement. All these factors make the calculated μ_R and μ_I/ω not have as a nice trend as the ones in the ecoflex phantom experiment. On one hand, it shows that the lung viscoelasticity model type is complex and a three-parameter model may not be accurate enough to characterize its viscoelastic properties. On the other hand, there is deviation from the isotropic and homogeneous half-space for the lung geometry, this also affects the accuracy of lung viscoelastic model type identification and parameter estimation. It reveals the complexity and inherent limitations to identifying pig lung viscoelastic properties based on surface wave measurements.

Table 2.5 Estimated viscoelastic coefficients and residual error in experimental studies

Approach 1					Approach 2						
				Residual Error*					Residual Error ($\times 10^3$)*		
				C _{SU}					μ_R	μ_I	μ
Voigt	μ_0 [kPa]	μ_l [Pa.s]		0.1274	Voigt	μ_0 [kPa]	μ_l [Pa.s]		72.33	23.74	76.13
	3.76	0.5				3.76	0.15				
Fractional Voigt	μ_0 [kPa]	μ_0 [Pa.s ^a]	α	0.0317	Fractional Voigt	μ_0 [kPa]	μ_0 [Pa.s ^a]	α	8.07	6.52	10.37
	3.76	2.68	0.49			3.76	6.35	0.53			
SLS	μ_0 [kPa]	μ_0 [Pa]	μ_l [Pa.s]	0.0314	SLS	μ_0 [kPa]	μ_0 [Pa]	μ_l [Pa.s]	13.57	4.24	14.22
	3.76	500	0.28			3.76	565.4	0.22			

to measure the Rayleigh wave speed and a function of frequency (i.e. wavelength as a function of frequency) and then to optimize the coefficients in an assumed viscoelastic model type to minimize the difference between the measured and predicted values. Another approach is to measure the complex-valued frequency response function (FRF) between the excitation location and points at known radial distances from the excitation location. (This does require that one knows the size and location of the excitation relative to the measurement points, information not necessary for the first approach.) The FRF has embedded in it frequency-dependent information about both surface wave phase speed (i.e. wavelength) and attenuation; it can be used to directly estimate the real and imaginary parts of the complex shear modulus (storage and loss shear moduli). The coefficients in an assumed viscoelastic tissue model type can then be optimized to minimize the differences in the predicted and experimentally determined values of the complex moduli. The relative merits of these approaches were explored theoretically, computationally and experimentally on a tissue-mimicking phantom. While theoretical and experimental studies suggested that Approach 2 was more capable of distinguishing which type of viscoelastic model was most appropriate, finite element studies highlighted the complications that arise due to finite boundary conditions and multiple wave types for both approaches. The surface wave measurements on excised pig lungs reveal the complexity of lung viscoelasticity and the lung geometry also affects the accuracy of its viscoelastic model type identification and parameter estimation. There are inherent limitations to identifying viscoelastic properties based on surface wave measurements. The findings of this study on surface waves, in terms of the merits of different approaches and limitations, are likely also relevant to identification of viscoelastic models and properties based on shear wave imaging, given the close relationship between the two wave types.

2.6. References

1. Zhang XM, Kinnick RR, Greenleaf JF, 2008, Viscoelasticity of lung tissue with surface wave method, *Ultrasonics Symposium, IEEE*, pp.21-23.

2. Yamakoshi Y, Sato J, Sato T, 1990, Ultrasonic imaging of internal vibration of soft tissue under forced vibration, *IEEE Trans. Ultrason. Ferroelectr. Freq. Contr.* 37, pp. 45–53.
3. Muthupillai R, Lomas DJ, Rossman PJ, Greenleaf JF, Manduca A, Ehman, RL, 1995, Magnetic resonance elastography by direct visualization of propagating acoustic strain waves, *Science*, 269, pp. 1854–1857.
4. Zhang XM, Greenleaf JF, 2007, Estimation of tissue's elasticity with surface wave speed, *J. Acoust. Soc. Am.* 122, pp. 2522–2525.
5. Duck FA, 1990, *Physical properties of tissue: a comprehensive reference book*, Academic Press, New York, NY.
6. Kuperman V, 2000, *Magnetic resonance imaging: physical principles and applications*, Academic Press, New York.
7. Hoyt K, Kneezel T, Castaneda B, Parker KJ, 2008, Quantitative sonoelastography for the in vivo assessment of skeletal muscle viscoelasticity, *Phys. Med. Biol.* 53, pp. 4063–4080.
8. Fung YC, 1993, *Biomechanics: mechanical properties of living tissues*, 2nd Ed., Springer-Verlag, New York.
9. Sarvazyan AP, Rudenko OV, Swanson SD, Fowlkes JB, Emelianov SY, 1998, Shear wave elasticity imaging: a new ultrasonic technology of medical diagnostics, *Ultrasound in Med. & Biol.* 24, pp. 1419–1435.
10. Chan RW, Titze IR, 2003, Effect of postmortem changes and freezing on the viscoelastic properties of vocal fold tissues, *Ann. Biomed. Eng.* 31, pp. 482–491.
11. Craiem D, Armentano R, 2007, A fractional derivative model to describe arterial viscoelasticity, *Biorheol.* 44, pp. 251–263.
12. Kiss MZ, Varghese T, Hall TJ, 2004, Viscoelastic characterization of in vitro canine tissue, *Phys. Med. Biol.* 49, pp. 4207–4218.

13. Klatt D, Hamhaber U, Asbach P, Braun J, Sack I, 2007, Noninvasive assessment of the rheological behavior of human organs using multifrequency MR elastography: a study of brain and liver viscoelasticity, *Phys. Med. Biol.* 52, pp. 7281–7294.
14. Riek K, Klatt D, Nuzha H, Mueller S, Neumann U, Sack I, Braun J, 2011, Wide-range dynamic magnetic resonance elastography, *J. Biomech. Eng.* 44, pp. 1380–1386.
15. Sinkus R, Tanter M, Xydeas T, Catheline S, Bercoff J, Fink M, 2005, Viscoelastic shear properties of in vivo breast lesions measured by MR elastography, *Magn. Reson. Imag.* 23(2), pp. 159-165.
16. Royston TJ, Mansy HA, Sandler RH, 1999, Excitation and propagation of surface waves on a viscoelastic half-space with application to medical diagnosis, *J. Acoust. Soc. Am.* 106, pp. 3678–3686.
17. Royston TJ, Yazicioglu Y, Loth F, 2003, Surface response of a viscoelastic medium to subsurface acoustic sources with application to medical diagnosis, *J. Acous. Soc. Amer.* 113, pp. 1109 – 1121.
18. Meral FC, Royston TJ, Magin RL, 2009, Surface response of a fractional order viscoelastic halfspace to surface and subsurface sources, *J. Acoust. Soc. Am.* 126, pp. 3278–3285.
19. Zhang XM, Osborn TG, Pittelkow MR, Qiang B, Kinnick RR, Greenleaf JF, 2011, Quantitative assessment of scleroderma by surface wave technique, *Med. Eng. & Phy.* 33, pp. 31-37.
20. Qiang B, Greenleaf JF, Zhang XM, 2010, Quantifying viscoelasticity of gelatin phantoms by measurement impulse response using compact optical sensors, *IEEE Trans. Ultrason. Ferroelectr. Freq. Contr.* 57, pp. 1696–1700.
21. Chen SG, Fatemi M, and Greenleaf JF, 2004, Quantifying elasticity and viscosity from measurement of shear wave speed dispersion, *J. Acoust. Soc. Am.* 115, pp. 2781–2785.
22. Zhang XM, Kinnick RR, Fatemi M, Greenleaf JF, 2005, Noninvasive method for estimation of complex elastic modulus of arterial vessels, *IEEE Trans. Ultrason. Ferroelectr. Freq. Contr.* 52, pp. 642–652.
23. Giannoula A, Cobbold RSC, 2008, Narrowband shear wave generation by a finite-amplitude radiation

- force: the fundamental component, *IEEE Trans. Ultrason. Ferroelectr. Freq. Contr.* 55, pp. 343–358.
24. Deffieux G, Montaldo M, Tanter, Fink M, 2009, Shear wave spectroscopy for in vivo quantification of human soft tissues visco-elasticity, *IEEE Trans. Med. Imag.* 28, pp. 313–322.
 25. Gennisson JL, Deffieux T, Macé E, Montaldo G, Fink M, Tanter M, 2010, Viscoelastic and anisotropic mechanical properties of in vivo muscle tissue assessed by supersonic shear imaging, *Ultrasound in Med. & Biol.* 36, pp. 789–801.
 26. Orescanin M, Insana MF, 2010, Shear modulus estimation with vibrating needle stimulation, *IEEE Trans. Ultrason. Ferroelectr. Freq. Contr.* 57, pp. 1358-1367.
 27. Oestreicher HL, 1951, Field and impedance of an oscillating sphere in a viscoelastic medium with an application to biophysics, *J. Acoust. Soc. Am.* 23, pp. 707–714.
 28. Magin RL, 2006, *Fractional calculus in bioengineering*, Begell House, Redding, CT.
 29. Heymans N, 2008, Dynamic measurements in long-memory materials: Fractional calculus evaluation of approach to steady state, *J. Vib. Contr.* 14, pp. 1587-1596.
 30. Mainardi F, 1997, Fractional calculus: some basic problems in continuum and statistical mechanics, in *Fractals and fractional calculus in continuum mechanics*, Carpinteri A, Mainardi F (eds), Springer Verlag, New York.
 31. Lakes RS, 1999, *Viscoelastic solids*, CRC Press, Boca Raton, FL.
 32. Timoshenko SP, Goodier JN, 1970, *Theory of elasticity*, 3rd ed., McGraw-Hill, New York.
 33. Butler JP, Nakamura M, Sasaki H, Sasaki T, Takishima T, 1986, Poissons' ratio of lung parenchyma and parenchymal interaction with bronchi, *Jpn. J. Physiol.* 36(1), pp. 91-106.
 34. Miller GF, Pursey H, 1954, The field and radiation impedance of mechanical radiators on the free surface of a semi-infinite isotropic solid, *Proc. Roy. Soc. A* 223, pp. 521–541.
 35. Miller GF, Pursey H, 1955, On the partition of energy between elastic waves in a semi-infinite solid, *Proc. Roy. Soc. A* 223, pp. 55–69.

36. Fung YC, 1965, *Foundations of solid mechanics*, Prentice Hall, NJ.
37. Achenbach JD, 1973, *Wave propagation in elastic solids*, North-Holland, Amsterdam, Netherlands.
38. Graff KF, 1991, *Wave motion in elastic solids*, Dover Publication, New York.
39. Rice DA, 1983, Sound speed in pulmonary parenchyma, *J. Appl. Physiol.* 54, pp. 304–308.
40. Wodicka GR, Stevens KN, Golub HL, Cravalho EG, Shannon DC, 1989, A model of acoustic transmission in the respiratory system, *IEEE Trans. Biomed. Eng.* 36, pp. 925 – 34.
41. Royston TJ, Zhang X, Mansy HA, Sandler RH, 2002, Modeling sound transmission through the pulmonary system and chest with application to diagnosis of a collapsed lung, *J. Acous. Soc. Amer.* 111, pp. 1931 – 1946.

CHAPTER 3

Poroviscoelastic Modeling of Sound Propagation in the Lung

3.1. Introduction

Like no other anatomical region in the body, the lungs are a unique, multiphase porous structure that has defied conventional noninvasive medical imaging methods and our ability to contrast and quantify changes in its macroscopic properties that can be indicative of disease and which may be fundamentally linked to behavioral and structural changes at the microscopic scale. Patients can suffer from a wide range of pulmonary ailments that result in significant changes, locally or diffusely, to the stiffness or density in the lungs, with findings that include inflammation, fibrosis, edema, consolidation or a mass (tumor). These changes often are not easily identifiable by most imaging modalities.

The utility of conventional ultrasound pulmonary imaging is severely limited due to the acoustic impedance mismatch between the air in the lungs and soft tissue. X-ray computed tomography (CT) and magnetic resonance imaging (MRI) provide useful anatomic information, but are often limited in their diagnostic accuracy, especially in distinguishing benign, infectious and malignant pathologies. CT also has the disadvantage of cancer risk associated with ionizing radiation. Spirometry, including the measurement of the volume of inhaled or exhaled air as a function of time, provides a global measure of lung and airway properties, but often provides relatively non-specific findings. Sputum monitoring and respiratory tests before and after the administration of bronchial dilators to assess changes in airway plasticity similarly provide global and, at best, indirect information on spatial extent. MRI using RF tagging techniques has been suggested as a method for assessing the regional mechanical properties of the parenchyma [1, 2]; but, this approach is limited to assessing changes in lung volume throughout the respiratory cycle.

Beyond obtaining an image that depicts the distribution of lung sounds on the torso surface, if a better understanding of mechanical wave propagation within the lungs and torso were available, one may be able to reconstruct the wave field within the lungs and torso based on the noninvasive surface measurements. This would take the 2 dimensional surface image into 3 dimensions, and could potentially

provide not only the location but also more quantitative information about the properties of the lung that can affect how sound and vibration propagate through it [3].

Also recently, the phase contrast-based technique known as magnetic resonance elastography (MRE), has been applied to the lungs in pilot studies with limited success [4-7]. MRE seeks to provide a map of the viscoelastic properties within the region of interest that will affect the shear wave motion that MRE measures. Previously, MRE has been successfully applied to the study of the mechanical properties of a variety of other organs and soft tissue regions in vivo, including the breast, brain, kidney, prostate, liver and muscle [8-12]. Application to the lungs has proven more challenging, given the poor signal-to-noise available in imaging due to a lower presence of hydrogen in air than in soft tissue (water), and the complex nature of vibratory wave propagation found in the lungs. Again, the authors propose that a better understanding of mechanical wave motion in the lungs would aid in the interpretation of the wave images that are acquired using MRE to reconstruct a quantitative map of variation in mechanical properties that can correlate with injury, the progression of disease and/or the response to therapy.

However, for the purpose of developing a tractable set of equations for predicting small-amplitude mechanical wave motion in the parenchyma for wavelengths larger than the microscopic heterogeneous features of the lung, macroscopic homogenized representations of the lung's physical properties have been proposed. Based on this homogenous or stochastic spatially-averaged view, two different models for wave propagation have been put forth. One is sometimes referred to as the "effective medium" or "bubble swarm" theory. It has been prominently used in the literature for modeling lung acoustics since the 1980's [13-15]. More recently, there has been an interest in applying Biot's theory of poroelasticity to the lung [16]. Application of Biot theory leads to a more complex theoretical model that predicts more wave types as compared to the effective medium theory [16]. From a practical and ultimately clinical perspective, questions of interest include: (1) how do these theories compare to each other and to experimental measurements; (2) how complex does the theory need to be to capture the salient phenomena that is measurable and can be linked to disease or injury; and (3) how easily are these theories applied or integrated into computational frameworks that would enable one to better understand

and quantify with specificity and significance how mechanical wave phenomena, that may be measured by application of the existing or nascent imaging technologies mentioned above, is affected by disease and pathology.

In this chapter of the dissertation these theories are compared through analytical and experimental studies. In Section 3.2, the key aspects of Biot theory, as applied to the lungs, are presented, culminating in a comparison of predicted wave attributes, namely wave speed and attenuation in Section 3.3. In Section 3.4, several experiments are detailed that are aimed at identifying key parameters used and predicted by the theories. The applicability of the proposed theories is experimentally assessed by comparison of their predictions to experimental measurements made on freshly excised pig lungs. Experiments at different transpulmonary pressures include sound transmission measurements that primarily provide information about compression waves, surface wave measurements that are linked to shear wave behavior, and measurements of basic lung mechanical properties. Finally an overall discussion is presented in Section 3.5.

3.2. Biot Theory Applied to Wave Propagation in the Lung

Assuming a homogenous isotropic poroviscoelastic medium and small deformations such that linear theory is valid, per Biot theory [17, 18] we have the following set of coupled differential equations (written in the Laplace domain where multiplication by s denotes a derivative with respect to time) describing dynamic oscillatory displacement u of the non-gaseous portion and dynamic pressure p of the gaseous portion [19]:

$$\mu u_{i,jj} + \left(K_b + \frac{\mu}{3}\right) u_{j,ij} - (\alpha - \beta) p_{,i} + F_i = s^2(\rho - \beta \rho_f) u_i, \quad (3.1a)$$

$$\beta p_{,ii} - \frac{\phi^2}{R} \rho_f s^2 p + \rho_f s a = \rho_f s^2 (\alpha - \beta) u_{i,i}. \quad (3.1b)$$

Here, Einstein summation notation is used, such that a repeated index in the subscript denotes summation of all the terms (such as x , y and z in a Cartesian coordinate system). Subscripts after the comma denote partial derivatives in those directions. K_b is the bulk modulus of the solid skeleton. Many of the other

material constants in the above equations were defined in the previous section. Newly introduced terms F_i and a denote external inputs of force per unit volume (e.g. Newtons per cubic meter) and the rate of introduction of gas volume per unit volume (e.g. inverse seconds) respectively. We also have the following [19]:

$$\alpha = 1 - \frac{K_b}{K_s}, \quad (3.2a)$$

$$\beta = \frac{\kappa \rho_f \phi^2 s}{\phi^2 + s \kappa (\rho_a + \phi \rho_f)}, \quad (3.2b)$$

$$R = \frac{\phi^2 K_f K_s^2}{K_f (K_s - K_b) + \phi K_s (K_s - K_f)}, \quad (3.2c)$$

$$\rho_a = (\tau - 1) \rho_f \phi, \quad (3.2d)$$

where τ is the tortuosity, which (as normally defined) is the square of the ratio of the minimum path length of a contiguous path through the pore network, to the straight path length. It is a shape factor depending on the pore geometry. The pore space in the lungs (respiratory tree) can be approximated as a sinuous cylindrical channel network with varying diameter, so the tortuosity at low frequencies is 1.33 [20]. $\kappa = \kappa_p / \nu_f$, κ_p is the permeability of the porous medium, and for a network of tortuous capillaries of any cross-section, $\kappa_p \propto \phi^3 S / \tau$ [21], where S is the specific area of the pore space. ν_f is the complex-valued fluid (gas) viscosity defined as [18]

$$\nu_f = F(\theta) \mu_f, \quad (3.3a)$$

where $F(\theta)$ is the frequency correction function for the viscosity and μ_f is the dynamic viscosity of the fluid (in $\text{Pa} \cdot \text{s}$). By applying Biot theory to the lungs, the fluid (air) in the pores (bronchioles and alveolar sacs) is modeled as three-dimensional flow in a circular straight duct with radius r . As the airway tree progressively subdivides, it finally reaches the alveolar sac which is made of clusters of alveoli. An alveolar duct is formed by a series of alveoli lying adjacent to one another. A microscope image showing morphometric parameters h (alveolar depth) and r (alveolar duct radius) for an alveolar duct is displayed in Figure 3.1. The flow type is Poiseuille flow when the duct wall is at rest. When the fluid and the solid

skeleton oscillates at a frequency ω , there is a deviation from the Poiseuille flow and the dynamic viscosity of the fluid is multiplied by a frequency correction function $F(\theta)$. $F(\theta)$ is defined as

$$F(\theta) = \frac{1}{4} \frac{\theta T(\theta)}{1 + 2jT(\theta)/\theta}, \quad (3.3b)$$

where $\theta = r \sqrt{\frac{\xi \omega}{\mu_f / \rho_f}}$, $T(\theta) = \frac{-\sqrt{-j} J_1(\sqrt{-j}\theta)}{J_0(\sqrt{-j}\theta)}$. As the pores are not parallel but sinuous, a sinuosity factor ξ is introduced to account for this effect and ξ is the square root of the tortuosity. Here J_0 and J_1 are Bessel functions of the first kind. At high frequencies, $F(\theta) \rightarrow \frac{\theta}{4} (\frac{1+j}{\sqrt{2}})$. As the friction between the fluid and the duct wall is proportional to $F(\theta)$, the friction is proportional to the square root of the frequency and is 45 degrees out of phase with the velocity.

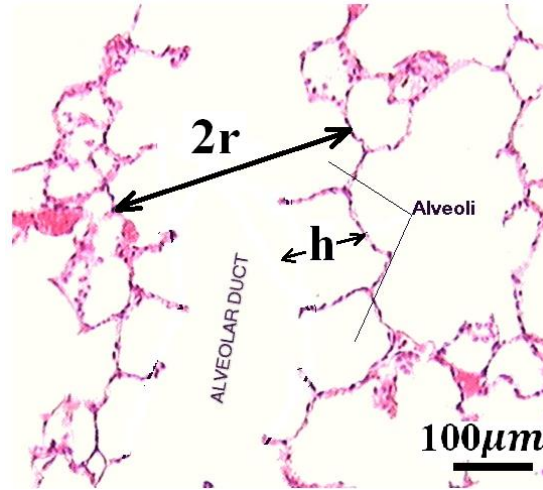


Figure 3.1 Microscope image showing morphometric parameters h and r for an alveolar duct.

Note, linear shear viscoelasticity of the solid medium will result in rate or s -dependent values for the material elastic constants. No other modifications are needed. Implementation of a shear viscoelastic model is discussed in the example case studies below. Neglecting external excitations, taking the divergence of Equation (3.1a) and not altering Equation (3.1b) yields the following

$$\left(K_b + \frac{4\mu}{3}\right) u_{j,jjj} - (\alpha - \beta) p_{,ii} = s^2 (\rho - \beta \rho_f) u_{i,i}, \quad (3.4a)$$

$$\beta p_{,ii} - \frac{\phi^2}{R} \rho_f s^2 p = \rho_f s^2 (\alpha - \beta) u_{i,i}. \quad (3.4b)$$

Taking the curl of Equation (3.1a) yields a single vector equation for shear waves. Since the curl of the gradient of a scalar always equals zero, we arrive at the following for shear waves:

$$\mu u_{i,jj} = (\rho - \beta \rho_f) s^2 u_i . \quad (3.5)$$

In the frequency domain, the complex-valued wave speed c_s and shear wave number k_s are

$$c_s = \sqrt{\mu/(\rho - \beta \rho_f)} , \quad (3.6a)$$

$$k_s = \omega/c_s . \quad (3.6b)$$

Here, the real part of k_s governs the shear wave speed and the imaginary part defines the attenuation.

The coupled equations for dilatation (compression) waves are given by the following.

$$\mu u_{i,jj} + \left(K_b + \frac{\mu}{3}\right) u_{j,ij} - (\alpha - \beta) p_{,i} = (\rho - \beta \rho_f) s^2 u_i , \quad (3.7a)$$

$$\beta p_{,ii} - \frac{\phi^2}{R} \rho_f s^2 p = \rho_f s^2 (\alpha - \beta) u_{i,i} . \quad (3.7b)$$

Without loss of generality, consider plane wave motion in the x direction, assuming there are no variations in y and z directions. The above equations simplify to the following for compression waves:

$$\bar{\alpha} u_x'' - \bar{\beta} p' = \bar{\Gamma} \ddot{u}_x , \quad (3.8a)$$

$$\bar{\Delta} p'' - \bar{\epsilon} \ddot{p} = \bar{\Omega} \dot{u}_x' , \quad (3.8b)$$

where $\bar{\alpha} = K_b + \frac{4\mu}{3}$, $\bar{\beta} = \alpha - \beta$, $\bar{\Gamma} = \rho - \beta \rho_f$, $\bar{\Delta} = \beta$, $\bar{\epsilon} = \frac{\phi^2}{R} \rho_f$, $\bar{\Omega} = \rho_f (\alpha - \beta)$, " denotes second order spatial derivative with respect to x and " " denotes second order time derivative. Assume that the plane wave motion in the x direction is oscillating at frequency ω , the displacement u_x and pressure p have the form

$$u_x = u_0 e^{j(\omega t - kx)} , \quad (3.9a)$$

$$p = p_0 e^{j(\omega t - kx)} . \quad (3.9b)$$

Inserting Equations (3.9a-b) into Equations (3.8a-b), we have the expression of u_x and p in matrix form:

$$\begin{bmatrix} \bar{\alpha} k^2 - \bar{\Gamma} \omega^2 & -j \bar{\beta} k \\ j \bar{\Omega} \omega^2 k & \bar{\Delta} k^2 - \bar{\epsilon} \omega^2 \end{bmatrix} \begin{bmatrix} u_x \\ p \end{bmatrix} = \begin{bmatrix} 0 \\ 0 \end{bmatrix} . \quad (3.10)$$

The nontrivial solution of u_x and p requires that the determinant of the coefficient matrix be zero, which leads to a quadratic equation $(\bar{\alpha}\bar{\Delta})k^4 - (\bar{\alpha}\bar{\epsilon} + \bar{\Gamma}\bar{\Delta} + \bar{\beta}\bar{\Omega})\omega^2k^2 + \bar{\Gamma}\bar{\epsilon}\omega^4 = 0$ for k^2 . This then provides for two possible solutions for k^2 , and thus positive-valued k , which are denoted as k_{ps} and k_{pf} , the slow and fast compression wave numbers. The two compression waves attenuate due to the relative motion between the solid and fluid, and due to the solid shear viscoelasticity. So, k_{ps} and k_{pf} are complex valued; the real part of k_{pf} and k_{ps} governs compression wave speed and the imaginary part defines the attenuation. The phase velocity of the fast and slow compression wave are defined as $\omega/Re(k_{pf})$ and $\omega/Re(k_{ps})$. The group velocity of the fast and slow compression wave are defined as $\frac{d\omega}{d(Re(k_{pf}))}$ and $\frac{d\omega}{d(Re(k_{ps}))}$. The phase velocity value and the group velocity value are not equal for a dispersive medium.

3.3. Comparison of Wave Speed and Attenuation Predictions

The theories described in Section 2.4.1 and 3.2 for mechanical wave motion in the lung parenchyma can be compared in terms of their predictions for wave speed and attenuation, given the set of nominal property values at 20 cm H₂O P_{ip} for the effective medium model provided in Table 3.1 and additional parameters for Biot theory provided in Table 3.2. The lung parenchyma permeability, lung skeleton bulk modulus and lung shear modulus are taken from experimental measurements described in Section 3.4.4 and 3.4.5. These comparisons are shown in Figure 3.2 and 3.3. Both theories predict a “fast” compression wave speed. The group velocity as well as the phase velocity (not plotted here) of the compression wave predicted by Biot theory increases with frequency, indicating the lung as a dispersive medium, while the effective medium theory predicts a frequency independent velocity. However, Biot theory predicts an additional slow compression wave that is not predicted by the effective medium theory. The shear wave, based on Equations (3.4a-b), is decoupled from equations for the compression waves, and as mentioned above can be implemented with either compression wave theory. The slow compression wave has a larger attenuation coefficient than the fast compression wave as shown in Figure 3.3. The

shear wave attenuation is mainly due to the material shear viscosity. However, the wave attenuation predicted by Biot theory and by thermal dissipation has significant differences. At frequencies above 1000 Hz, the thermal dissipation model predicts a much larger attenuation coefficient than the Biot theory. The wave speed and attenuation predictions will be compared with experimental measurements detailed in Section 3.4.6.

Table 3.1 Parameters for effective medium theory

ϕ	Air volume fraction	0.71	P	Air pressure	1.03×10^5 Pa
n	Polytropic constant	1	ρ_f	Air density	1.2 kg/m^3
K_s	Solid bulk modulus	2.2×10^9 Pa	ρ_s	Solid density	1000 kg/m^3

Table 3.2 Additional parameters for Biot theory

a	Pore radius	0.225 mm	τ	Tortuosity	1.33
κ_p	Permeability	$25.32 \times 10^{-12} \text{ m}^2$	μ_f	Air viscosity	$1.82 \times 10^{-5} \text{ Pa}\cdot\text{s}$
K_b	Solid skeleton modulus bulk	8.26×10^3 Pa	ρ_s	Solid shear modulus	$1400 + 5.78(j\omega)^{0.5}$ Pa

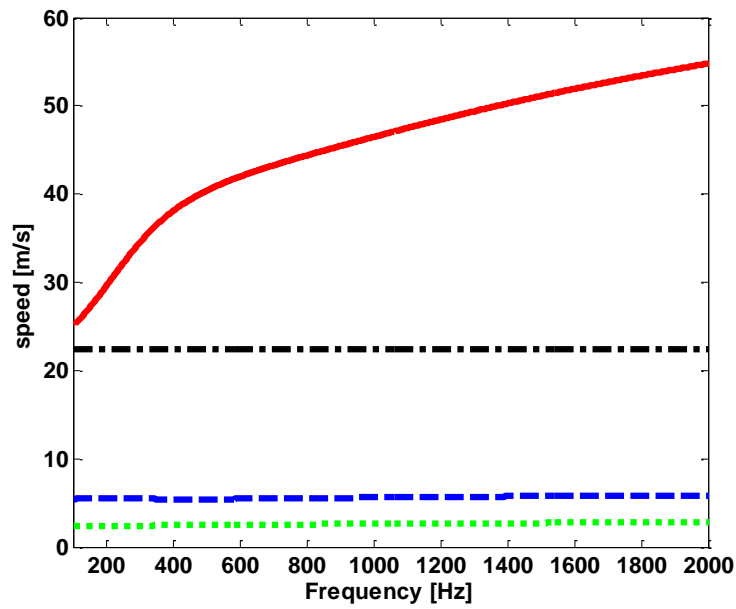


Figure 3.2 Compression and shear wave group velocity at 20 cm H_2O P_{tp} , — fast compression wave, Biot theory, — slow compression wave, Biot theory, — — compression wave, effective medium model, - - - shear wave, Biot theory.

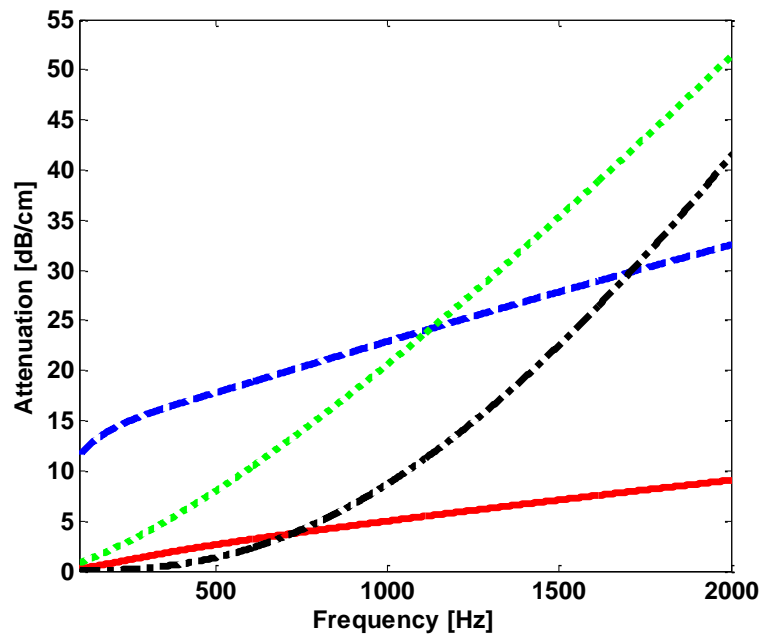


Figure 3.3 Compression and shear wave attenuation at 20 cm H_2O P_{tp} , — fast compression wave, Biot theory, — slow compression wave, Biot theory, — — compression wave, thermal dissipation model, - - - shear wave, Biot theory.

3.4. Ex Vivo Experimental Studies on Pig Lung

3.4.1. Lung Preparation

Experiments detailed in Section 3.4 (except Section 3.4.3) were carried out on the lung of a freshly sacrificed pig that weighed 33 kg. Immediately upon sacrifice the lung was inflated by air with positive pressure of 20 cm H₂O gage. As the chest cavity was surgically opened and pleural pressure became atmospheric pressure, the transpulmonary pressure (P_{tp} , airway pressure relative to pleural or atmospheric pressure) was maintained at 20 cm H₂O. It was observed that all the lung lobes were uniformly inflated and no noticeable amounts of gas trapping were found under the pleural membrane. The lung was removed from the chest of the pig, blood drained, and placed on a vibration isolated test bench in a room maintained at 20°C. The sequence of experiments on the lung included: mechanical indentation measurements, surface wave measurements and compression wave measurements. After the above measurements, the lung volume was measured by water displacement and the lung mass was also measured. The time range of these measurements postmortem was about 0.5-1 hours, 1-1.5 hours, 1.5-2 hours and 2-2.25 hours, respectively. During this time the lung was periodically sprayed with water to keep the surface moist. Separately, permeability measurements were made on dried specimens of porcine lung (Section 3.4.3).

3.4.2. Mass and Air Volume Fraction of Inflated Lung

As the air volume fraction and the permeability will be used to calculate the fast wave speed from Biot theory and compared with experiments, measurements on these two parameters are first reported. The mass of the pig lung at zero P_{tp} was 331 g. As the soft tissue density is very close to 1 g/cm³, the soft tissue volume was taken to be 331 cm³. The total volume of the lung at 20 cm H₂O and 10 cm H₂O was 1141 cm³ and 770 cm³; so, the air volume fraction of the lung was 71% and 57%, respectively.

3.4.3. Permeability Measurement on Dried Pig Lung

Permeability is a measure of the ability of a porous material to allow fluids to pass through it. It is an important parameter that affects the compression wave speeds and attenuation in the Biot theory. It is part of the proportionality constant in Darcy's law which relates discharge (flow rate) and fluid physical properties (e.g. viscosity) to a pressure gradient applied to the porous media; it is defined as

$$\kappa_p = v \frac{\mu_f \Delta x}{\Delta p}, \quad (3.11)$$

where v is the superficial fluid flow velocity through the medium (i.e., the average velocity calculated as if the fluid were the only phase present in the porous medium), μ_f is the dynamic viscosity of the fluid, Δp is the applied pressure difference and Δx is the thickness of the porous medium. As any piece of lung parenchyma cut from an inflated fresh lung will collapse and can't keep its shape, dry-preserved swine lung pieces (LS03686, Nasco, Fort Atkinson, WI) were used to estimate lung parenchyma permeability. The dry-preserved lung was inflated to its maximum volume and dried by the manufacturer. Cylindrical samples were carefully cut from dry-preserved lung pieces and clearly visible airways were avoided as best as possible to keep the test samples close to a homogeneous and isotropic medium. The test sample was put into a plastic test tube and connected to an air flow source with constant volume flow rate. The pressure difference at two ends of the sample was measured by a differential pressure manometer (HD 750, Extech, Nashua, NH). The downstream volume flow rate was measured by a Visi-Float® flowmeter (Series VFB, Dwyer Instruments, Michigan City, IN). The experimental setup is shown in Figure 3.4. The superficial fluid flow velocity was calculated by dividing the volume flow rate by the test sample cross-sectional area. For each test sample, experiments were carried out for five pressure differences and the permeability was estimated from Equation (3.11).

For the permeability measurement, different superficial fluid flow velocities and applied pressure differences form a good linear relationship for each dried lung sample. The lung parenchyma permeability with its mean and standard deviation is shown in Table 3.3. The average value of the permeability of the four samples is $25.32 \times 10^{-12} \text{ m}^2$ and this is taken as an approximation of the parenchymal permeability

value at 20 cm H₂O. As $\kappa_p \propto \phi^3 S/\tau$, the lung permeability at different P_{tp} s is different. The pore space in the lungs is the respiratory tree, which is composed of the conducting airways and the respiratory zone (the respiratory bronchioles, the alveolar ducts, alveolar sacs and alveoli). The length and diameter of the conducting airways and the respiratory bronchioles almost remain the same over the range of different P_{tp} s; so, the tortuosity is approximated as a constant. Although there are still many inconsistencies in the literature regarding alveolar surface area at different P_{tp} , in a recent study Hajari et al. [22] demonstrated that, by using the ³He MRI technique, the healthy human lungs inflate primarily by alveolar recruitment combined to a lesser extent with anisotropic expansion of alveolar ducts. From their study, the alveolar surface area changes little with pressure. So the pore surface area for the lungs may not significantly affect the permeability. Then from $\kappa_p \propto \phi^3 S/\tau$ and by considering the change of air volume fraction, the permeability of the lung parenchyma at 10 cm H₂O is $13.10 \times 10^{-12} \text{ m}^2$.

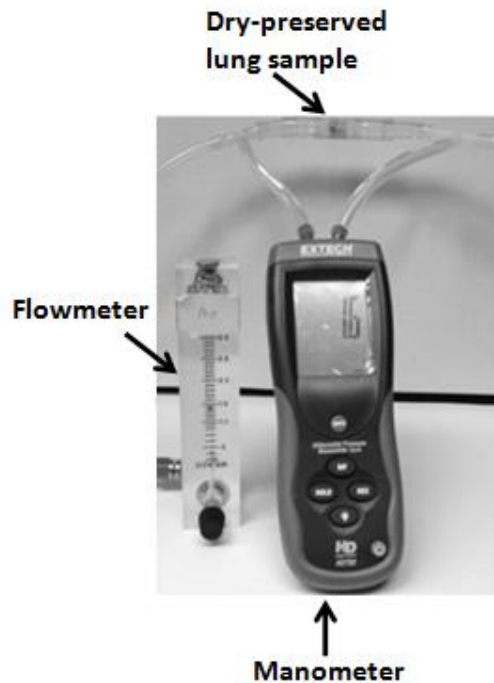


Figure 3.4 Experimental setup for lung parenchyma permeability measurement.

Table 3.3 Lung parenchyma permeability

Sample #	Diameter (cm)	Length (cm)	Permeability ($\times 10^{-12} \text{m}^2$)(mean \pm std)
1	1.50	1.60	32.30 ± 1.95
2	1.50	1.45	21.75 ± 0.61
3	0.98	1.20	26.24 ± 1.33
4	0.98	1.00	21.00 ± 0.89

3.4.4. Mechanical Indentation Tests on the Lung

A mechanical indentation test was performed to determine the lung shear modulus at two different P_{tp} 's. A steel cylindrical indenter with a 1.1 cm diameter was indented on the surface of the cranial lobe. The increment in displacement (a) was 0.25 mm and the maximum displacement was kept to 1.5 mm to ensure small deformation. The displacement was measured by a micrometer and the applied force F was measured by a digital force gauge (DS2-1, Imada, Northbrook, IL). By taking the Poisson's ratio of the lung as $\nu_1 = 0.42$ and from Equations (2.10-2.11) the relaxed shear modulus μ_0 of the lung can be calculated. The applied force and displacement relation for the indentation measurements is shown in Figure 3.5. From Equation (2.11), the lung shear modulus is estimated to be 1.40 kPa and 0.79 kPa at 20 cm H₂O and 10 cm H₂O, respectively.

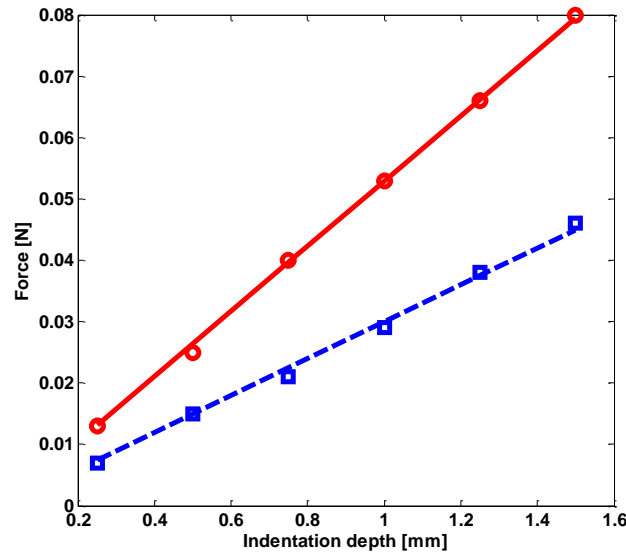


Figure 3.5 Force and indentation depth relation in indentation measurement, $\circ \circ \circ$ experiment, 20cm H₂O, — least square fit, 20cm H₂O, $\square \square \square$ experiment, 10cm H₂O, - - least square fit, 10cm H₂O.

3.4.5. Surface Wave Measurements

Surface wave propagation on the inflated lung surface was measured the same way as described in Section 2.4.2. The frequencies of sinusoidal excitation were from 100 Hz to 600 Hz with an increment of 100 Hz. The measurements were taken at 20 cm H₂O and 10 cm H₂O P_{tp}. Scanning was along two adjacent lines radially outward from the excitation area over a distance of 25 mm with a 2.5 mm increment and the measurement point closest to the excitation was 5 mm from the rim of the plexiglass disk. The experimental setup is the same as that in Section 2.4.2.

The measured surface wave speed at each P_{tp} is plotted in Figure 3.6. For the band of frequencies analyzed here, it was found that the fractional Voigt model [23, 24] with fractional order $\alpha = 0.5$ provided a reasonable fit to experimental data and only requires optimization of one parameter μ_α based on surface wave measurements (as μ_0 was determined by the indentation tests). By optimizing μ_α , the fitting curve of the surface wave speed is also plotted in Figure 3.6 for each P_{tp}. In Figure 3.6, the measured surface wave speed along lines 1 and 2 are close to each other; the small discrepancy between the values of the two lines is likely caused by non-homogeneity of the lung tissue. An approximate relation between surface wave and shear wave speed is [Graff 1991]

$$c_R = (0.87 + 1.12\nu_1)/(1 + \nu_1)c_s = (0.87 + 1.12\nu_1)/(1 + \nu_1) \sqrt{\frac{2}{\rho} \frac{\mu_R^2 + \mu_I^2}{\mu_R + \sqrt{\mu_R^2 + \mu_I^2}}} . \quad (3.12)$$

The surface wave speeds along the two lines were averaged and used to fit Equation (3.12) in a least square error sense to obtain the optimal values of μ_R and μ_I . The fitting curves at each P_{tp} are also plotted in Figure 3.6. Using Equation (2.4a-b) and known μ_0 from the indentation tests, the shear viscosity μ_α can be calculated from μ_R or μ_I . At 20 cm H₂O and 10 cm H₂O P_{tp}, $\mu_\alpha = 5.78 \text{ Pa} \cdot \text{s}^{1/2}$ and $\mu_\alpha = 1.23 \text{ Pa} \cdot \text{s}^{1/2}$, respectively. When the frequency approaches zero, the shear wave speed approaches $\sqrt{\mu/\rho}$.

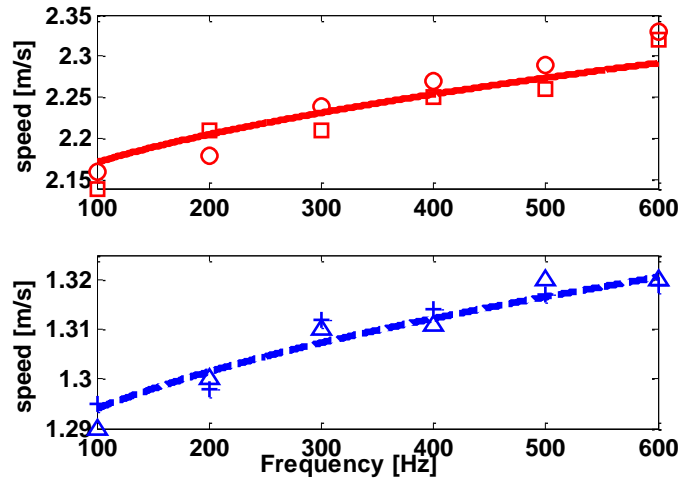


Figure 3.6 Surface wave speed, $\circ \circ \circ$ experiment, 20cm H₂O, line 1, $\square \square \square$ experiment, 20cm H₂O, line 2, — Fractional Voigt model least square fit, 20cm H₂O, $\triangle \triangle \triangle$ experiment, 10cm H₂O, line 1, $+++$ experiment, 10cm H₂O, line 2, - - Fractional Voigt model least square fit, 10cm H₂O.

3.4.6. Compression Wave Measurements

The same power amplifier, electromagnetic shaker and impedance head were used in compression wave studies. A twenty cycle tone burst signal was generated from a dynamic signal analyzer (SignalCalc ACE, Data Physics, San Jose, CA) and was fed into the power amplifier that was connected to the electromagnetic shaker. The impedance head was mounted on the shaker with its end connected to a plexiglass disk with radius of 15 mm which in turn was gently pressed against the inflated and excised lung's surface. The frequencies of the tone burst signal were from 100 Hz to 2000 Hz. A point on the lung surface was driven by the plexiglass disk and its acceleration was measured by the impedance head. Out-of-plane velocity of the point on the other side of lung surface was measured by a laser Doppler vibrometer (LDV) (PDV-100, Polytec, Irvine, CA). The measurements were taken at cranial lobes as they provide enough space for the full contact between the plexiglass disk and the lung surface. The distance between the point at the center of the plexiglass disk and the point measured by LDV was measured by a caliper to the nearest tenth of a mm. The acceleration and velocity measurements were recorded by the same signal analyzer with a sampling frequency of 102.4 kHz. The wave speeds were measured at three locations (each location twice) at each P_{ip} . The schematic diagram and the

experiment set up are shown in Figure 3.7 and 3.8. The acceleration measured on one side of the lung surface was regarded as the input signal $x(t)$, the velocity measured on the other side of the lung surface was numerically differentiated and the resulting acceleration was regarded as the output signal $y(t)$. The cross-correlation function $R_{xy}(\tau)$ of the two signals is calculated by

$$R_{xy}(\tau) = \lim_{T \rightarrow \infty} \frac{1}{T} \int_0^T x(t)y(t + \tau)dt . \quad (3.13)$$

τ_1 was found to be the peak location of the $R_{xy}(\tau)$ curve. Thus the transit time τ_2 of the compression wave traveling at a constant velocity between two points on the lung surface is

$$\tau_2 = \tau_1 - \tau_3. \quad (3.14)$$

where τ_3 is the time delay of the LDV which is 1.243 ms (per the manufacturer and in agreement with calibration measurements taken in our lab). The compression wave speed is then given by d/τ_2 , where d is the distance between two points. Since the excitation signal is a narrow-banded finite-duration oscillatory pulse, this excitation waveform propagates undistorted in shape and at the group velocity [25]; thus, the estimated wave speed is the group velocity of compression waves propagating in the lungs.

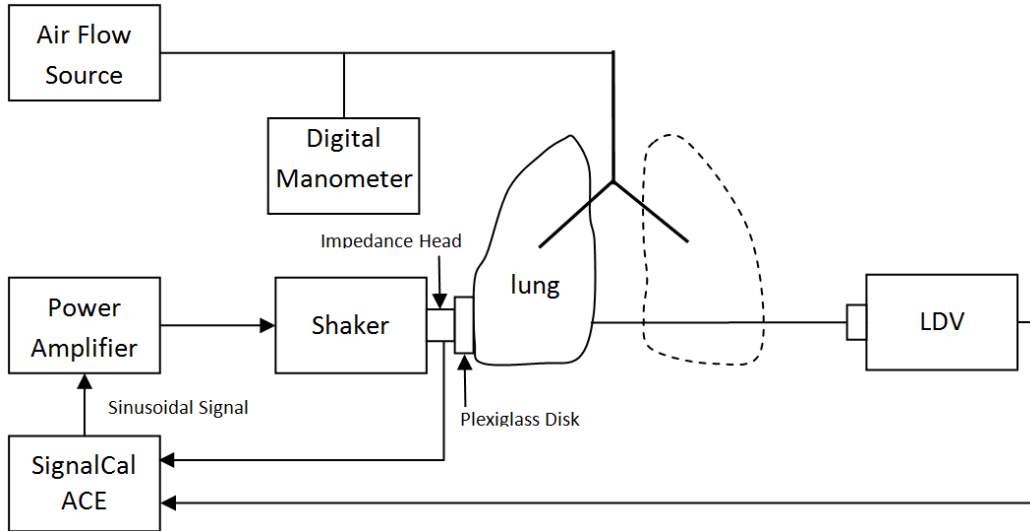


Figure 3.7 Schematic diagram of compression wave measurement.

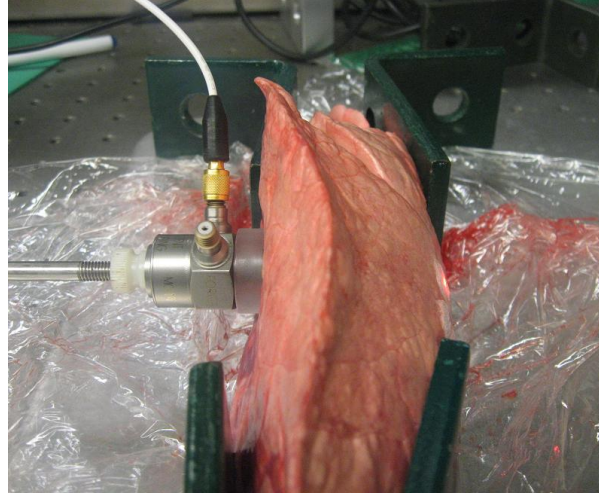


Figure 3.8 Experiment set up of compression wave measurement.

Due to complex geometries of the lungs, wave reflection/transmission at the lung and air interface, attenuation estimated from the velocity measured by the LDV with respect to the reference acceleration will be unreliable; so, two subminiature microphones (BL-21785-000 Knowles Electronics, Itasca, IL) were used to measure the wave attenuation. The image and dimension of the microphone is shown in Figure 3.9. As it is very difficult to have planar compression waves throughout the lung, having spherical compression waves throughout the lung will make easier separation of the attenuation due to geometric spreading from total attenuation. To achieve this, the plexiglass disk with a radius of 1 cm connected to a shaker was replaced by a hose with a radius of 3.1 mm connected to a 3.5 inch speaker (PDWR30W, PylePro, Brooklyn, NY). A needle with an inner diameter of 0.413 mm was inserted into the lung at the same height as that of the sound input. The needle end was connected to a 50 mm long hose and the pressure was measured by the microphone through the hose. The data acquisition system remained the same. The experiment set up is shown in Figure 3.10. The measurements were taken at three different locations (each location twice) at each P_{tp} . The pressure amplitudes at two measurement points (except the near field) have the form

$$p_1 = \frac{A}{r_1} e^{-k_I r_1}, \quad (3.15a)$$

$$p_2 = \frac{A}{r_2} e^{-k_I r_2}, \quad (3.15b)$$

where A is an arbitrary constant, k_I is the imaginary part of the wave number and r_1 and r_2 are the distances of the measurement points from the sound input. From Equation (3.15a-b), the attenuation (dB/m) is

$$Att = \left[20 \log_{10} \left(\frac{p_1 r_1}{p_2 r_2} \right) \right] / (r_2 - r_1). \quad (3.16)$$

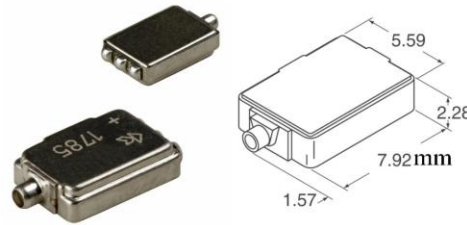


Figure 3.9 Photo and dimension of subminiature microphone BL-21785-000.

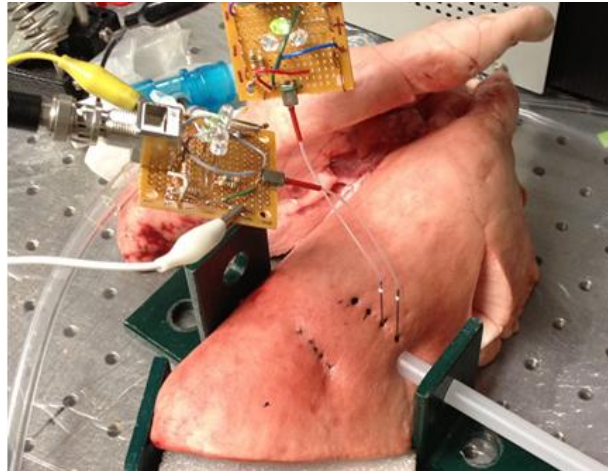


Figure 3.10 Experiment setup of compression wave attenuation measurement.

From the compression wave studies, the time history of the acceleration and velocity of a point at 400 Hz is shown in Figure 3.11. The distance between two points was 33.2 mm at 10 cm H₂O. The amplitude of the velocity is very small; so it was increased by 2000 times for ease of viewing in the figure.

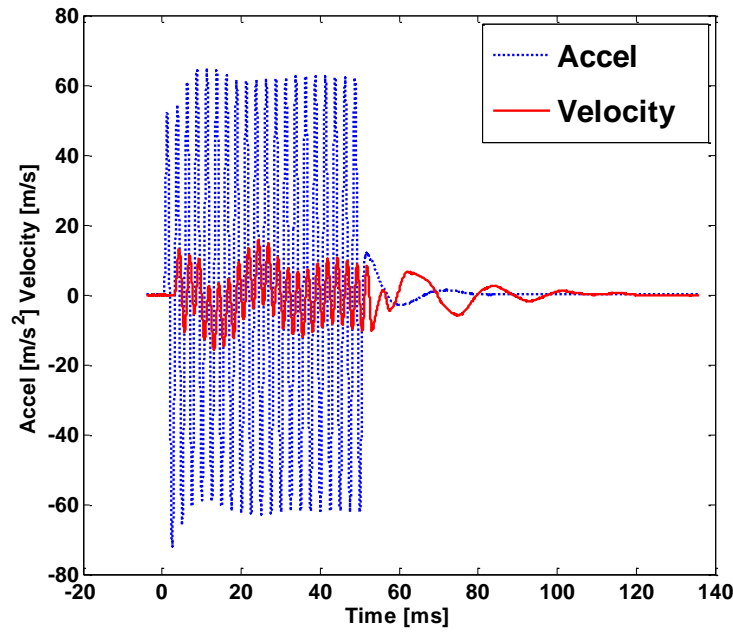


Figure 3.11 Time history of the acceleration and velocity of a point at 400 Hz with 10 cm H₂O. The amplitude of the velocity is increased by 2000 times for ease of viewing here.

From Figure 3.11, it is observed that there is only one type of compression wave (fast wave) propagating in the lung parenchyma while the slow wave is not observed. This can be explained as follows. In Biot theory, it is assumed that the flow of the fluid relative to the solid through the pores is of the Poiseuille type. For Poiseuille flow in a porous medium the characterizing boundary layer is known as the viscous skin depth d_s , and it is expressed as [21]

$$d_s = (2\mu_f/\rho_f\omega)^{1/2}. \quad (3.17)$$

The assumption of Poiseuille flow fails when d_s is equal to or greater than the pore radius. It is very important for the observation of the slow wave that d_s should be much smaller than the pore radius as the relative motion of the solid and the fluid is not impeded by viscous drag so that the slow wave can propagate [21]. In our frequency range of interest (100-2000 Hz), d_s ranges from 0.05 to 0.22 mm. The typical pore radius is the alveolar duct radius which is around 0.25 mm. The slow compression wave was first observed by Plona in water-saturated disks composed of sintered glass spheres with diameters between 0.21 and 0.29 mm [26]. Slow wave velocity measurements were made using the 500 kHz

transducer pair. So from Equation (3.17), the viscous skin depth d_s is $0.8 \mu\text{m}$ and the sphere radius is about 300 times of d_s . The slow compression wave was also observed in water-saturated bovine plexiform and human Haversian bone [27]. To observe the slow wave, the lowest frequency in bovine plexiform bone cut perpendicular to longitudinal direction is 0.73 MHz and the radius (round 0.02 mm) of the main canals for blood supply is taken as the pore size. Thus d_s is $0.66 \mu\text{m}$ and the pore size is about 30 times of d_s . However, in the current experiment d_s is not small enough compared with the pore radius so it is not possible to observe the slow compression wave in our frequency range of interest. Under very high frequencies, it might also be impossible to observe the slow wave as it attenuates faster than at lower frequencies.

The measured compression wave speed (group velocity) at 20 cm H₂O and 10 cm H₂O are shown in Figure 3.12. The theoretical predictions by Biot theory and the effective medium model are also plotted for comparison. The signals measured by the microphone have much more noise than those from the LDV and hence they were not used to estimate the wave speed. In order to have a good estimate of the true mean of the compression wave speed in the lung parenchyma based on a finite-sized sample, a 95% confidence interval is used as a quantified measure of the random error in the estimate of the true value of the compression wave speed. Thus, the estimate of the true mean value based on a finite data set experiment is stated as

$$c_p' = \bar{c}_p \pm t_{5,95} S_{\bar{c}_p}, \quad (3.18)$$

where $t_{5,95}$ is the estimator of the Student's t distribution with 0.95 probability and 5 degrees of freedom. $S_{\bar{c}_p}$ is the standard deviation of the means and is defined as $S_{\bar{c}_p} = S_{c_p} / \sqrt{N}$ with S_{c_p} as the sample standard deviation and N as the sample size of six.

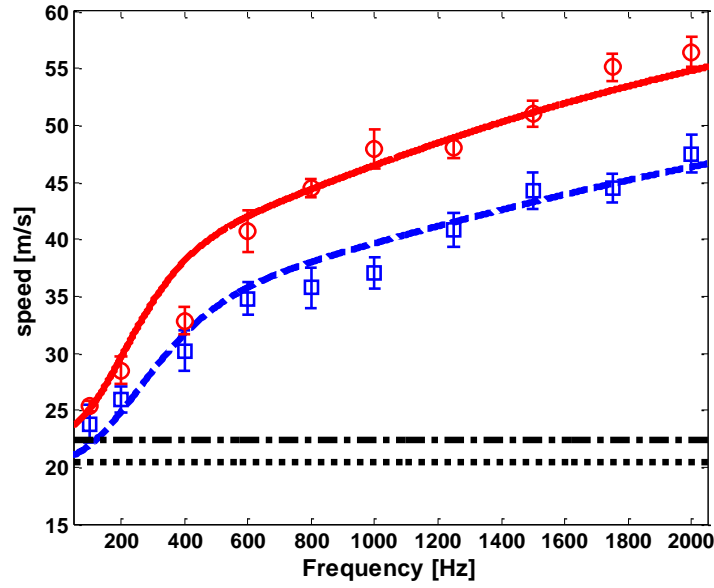


Figure 3.12 Fast compression wave group velocity, $\circ \circ \circ$ experiment, 20cm H₂O, — Biot theory, 20cm H₂O, — effective medium model, 20cm H₂O, $\square \square \square$ experiment, 10cm H₂O, - - Biot theory, 10cm H₂O, - - - effective medium model, 10cm H₂O. Bars on experiment denote 95% confidence interval.

The parameters used for theoretical predictions are listed as follows. The air density at 20°C is $\rho_f = 1.2 \text{ kg/m}^3$. The air pressure in the lung at 20 cm H₂O and 10 cm H₂O is $1.03 \times 10^5 \text{ Pa}$ and $1.02 \times 10^5 \text{ Pa}$, respectively. The soft tissue density is $\rho_s = 1000 \text{ kg/m}^3$, the tissue bulk modulus is taken to be that of the water as $K_s = 2.2 \text{ GPa}$. Air viscosity at 20°C is $\mu_f = 1.82 \times 10^{-5} \text{ Pa} \cdot \text{s}$. The complex shear modulus of the lung is $\mu = 1400 + 5.78(j\omega)^{1/2} \text{ Pa}$ and $\mu = 790 + 1.23(j\omega)^{1/2} \text{ Pa}$ at 20 cm H₂O and 10 cm H₂O, respectively. The solid skeleton bulk modulus K_b is 1.40 kPa and 0.79 kPa at 20 cm H₂O and 10 cm H₂O, respectively. The pore size also affects the fast compression wave speed. Using the ³He MRI technique, Hajari et al. [22, 28] demonstrated that the alveolar duct radius of both human and dog lung increases with pressure. As the weight of the pig used in this experiment was close to that of the dog, we took the alveolar duct radius as 0.225 mm at 20 cm H₂O and 0.2 mm at 10 cm H₂O from the measurements made by Hajari. The polytropic constant is taken as $n=1$. This fits the wave speed in the experiments better than $n=1.41$. In the attenuation results below, $n=1$ also has a better fit. As mentioned above, n can be between 1 and 1.41. Since the bulk modulus of the lung tissue is about five times the

order of magnitude of that of the air, from Equation (2.18b), the bulk modulus of the lung is approximately nP/ϕ . Yen et al. [29] measured the compression wave speed, density and the bulk modulus of the rabbit lung. From their measured lung density and bulk modulus, the polytropic constants at the different P_{tp} used here are close to 1.09, which supports our reasonable choice of $n=1$. The polytropic constant was also $n=1$ in Wodicka et al. [14]. It is observed in Figure 3.12 that the compression wave speed increases with frequency and these trends agree well with the Biot theory prediction. As P_{tp} increases from 10 cm H₂O to 20 cm H₂O, the Biot theory also predicts a larger wave speed, which is confirmed from the experiment. The effective medium model predicts a frequency independent wave speed and the values it predicts are lower than those of Biot theory. For frequencies higher than 2000 Hz, the low LDV SNR makes the estimation of the transit time unreliable; thus, 2000 Hz was the highest excitation frequency in the current experimental protocol.

The attenuation of the compression wave at 20 cm H₂O and 10 cm H₂O are shown in Figure 3.13. The theoretical predictions by Biot theory and the effective medium theory are also plotted for comparison. As the signals with poor SNR were discarded, only two measurements with different microphone distances were shown for each pressure. The Biot theory prediction has a relatively good match with the experiments while the thermal damping predictions from the effective medium theory do not provide a good match. As seen from Figure 3.13, above 300 Hz the attenuation at 10 cm H₂O is larger than that of 20 cm H₂O. This attenuation increase likely arises from the increase of friction between the alveolar duct wall and the air. Microscopically, the increase of friction is due to the significant drop of permeability which increases the pressure gradient along the pore space. As $\kappa_p \propto \phi^3 S/\tau$ and assuming that the alveolar duct radius increases with the air volume fraction, the attenuation has a maximum at a certain air volume fraction based on the Biot theory prediction. Using the parameters above, the maximum attenuation shifts from an air volume fraction of 0.68 to 0.5 as the frequency increases from 100 to 2000 Hz. At frequencies above 1000 Hz, the maximum attenuation occurs at a volume fraction slightly less than 0.57 (air volume fraction at 10 cm H₂O); so, the attenuation coefficient at 20 cm H₂O is significantly smaller than that at 10 cm H₂O. The discrepancies between the experimental measurements

and the Biot theory prediction show that even though the viscous dissipation is the major source of dissipation for fast compression wave in the lungs, there likely are other non-negligible sources of dissipation, including thermal dissipation. In summary, in terms of the compression wave speed and attenuation in the lungs, the Biot theory yields a better prediction than the effective medium theory and the thermal dissipation model.

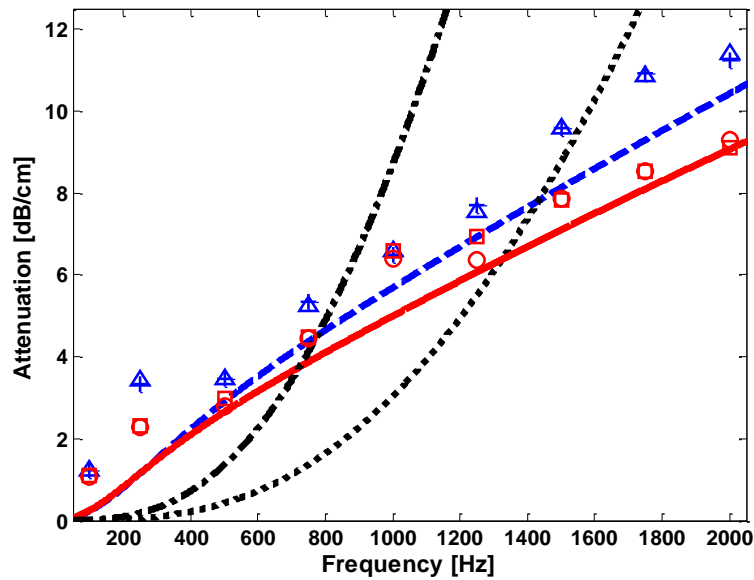


Figure 3.13 Fast compression wave attenuation, ○ ○ ○ experiment, 20cm H₂O, location 1, □ □ □ experiment, 20cm H₂O, location 2, — Biot theory, 20cm H₂O, --- effective medium model, 20cm H₂O, △ △ △ experiment, 10cm H₂O, location 1, + + + experiment, 10cm H₂O, location 2, — Biot theory, 10cm H₂O, --- effective medium model, 10cm H₂O.

3.5. Discussion

Two theoretical models of the vibro-acoustic behavior of the lung parenchyma are compared: (1) an effective medium theory for compression wave behavior in the lung and (2) the Biot theory applied to wave propagation in the lung. A fractional derivative formulation of viscoelasticity is integrated into both models. A measurable “fast” compression wave speed predicted by the Biot theory formulation has a significant frequency dependence which is not predicted by the effective medium theory. Biot theory also predicts a slow compression wave and a shear wave. The frequency dependent compression wave group velocity was measured experimentally from 100 to 2000 Hz by applying narrow-banded pulses on freshly

excised pig lung ex vivo. Both the experimentally measured fast compression wave speed and attenuation in an ex vivo pig lung model agreed well with the Biot theory. To obtain the parameters for Biot theory prediction: mechanical indentation tests were performed to measure the relaxed shear modulus of the lung; surface wave measurements were performed to estimate lung tissue shear viscoelasticity; and, lung permeability was separately measured on dried lung specimens. The slow compression wave was not observed in the experiment as the relative motion of the solid and the fluid was impeded by viscous drag due to the relatively large viscous skin depth in the frequency range considered. Compression wave propagation in the lungs has been primarily studied below several hundred Hz and limited information about wave speed versus frequency has been obtained. In the current study compression wave speed measurements were extended to 2000 Hz revealing that the lung is a dispersive medium for both compression and shear waves. This study suggests that the Biot theory may provide a more robust and accurate model than the effective medium theory for wave propagation in the lungs over a wider frequency range.

3.6. References

1. Chen Q, Mai VM, Bankier AA, Napadow VJ, Gilbert RJ, Edelman RR, 2001, Ultrafast MR grid-tagging sequence for assessment of local mechanical properties of the lungs, *Magn. Reson. Med.* 45(1), pp. 24-28.
2. Napadow VJ, Mai, VM, Bankier AA, Gilbert RJ, Edelman RR, Chen Q, 2001, Determination of regional pulmonary parenchymal strain during normal respiration using spin inversion tagged magnetization, *J. Magn. Reson. Imag.* 13(3), pp. 467-474.
3. Kompis M, Pasterkamp H, Wodicka GR, 2001, Acoustic imaging of the human chest, *Chest*, 120, pp. 1309-1321.
4. Goss BC, McGee KP, Ehman RC, Manduca A, Ehman RL, 2006, Magnetic resonance elastography of the lung: technical feasibility, *Magn. Reson. Med.* 56, pp. 1060–1066.

5. McGee KP, Hubmayr RD, Ehman RL, 2008, MR elastography of the lung with hyperpolarized ^3He , *Magn. Reson. Med.* 59, pp. 14–18.
6. McGee KP, Lake D, Mariappan Y, Hubmayr RD, Manduca A, Ansell K, Ehman RL, 2011, Calculation of shear stiffness in noise dominated magnetic resonance elastography data based on principal frequency estimation, *Phys. Med. Biol.* 56, pp. 4291–4309.
7. Mariappan YK, Kolipaka A, Manduca A, Hubmayr RD, Ehman RL, Araoz P, McGee KP, 2012, Magnetic resonance elastography of the lung parenchyma in an in situ porcine model with a noninvasive mechanical driver: correlation of shear stiffness with trans-respiratory system pressures, *Magn. Reson. Med.* 67, pp. 210–217.
8. Sinkus R, Tanter M, Xydeas T, Catheline S, Bercoff J, Fink M, 2005, Viscoelastic shear properties of in vivo breast lesions measured by MR elastography, *Magn. Reson. Imag.* 23(2), pp. 159-165.
9. Shah NS, Kruse SA, Lager DJ, Farell-Baril G, Lieske JC, King BF, Ehman RL, 2004, Evaluation of renal parenchymal disease in a rat model with magnetic resonance elastography, *Magn. Reson. Med.* 52(1), pp. 56-64.
10. Kemper J, Sinkus R, Lorenzen J, Nolte-Ernsting C, Stork A, Adam G, 2004, MR elastography of the prostate: initial in-vivo application, *Rofo*, 176(8), pp. 1094-1099.
11. Jenkyn TR, Ehman RL, An K, 2003, Noninvasive muscle tension measurement using the novel technique of magnetic resonance elastography (MRE), *J. Biomech. Eng.* 36(12), pp. 1917-1921.
12. Klatt D, Hamhaber U, Asbach P, Braun J, Sack I, 2007, Noninvasive assessment of the rheological behavior of human organs using multifrequency MR elastography: a study of brain and liver viscoelasticity, *Phys. Med. Biol.* 52, pp. 7281–7294.
13. Rice DA, 1983, Sound speed in pulmonary parenchyma, *J. Appl. Physiol.* 54, pp. 304–308.
14. Wodicka GR, Stevens KN, Golub HL, Cravalho EG, Shannon DC, 1989, A model of acoustic transmission in the respiratory system, *IEEE Trans. Biomed. Eng.* 36, pp. 925 – 34.

15. Royston TJ, Zhang X, Mansy HA, Sandler RH, 2002, Modeling sound transmission through the pulmonary system and chest with application to diagnosis of a collapsed lung, *J. Acous. Soc. Amer.* 111, pp. 1931 – 1946.
16. Siklosi M, Jensen OE, Tew RH, Logg A, 2008, Multiscale modeling of the acoustic properties of lung parenchyma, *ESAIM: Proc.* 23, pp. 78-97.
17. Biot MA, 1956, Theory of propagation of elastic waves in a fluid saturated porous solid. I Low frequency range, *J. Acous. Soc. Amer.* 28(2), pp. 168-178.
18. Biot MA, 1956, Theory of propagation of elastic waves in a fluid saturated porous solid. II Higher frequency range, *J. Acous. Soc. Amer.* 28(2), pp. 179-191.
19. Schanz, M, 2001, *Wave propagation in viscoelastic and poroelastic continua: a boundary element approach*, Springer, Berlin.
20. Bonnet G, Auriault JL, 1985, Dynamics of saturated and deformable porous media: homogenization theory and determination of the solid-liquid coupling coefficients, in *Physics of finely divided matter*, Springer, Berlin.
21. Bourbie T, Coussy O, Zinszner B, 1987, *Acoustics of porous media*, Gulf Publishing Company, Huston, TX.
22. Hajari AJ, Yablonskiy DA, Sukstanskii AL, Quirk JD, Conradi MS, WoodsJC, 2012, Morphometric changes in the human pulmonary acinus during inflation, *J. Appl. Physiol.* 112, pp. 937-943.
23. Royston TJ, Dai Z, Chaunsali R, Liu Y, Peng Y, Magin RL, 2011, estimating material viscoelastic properties based on surface wave measurements: a comparison of techniques and modeling assumptions, *J. Acous. Soc. Amer.* 130(6), pp. 4126-4138.
24. Yasar TK, Royston TJ, Magin RL, 2012, Wideband MR elastography for viscoelasticity model identification, *Magn. Reson. Med.* doi: 10.1002/mrm.24495.
25. Graff KF, 1991, *Wave motion in elastic solids*, Dover Publication, New York.

26. Plona TJ, 1980, Observation of a second bulk compressional wave in a porous medium at ultrasonic frequencies, *Appl. Phys. Lett.* 36, pp. 259-261.
27. Lakes R, Yoon HS, Katz JL, 1983, Slow compressional wave propagation in wet human and bovine cortical bone, *Science*, 220(4596), pp. 513-515.
28. Hajari AJ, Yablonskiy DA, Quirk JD, Sukstanskii AL, Pierce RA, Desl   G, Conradi MS, Woods JC, 2011, Imaging alveolar-duct geometry during expiration via ^3He lung morphometry, *J. Appl. Physiol.* 110, pp. 1448–1454.
29. Yen RT, Fung YC, Ho HH, Buttermann G, 1986, Speed of stress wave propagation in lung, *J. Appl. Physiol.* 61, pp. 701–705.

CHAPTER 4

Sound Transmission in Airways and Coupling to Lung Parenchyma

4.1. Introduction

In modeling the transmission of sound throughout the pulmonary system and chest region, the system may be viewed as having two main components:

- (1) transmission of sound through the tracheobronchial tree and,
- (2) coupling to and transmission through the surrounding biological tissues to reach the chest surface – namely the parenchyma, free air or water/blood region (in the case of a pneumothorax or hydro/hemothorax), surrounding muscle and rib cage regions, and outer soft tissues.

Many studies have focused on the transmission of sound in the respiratory tract, the tracheobronchial airway tree, with some also considering coupling to modes of wave propagation in the parenchyma [1-5]. Many have considered acoustic impedance of the tree, air excitation, and response measurement at the mouth or just below the glottis or some combination of these locations with and without endotracheal intubation, and/or resulting pressure distributions throughout the tree and parenchyma, itself. In these cases, it has been shown that a 1D branching waveguide representation of the trachea and bronchial airways with compliant walls reasonably approximates most of the dynamic behavior up to several kHz. At higher frequencies the 1D quasi-planar wave propagation assumption begins to lose validity in the larger airways. Below 100 Hz vibratory wave propagation in the parenchyma is more a function of the elastic and inertial properties of the solid tissue only and the acoustic response of the bronchial tree can be reasonably approximated as a capacitive load [6].

Transmission through the surrounding biological tissues to reach the chest surface has, arguably, received less attention. Previous studies of this part of the problem have assumed simplified geometries and homogenized material properties [7-9]. Wodicka et al. [7] assumed an axisymmetric cylindrical geometry, with the outer tissue regions of the chest treated simply as a mass load on the parenchyma. In Vovk et al. [8], an axisymmetric layered model for the torso region is used that includes annular regions for the parenchyma, rib cage region, soft outer tissue and skin. In Royston et al. [9], simplifications of

both airway and tissue structures were imposed that resulted in an axisymmetric assumption or two-dimensional planar model assumption that could be easily handled with finite element analysis. The benefit of coupling an array measurement on the surface with an improved computational model of sound propagation within the torso was demonstrated fundamentally in Ozer et al. [10]. In phantom studies, it was shown that the use of a computational boundary element model of lung acoustics combined with a surface array measurement, was significantly superior in identifying the dominant source location of the sound as compared to a simple “ray acoustics” model that neglects the more complex nature of sound transmission in a finite and complex dimensioned structure. In Acikgoz et al. [11] an acoustic boundary element model was used to simulate sound propagation in the lung parenchyma and surrounding chest wall. The simulations were compared with experimental studies on lung-chest phantom models that mimic the lung pathology of pneumothorax. Studies quantified the effect of the simulated lung pathology on the resulting acoustic field measured at the phantom chest surface. Wochner et al. [12] used a two-fold symmetric model to study lung response to underwater sound by the finite element method.

In this chapter of the dissertation, sound propagation in the subglottal region including the trachea and the lung is studied. Experiments and simulations were first performed on a tissue-mimicking phantom for sound coupling into the lung parenchyma. Then the human airway tree is simplified to an airway tree including the trachea and major upper airways with acoustic impedance boundary conditions applied to the terminal segments. Simulations on lung excitation through airway insonification were performed on a real lung geometry from the Visible Human Male with integration of the simplified airway tree and compared with SLDV measurements on a preserved pig lung.

4.2. Theory

4.2.1. Horsfield Model of the Human Airway Tree

The acoustics of the respiratory airway tract can be analyzed by first separating it into the supraglottal and subglottal components. Above the glottis (supraglottal), the acoustic behavior depends on the geometry of the throat, mouth and nasal passages, as well as any external apparatus used to input

sound. Additionally, the glottis, itself, will significantly alter sound propagation between supra- and sub-regions, depending on its state, from closed to partially open to fully open. Alternately, if the subject is intubated with an endotracheal tube (ETT), which serves as the source of sound excitation, the geometry of the ETT, an essentially cylindrical tube, defines the nature of sound transmission with relative simplicity bypassing the complexities and variability of the supraglottal region and glottis itself, as the tube exits subglottally, ideally into the trachea. The subglottal region consists of the trachea which then splits into the main-stem bronchi which further divide numerous times to create the complex bronchial trees. While the bronchial tree is extremely complex, geometrically it will exhibit less variability with time, relative to the supraglottal region, as voluntary actions of the subject will not significantly alter its geometry, unlike the subject's ability to alter the glottal opening, tongue position, throat and mouth geometry, etc. In the study of this dissertation the ultimate objective is to develop an acoustic model of the torso region that accounts for pulmonary acoustics. Consequently, the focus here is subglottal and a comprehensive technique for relating the acoustic pressure throughout the bronchial tree to the acoustic pressure just below the glottis will be developed. A glottal and supraglottal model, or ETT acoustic model, in addition to a model of the acoustic excitation source, would then be needed to relate the acoustic pressure just below the glottis to the input excitation to the mouth or ETT. In terms of experimental validation studies, the subglottal acoustic pressure can be either directly or approximately measured by either placing a miniature microphone at the end of the ETT in the case of intubation or by placing a dynamic contact sensor on the skin surface on the subglottal notch on the neck. Prior studies have described the relation between this external measurement to subglottal acoustic pressure [13].

The model of sound propagation in the subglottal region consists of two fundamental parts. First, it requires a mathematical description of the acoustic properties of individual airway segments, the description of which must be sufficiently sophisticated to include all of the phenomena of the gas and airway wall considered to be significant. Second, the dynamical description of individual airway segments must be integrated into a complex asymmetrically airway tree encompassing approximately 10^7 terminal

branches in the case of human subjects. This task is tackled by using the Horsfield self-consistent model of asymmetric dichotomy for the bronchial tree. Horsfield et al. [14, 15] proposed an approximate but comprehensive model based on detailed lung castings for both human and canine subjects. The Horsfield model of the human lung categorizes the airway tree into 35 different segment sizes, starting with $n = 35$, the trachea, and ending with $n = 1$, the terminal bronchiole, which itself terminates into two alveoli. In addition to specifying the average of each segment's length $l^{(n)}$, diameter $d^{(n)}$, wall thickness $h^{(n)}$, and area fraction of cartilage $c^{(n)}$, the Horsfield model specifies the degree of asymmetry at each airway bifurcation through a recursion index $\Delta^{(n)}$, provided in Table 4.1. An airway of order n bifurcates into two airways of order $n-1$ and $n-1-\Delta^{(n)}$. The Horsfield model is self-consistent in the sense that, for a particular airway order n , the bifurcated airway types (or daughter airways) are the same throughout the lung. A partial diagram of the lung airway tree based on this model down to $n = 23$ is shown in Figure 4.1, as adapted from Fredberg [16].

These bronchial models of Horsfield, as modified by Habib et al. [17, 18] to account for non-rigid airway walls and terminal respiratory tissues, will be used. These are based on lung airway casts and consist of acoustically one-dimensional tube-like branches that split successively into smaller and smaller components with a self-consistent asymmetrical dichotomy terminating with the alveoli. This modeling approach ought to be valid up to at least 5 kHz; at higher frequencies pressure variations across the large airway cross sections are expected, necessitating a more complex three-dimensional acoustic description.

Table 4.1 Structural parameters of the human airway model as adapted from Habib et al. [17] and scaled to match the Visible Human Male images (n , Horsefield airway order; $l^{(n)}$ and $d^{(n)}$, airway length and diameter, respectively; $h^{(n)}$, wall thickness between lumen and outer smooth muscle; $c(n)$, fractional cartilage content as a function of airway order n).

n	$l^{(n)}$ (cm)	$d^{(n)}$ (cm)	$h^{(n)}$ (cm)	$\Delta^{(n)}$	$c^{(n)}$
1	0.0600	0.1000	0.0065	0	0
	0.0600	0.1000	0.0065	0	0
3	0.0600	0.1000	0.0065	0	0
4	0.0600	0.1000	0.0065	0	0
5	0.0600	0.1000	0.0065	0	0
6	0.0737	0.1000	0.0065	0	0
7	0.0938	0.0537	0.0036	0	0
8	0.1313	0.0600	0.0040	0	0
9	0.1638	0.0663	0.0045	0	0
10	0.1375	0.0788	0.0052	0	0
11	0.3125	0.0950	0.0063	1	0
12	0.3875	0.1187	0.0075	2	0
13	0.4500	0.1375	0.0084	2	0
14	0.5250	0.1750	0.0061	3	0
15	0.6000	0.2000	0.0106	3	0
16	0.6462	0.2250	0.0114	3	0
17	0.7875	0.2500	0.0120	3	0.0329
18	0.8000	0.2725	0.0125	3	0.0374
19	0.9625	0.3000	0.0131	3	0.0429
20	1.0125	0.3125	0.0134	3	0.0453
21	1.0250	0.3375	0.0139	3	0.0501
22	1.1500	0.3500	0.0140	3	0.0525
23	1.0000	0.3625	0.0143	3	0.0548
24	1.2375	0.3875	0.0147	3	0.0594
25	1.1875	0.4375	0.0158	3	0.0681
26	1.0750	0.4375	0.0158	3	0.0681
27	1.3500	0.5375	0.0186	3	0.0844
28	1.2125	0.6750	0.0256	3	0.1037
29	1.4125	0.7375	0.0305	3	0.1114
30	1.4125	0.7375	0.0305	3	0.2000
31	1.3125	0.9125	0.0511	3	0.2500
32	1.3750	1.0000	0.0660	3	0.3000
33	2.7500	1.3750	0.1685	3	0.5000
34	6.2500	1.5000	0.2169	2	0.5000
35	12.5000	2.0000	0.4655	1	0.6700

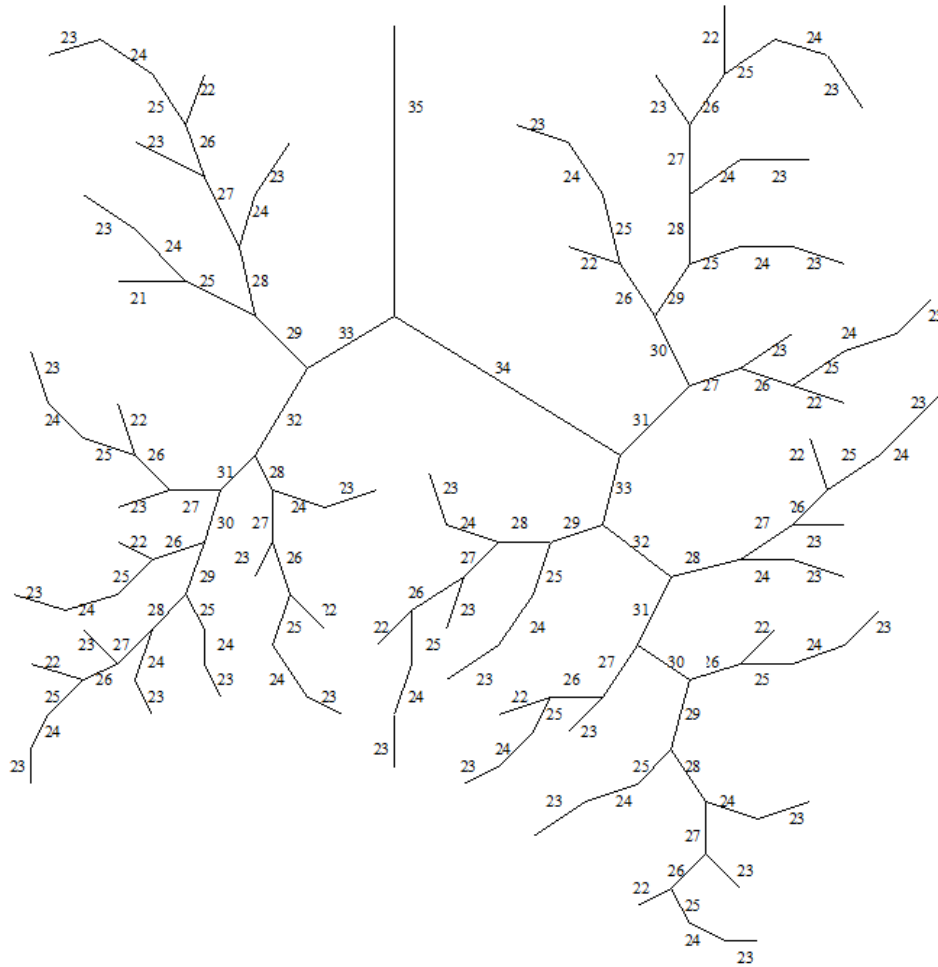


Figure 4.1 Diagram of partial airway model of Horsfield (from 35th to 23rd order), adapted from Fredberg et al. [16].

4.2.2. Mathematical and Diagrammatic Description of the Subglottal Model

It is of interest in the present study to be able to calculate the acoustic impedance (ratio of acoustic pressure to acoustic particle velocity as a function of frequency) at the input to the trachea as a function of the airway geometry and any changes it experiences. Additionally, as will be shown later, as a means of estimating sound transmission to the chest surface, it is also of interest to be able to explicitly calculate the acoustic pressure distribution within the airways, at least through the first several bifurcations, say down to $n = 21$. The self-consistent nature of the Horsfield model renders the first of these tasks, the input impedance calculation, relatively simple in spite of approximately 6 million airways

present in the model. The first step is to calculate the input acoustic impedance at a terminal bronchiole, $n = 1$. Then, “march up” the recursion ladder from $n = 2$, then 3 and so on until calculating the input impedance for $n = 35$, the trachea. Referring to Figure 4.2, for the n^{th} order airway segment of length $l^{(n)}$, the input acoustic impedance $Z_{in}^{(n)}[\omega]$ (taken at the end closer to the trachea) is given by

$$Z_{in}^{(n)}[\omega] = \frac{Z_T^n[\omega] + Z_0^n[\omega] \tanh[\gamma_0^{(n)}[\omega] l^{(n)}]}{1 + (Z_T^n[\omega]/Z_0^n[\omega]) \tanh[\gamma_0^{(n)}[\omega] l^{(n)}]}, \quad n = 1, \dots, 35. \quad (4.1)$$

The terms $Z_0^{(n)}[\omega]$ and $\gamma_0^{(n)}[\omega]$ are the characteristic impedance and propagation coefficient of the n^{th} airway segment, respectively, and are computed using the following equations [17-19].

$$Z_0^{(n)}[\omega] = \sqrt{Z^{(n)}[\omega]/Y^{(n)}[\omega]}, \quad (4.2)$$

$$\gamma_0^{(n)}[\omega] = \sqrt{Z^{(n)}[\omega]Y^{(n)}[\omega]}, \quad (4.3)$$

$$Z^{(n)}[\omega] = \frac{j\omega\rho_g}{A^{(n)}(1 - F_v^{(n)}[\omega])}, \quad (4.4)$$

$$Y^{(n)}[\omega] = \frac{j\omega A^{(n)}}{\rho_g c_g^2} (1 + 0.402 F_t^{(n)}[\omega]) + \frac{1}{Z_w^{(n)}[\omega] l^{(n)}}, \quad (4.5)$$

$$F_v^{(n)}[\omega] = \frac{2}{a^{(n)} \sqrt{-j\omega\rho_g/\eta_g}} \frac{J_1[a^{(n)} \sqrt{-j\omega\rho_g/\eta_g}]}{J_0[a^{(n)} \sqrt{-j\omega\rho_g/\eta_g}]}, \quad (4.6)$$

$$F_t^{(n)}[\omega] = \frac{2}{a^{(n)} \sqrt{-j\omega C_g/\kappa_g}} \frac{J_1[a^{(n)} \sqrt{-j\omega C_g/\kappa_g}]}{J_0[a^{(n)} \sqrt{-j\omega C_g/\kappa_g}]}, \quad (4.7)$$

$$Z_w^{(n)}[\omega]^{-1} = \frac{c^{(n)}}{Z_{w,c}^{(n)}[\omega]} + \frac{1 - c^{(n)}}{Z_{w,s}^{(n)}[\omega]}. \quad (4.8)$$

Here, $Z_w^{(n)}[\omega]$ is the effective volumetric wall impedance of the n^{th} order airway segment that may be composed of two distinct material types, cartilage and soft tissue, their fractional proportions denoted by

$c^{(n)}$ and $1-c^{(n)}$, respectively. Cartilage rings are present in the trachea and larger airway orders in decreasing proportion from $n = 35$ down to $n = 17$ for human subjects. For, $n = 1, \dots, 16$ only soft tissue is present ($c^{(n)} = 0$). Both the impedance of the cartilage component $Z_{w,c}^{(n)}[\omega]$ and the soft tissue component $Z_{w,s}^{(n)}[\omega]$ can be computed by invoking a series resistance, inertance and compliance (R_w - I_w - C_w) representation of each wall compartment as

$$Z_{w,cor s}^{(n)}[\omega] = R_w^{(n)} + j \left(\omega I_w^{(n)} - 1/\omega C_w^{(n)} \right), \quad (4.9)$$

where

$$R_{w,cor s}^{(n)} = \frac{4h^{(n)}\nu_{cor s}}{\pi \left(d^{(n)}\right)^3 l^{(n)}}, \quad (4.10)$$

$$I_{w,cor s}^{(n)} = \frac{h^{(n)}\rho_{cor s}}{\pi d^{(n)}l^{(n)}}, \quad (4.11)$$

$$C_{w,cor s}^{(n)} = \frac{\pi \left(d^{(n)}\right)^3 l^{(n)}}{4h^{(n)}E_{cor s}}. \quad (4.12)$$

Here, $\nu_{cor s}$ denotes the viscosity, $\rho_{cor s}$ denotes the density and $E_{cor s}$ denotes Young's modulus of the cartilage or soft tissue, respectively. Nominal material property values are: $\nu_c = 18,000$ Pa·s, $\nu_s = 160$ Pa·s, $\rho_c = 1,140$ kg/m³, $\rho_s = 1,060$ kg/m³, $E_c = 4.4 \times 10^6$ Pa, and $E_s = 3.92 \times 10^4$ Pa.

The term $Z_T^{(n)}[\omega]$ denotes the acoustic impedance at the far end of each segment, which is given by

$$Z_T^{(n)}[\omega] = \begin{cases} \frac{N_T}{j\omega C_g + 1/\left[R_t + j\left(\omega I_t - 1/[\omega C_t]\right)\right]} & n = 1 \\ \frac{1}{1/Z_T^{(n-1)}[\omega] + 1/Z_T^{(n-1-\Delta[n])}[\omega]} & n = 2, \dots, 35 \end{cases}. \quad (4.13)$$

Here, N_T denotes the total number of terminal ($n=1$) bronchiole segments, which are effectively in parallel with respect to the termination into the soft tissue of the parenchymae. For the Horsfield human model, this can be calculated using the following recursion formula, taking $N_T^{(1)} = 1$ and $N_T = N_T^{(35)}$,

$$N_T^{(n)} = N_T^{(n-1)} + N_T^{(n-1-\Delta[n])}. \quad (4.14)$$

The result is $N_T \approx 2.35$ million in this case. The term C_g denotes the alveolar gas compression compliance based on the Dubois [20] six-element terminal airway model. Also based on the Dubois model, R_t , I_t and C_t denote the terminal tissue resistance, inertia and compliance. (The lumped airway wall inertance and resistance of the Dubois six-element model are replaced here by the more comprehensive airway tree model.)

Calculating acoustic pressure values (e.g. complex amplitudes as a function of frequency referenced to the input acoustic pressure at the trachea) throughout the airway tree is not as simple as the impedance calculation. For pressure calculations, the starting point is at the trachea, $n = 35$, respectively, and then proceeds down the tree. Pressure values are not self-consistent in that all branch segments of the same order n' where $n' < 35$ will not have the same pressure values as they all are different lengths from the trachea. I.e., there is a different sequence of orders between them and the trachea, which results in different pressure values. So, calculating pressure values for every segment in the human airway tree would require more than 2.35 million separate calculations. However, for purposes discussed later, it is feasible to calculate pressures, say through the first six or so bifurcations from the trachea, which would amount to the following number of branch segments:

$$\sum_{m=0}^6 2^m. \quad (4.15)$$

While the acoustic pressure levels will not be consistent among airways of the same order “ n ”, the ratio of acoustic pressure $P_{rat}^{(n)}[\omega]$ at the far end $P_T^{(n)}[\omega]$ to that at the near end $P_{in}^{(n)}[\omega]$ (closer to the trachea) is consistent among airway segments of a particular order “ n ” and is given by:

$$P_{rat}^{(n)}[\omega] = \frac{P_T^{(n)}[\omega]}{P_{in}^{(n)}[\omega]} = Z_T^{(n)}[\omega] \left\{ \frac{\cosh[\gamma_0^{(n)}[\omega]l^{(n)}]}{Z_{in}^{(n)}[\omega]} - \frac{\sinh[\gamma_0^{(n)}[\omega]l^{(n)}]}{Z_0^{(n)}[\omega]} \right\}. \quad (4.16)$$

Consequently, given the acoustic pressure at the input to the bronchial tree (top of trachea), the above formula is used to calculate the acoustic pressure at the base of the trachea, which is the same as the pressure at the top of the two main-stem bronchi. This process can be repeated to obtain the acoustic pressure at the top or base of any airway segment. The acoustic pressure along a particular segment can also be computed based on the pressure values at either end of the segment [16]. Taking $x = 0$ as the end of a segment nearer to the trachea and $x=l$ as the far end, gives

$$P^{(n)}[x, \omega] = \frac{Z_0^{(n)}[\omega]}{\sinh(\gamma_0^{(n)}[\omega]l)} \left(\frac{P_{in}^{(n)}[\omega]}{Z_{in}^{(n)}[\omega]} \cosh(\gamma_0^{(n)}[\omega](x-l)) - \frac{P_T^{(n)}[\omega]}{Z_T^{(n)}[\omega]} \cosh(\gamma_0^{(n)}[\omega]x) \right). \quad (4.17)$$

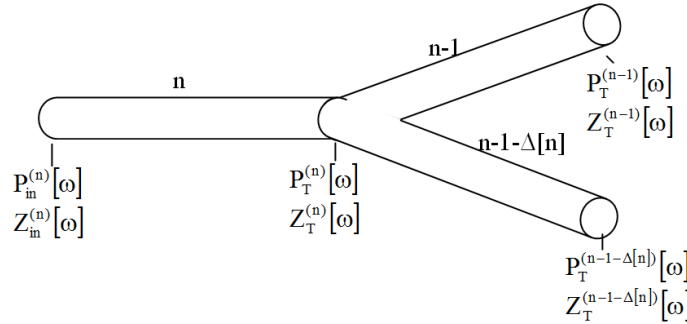


Figure 4.2 Airway acoustic model showing one bifurcation.

4.3. Studies on Tissue-Mimicking Phantom

4.3.1. Airway Acoustics in Tissue-Mimicking Phantom

First, theoretical, experimental and computational studies were conducted on a tissue-mimicking phantom for gaining a better understanding of (i) sound propagation through an airway tree, and (ii) sound coupling into the soft biological tissues. The phantom with an airway tree was built using Ecoflex 00-10 (NuSil Technology, Carpinteria, CA) and is shown in Figure 4.3. The airway tree in the phantom was created by pouring the Ecoflex 00-10 into the mold with plastic rods. The Horsefield model categorizes

this airway tree into 10 different segment sizes. The schematic diagram of the airway tree is shown in Figure 4.4. The material properties of the phantom and structural parameters of this airway tree are listed in Table 4.2 and Table 4.3. Since the same Ecoflex 00-10 was used for the phantom as used for the phantom in Section 2.3.3, the SLS viscoelastic model type and coefficients are taken from the results by approach 2 in Table 2.4. Here fractional cartilage contents $c^{(n)}$ are all zero so they are not listed in Table 4.3. The frequency dependent pressure at each terminal segment (A-H) is calculated by the equations in Section 4.2.2.

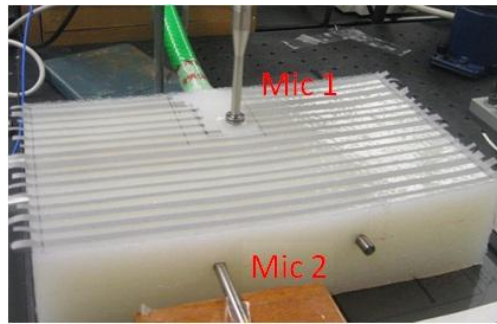


Figure 4.3 Phantom with airway tree inside.

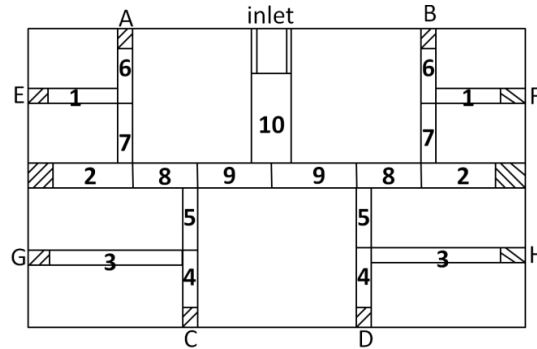


Figure 4.4 Schematic diagram of the airway tree in the phantom.

Table 4.2 Material properties of the tissue-mimicking phantom

ρ_g (kg/m ³)	1.23	c_g (m/s)	343
C_g (cal kg ⁻¹ K ⁻¹)	240	κ_g (cal m ⁻¹ s ⁻¹ K ⁻¹)	6.4×10^{-3}
η_g (Pa·s)	1.82×10^{-5}	ρ_s (kg/m ³)	965
E_s (kPa)	39.9	μ_0 (kPa)	13.3
μ_ω (kPa)	27.25	μ_1 (Pa·s)	17.77

Table 4.3 Structural parameters of the airway tree (n , Horsefield airway order; $l^{(n)}$ and $d^{(n)}$, airway length and diameter, respectively; $h^{(n)}$, wall thickness, $\Delta^{(n)}$, recursion index)

n	$l^{(n)}$ (cm)	$d^{(n)}$ (cm)	$h^{(n)}$ (cm)	$\Delta^{(n)}$
1	4.7	0.6	2.2	0
2	5.3	1.3	1.85	0
3	8.7	0.6	2.2	0
4	3.73	0.6	2.2	0
5	3.12	0.6	2.2	1
6	3.73	0.6	2.2	0
7	3.12	0.6	2.2	5
8	4	1.3	1.85	5
9	3.7	1.3	1.85	3
10	6.85	2.2	1.4	0

The airway tree acoustic was studied by measuring the pressure at each terminal segment using a 1/4 inch microphone (377A01, PCB Piezotronic, Depew, NY) (Mic 2). The reference pressure was measured by inserting a 1/2 inch microphone (4176, Brüel & Kjær Sound & Vibration, Denmark) (Mic 1) into segment 10 from the phantom top surface. Periodic chirp sound wave from 100 to 1600 Hz is introduced into the airway through a hose inserted into the inlet. Metal pins are inserted at all terminal segments by 1 cm to create the fixed boundary conditions. The measured pressure was recorded by a dynamic signal analyzer (SignalCalc ACE, Data Physics, San Jose, CA). The frequency response of the two microphone measurements can then be acquired.

The FRF of the two microphone measurements can also be calculated analytically. The first step is to calculate the input acoustic impedance at a terminal segment, $n = 1$. Then, “march up” the recursion ladder until calculating the input impedance for $n = 10$. As the FRF of pressure at two locations in the phantom is the same for all pressure values at the inlet, so assuming the pressure at the inlet to be 1 Pa, the formulae in Section 4.2.2 were used to calculate the acoustic pressure at the base of segment 10, which is the same as the pressure at the top of segment 9. This process can be repeated to obtain the acoustic pressure at the top or base of any segment. For example, referring to Figure 4.4, we have the path 10-9-5-3. The acoustic pressure at the bottom of the $n = 3$ path is:

$$P_{in}^{(3)}[\omega] = P_{in}^{(10)}[\omega] P_{rat}^{(10)}[\omega] P_{rat}^{(9)}[\omega] P_{rat}^{(5)}[\omega] P_{rat}^{(3)}[\omega], \quad (4.18)$$

$$P_T^{(3)}[\omega] = P_{in}^{(3)}[\omega] P_{rat}^{(3)}[\omega]. \quad (4.19)$$

As the microphone can be approximated as a fixed boundary condition, the impedance $Z_T^{(n)}$ at the terminal segment approaches infinity, so Equations (4.1) and (4.16) simplify to

$$Z_{in}^{(n)}[\omega] = \frac{Z_0^n[\omega]}{\tanh[\gamma_0^{(n)}[\omega] l^{(n)}]}, \quad (4.20)$$

$$P_{rat}^{(n)}[\omega] = \cosh[\gamma_0^{(n)}[\omega] l^{(n)}] - \sinh[\gamma_0^{(n)}[\omega] l^{(n)}] \tanh[\gamma_0^{(n)}[\omega] l^{(n)}]. \quad (4.21)$$

Knowing the exact location where the Mic 2 was inserted into segment 10, the reference pressure can be calculated from Equation (4.17).

The acoustics of the airway tree is also simulated in acoustic-solid interaction module in Comsol 4.3. The phantom was modeled as a viscoelastic solid. The SLS model with its estimated viscoelastic parameters of Ecoflex 00-10 in Section 2.3.3 was incorporated in the Comsol simulation. Since the phantom is symmetric, only the left half was simulated by creating a symmetry plane in Comsol. Figure 4.5 shows the 3D geometry of the left half of the phantom.

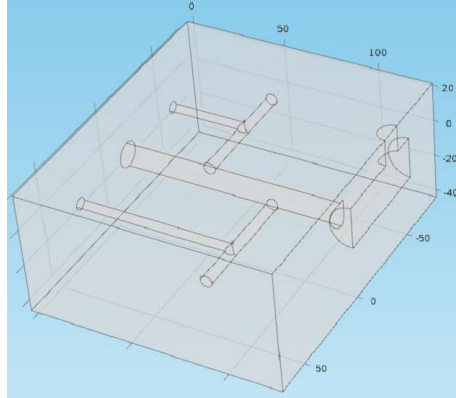


Figure 4.5 3D geometry of the left half of the phantom.

The FRF at different terminal locations are plotted in Figure 4.6. In each subplot, the red and blue curves represent experimental results measured at left and right side of the phantom. The analytical calculation and Comsol simulation match the experiment reasonably well in the upper half of the

frequency range shown, but show some discrepancy in the vicinity of the lower resonant frequency.

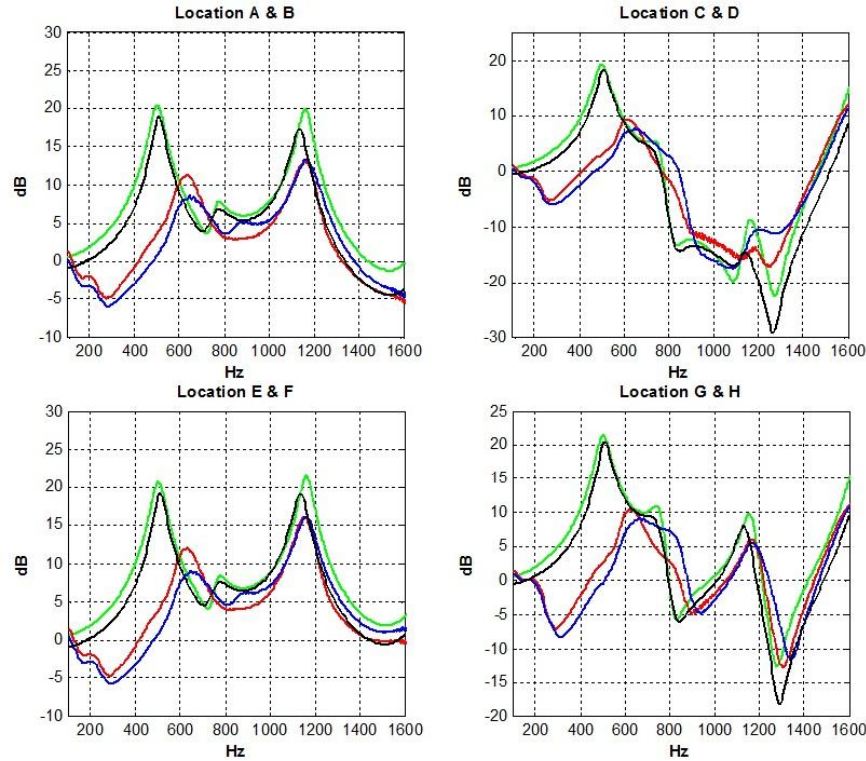


Figure 4.6 FRF of Mic 2/Mic 1 (Pa/Pa), fixed boundary condition at all terminal segments, for locations refer to Figure 4.4. Key: — simulation, — theoretical prediction, — and — measurement.

4.3.2. Sound Coupling into Tissue-Mimicking Phantom

Sound coupling into the soft biological tissues was studied by using the same phantom mentioned above. As the walls of the airway trees are elastic, they will have radial motion when sound propagates through the airway tree, the sound wave motion is coupled into the solid part of the phantom in this way. As shown in Figure 4.7, bands of retro-reflective tapes were adhered on the phantom top surface to enhance laser reflectivity. A total number of 1126 scanning points were defined on the retro-reflective tapes. The same B&K microphone was used to measure the reference pressure. Metal pins are inserted at all terminal segments by 1 cm to create the fixed boundary conditions. The input sound wave has a broad band frequency between 100 Hz and 1600 Hz. The surface velocity on top of the phantom was measured by SLDV and the FRF of the phantom surface velocity and reference pressure was recorded. The wave propagation in this phantom was also simulated in acoustic-solid interaction module in Comsol 4.3. The

interpolated FRF amplitudes at three different frequencies from experimental measurements are plotted together with simulation results in Figures 4.8-4.10. In each figure, the left half is from the simulation and the right half is from experiment. (The phantom model is symmetric about the center.) The color bar is in dB. In the experiment, a small area on the phantom top surface was shaded by the fixture of the microphone and thus can't be scanned by the SLDV. It is shown that the FRF amplitude distribution between simulation and experiment generally matches well at 1000 Hz and 1500 Hz. At 500 Hz, the FRF amplitude at the peripheral area of the phantom from the experiment is smaller than that from the simulation, this corresponds to the observation from Figure 4.6 that the measured FRF is smaller than that from the simulation below 600 Hz. As the measured pressures at the terminal segments are smaller than predicted, it is expected that the peripheral area of the phantom top surface will have less motion, thus resulting in a smaller FRF.

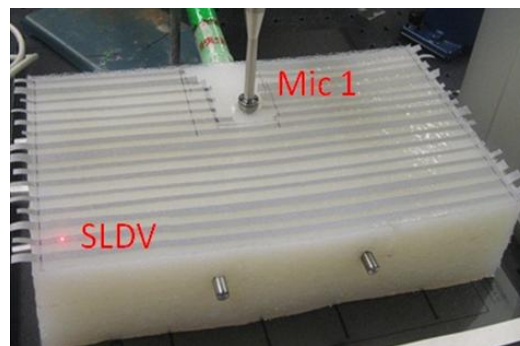


Figure 4.7 Experimental setup of sound coupling into phantom measurement.

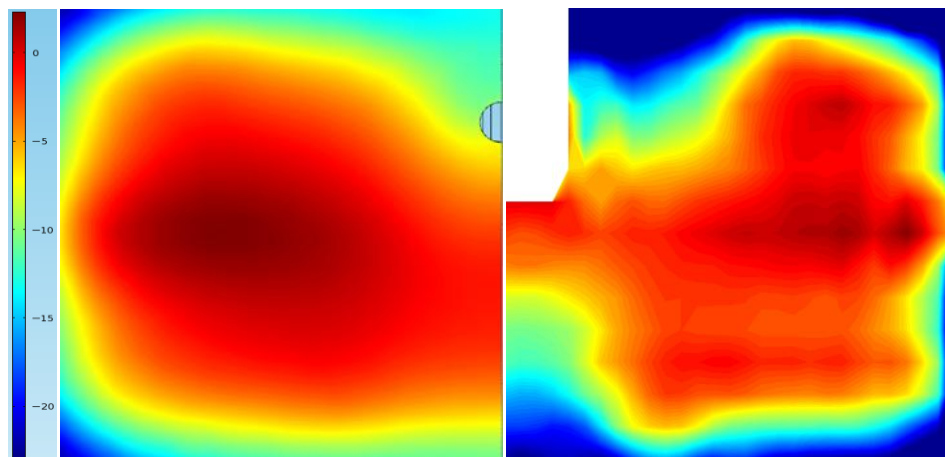


Figure 4.8 FRF of phantom surface velocity at 500 Hz. (Left: Simulation, Right: Experiment)

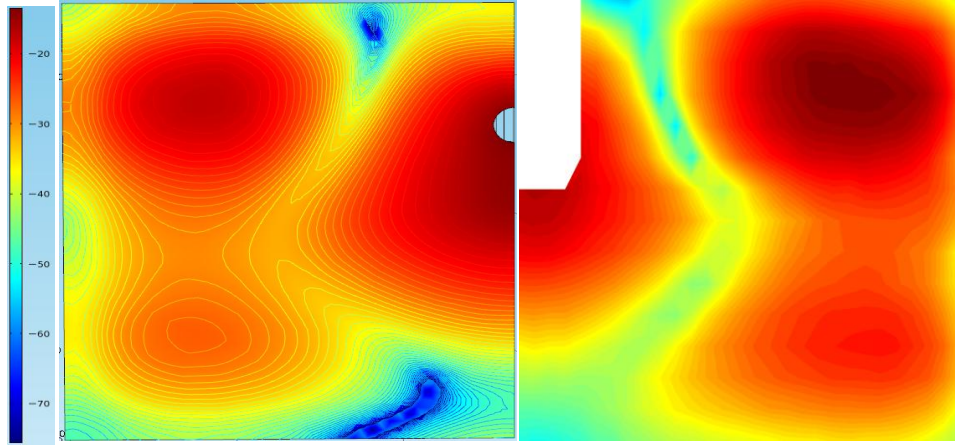


Figure 4.9 FRF of phantom surface velocity at 1000 Hz. (Left: Simulation, Right: Experiment)

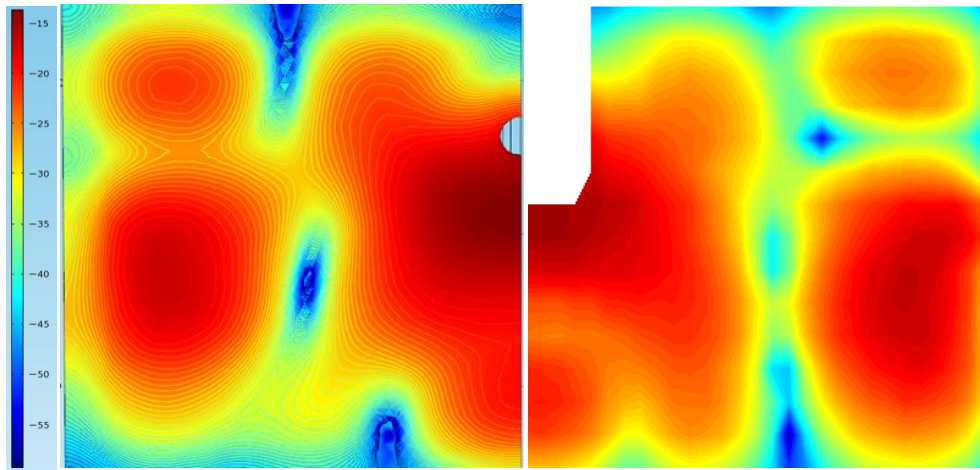


Figure 4.10 FRF of phantom surface velocity at 1500 Hz. (Left: Simulation, Right: Experiment)

4.4. Studies on Ex Vivo Pig Lung and In Vivo Human Lung

4.4.1. Pig Lung Excitation through Airway Insonification

SLDV measurements (Polytec PSV-400) of an excised preserved pig lung (ENasco) subject to airway insonification were taken and the experimental set up is shown in Figure 4.11. The preserved lung was hung under a frame and fully inflated. Broad band periodic chirp with spectral content from 50 to 1000 Hz was generated by a 3.5 inch speaker (PDWR30W, PylePro, Brooklyn, NY) and sent into the lung via the frame. P-RETRO-250 glass beads (45 – 63 μm dia., Polytec, Irvine, CA) were spread on and adhered to the lung surface to enhance the laser reflectivity. The whole lung was scanned by the SLDV

except the areas where the left and right lobe touch each other and some peripheral points where the laser can barely scan. Four scans were made at different angles and then combined to cover the entire lung geometry. The lung was preserved using propylene glycol and its mechanical properties were stable and, though not the same, appeared to be close to that of live or freshly excised lung. This enables repeated experiments on the lung that take time. Also, an endotracheal tube was usually inserted into the fresh lung to maintain a patent airway. The ET tube changes the sound pressure level sending into the trachea and the surface motion amplitude of the trachea wall. It also introduces some difficulty into the computer simulation of airway insonification. Due to these factors the preserved lung was used instead of the fresh lung. The SLDV measurements will be compared with computer simulations of lung excitation caused by airway insonification and they will be presented in Section 4.4.3.

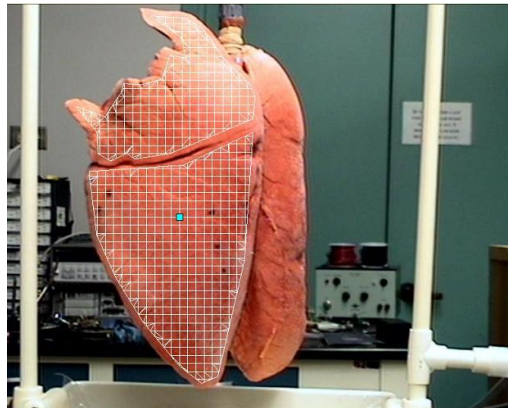


Figure 4.11 Experiment setup of SLDV measurement of lung surface motion.

4.4.2. Geometry Construction of Human Lung and Airway Tree

With the success of studies on sound transmission in the tissue-mimicking phantom, the similar simulation approach can be applied to the human lung. First of all, it requires an anatomically precise 3D geometrical model of the human lung. The lung geometry without airways was converted from the CT images of the Visible Human Project (VHP) of the National Library of Medicine and is shown in Figure 4.12.

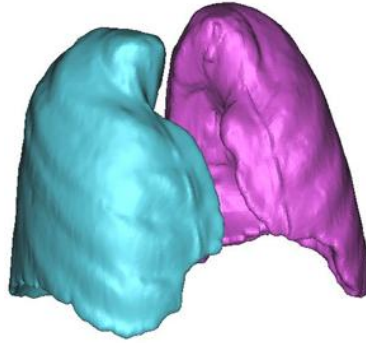


Figure 4.12 Human lung geometry from the Visible Human Project.

Constructing anatomically precise airway geometry is far more complex than the lung contour. There are millions of smaller airway segments that are beyond MRI or CT image registration or reconstruction. Also simulation on sound transmission in the lung with millions of airway segments will be too computational costly. So an airway model with enough segments to best approximate the complete respiratory system while on the other hand adaptive to the computational/time costs is sought. Even though recent advancements in CT and MRI make small airway segmentation easier, the manual segmentation is prohibitively time consuming while the automatic segmentation has limited use due to its non open-source segmentation software.

Computer generated airways offer a new approach to this problem. Kitaoka et al. [21] proposed a programmatic way of generating airway trees in three dimensions, by growing trees strictly according to hard coded mathematical laws and conditions. The benefit of this approach was the development of an elaborate and complex airway tree with the number of segments specified by the user in an asymmetrical fashion; however, the method was only capable of producing a single model. The only variation between each tree was the number of generated airway segments. In addition, all terminal segments must have the same flow to make computation time as minimal as possible. As a base model for the simulation, the computer generated airways serve as a quick way to evaluate sound transmission in the lung due to its flexibility in segments generation. Figure 4.13 (a) and (b) show the computer generated airways with around 55000 segments.

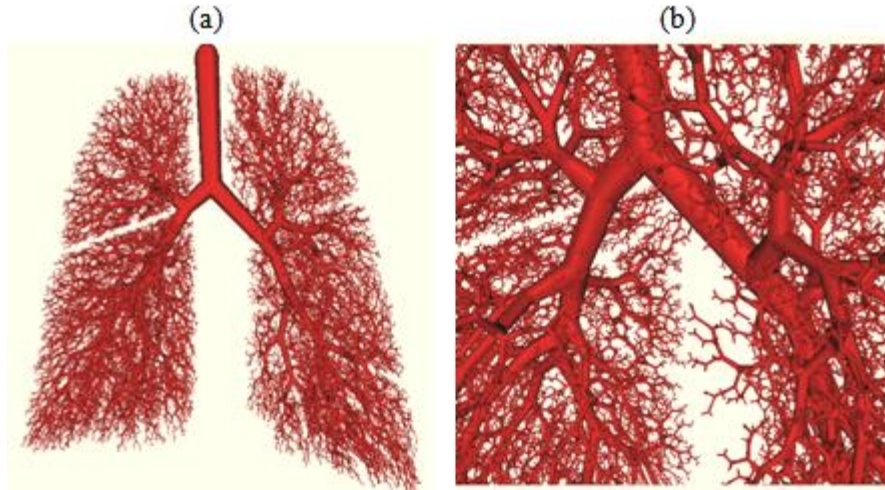


Figure 4.13 (a) Computer generated airway tree with around 55000 segments (b) Details of the same airway tree.

4.4.3. Simulations on Human Lung Excitation through Airway Insonification

Even though the entire airway tree from the trachea to the respiratory bronchioles can be generated if the number of bifurcations is large enough, such a detailed airway tree with millions of segments integrated into the lung will be computationally prohibitive. Thus it is important to generate a simplified airway tree to approximate the acoustic properties of the human airway tree accurately and at the same time to reduce the computation time. The impedance $Z_T^{(n)}[\omega]$ of the terminal bronchiole segments and the upper stream segments can be calculated from Equation (4.13); so, for the simplified airway $Z_T^{(n)}[\omega]$ of the terminal segments can be the impedance boundary condition of the airways integrated into the lung. As the air transmits in the airway tree, each airway segment expands and contracts in its radial direction and these motions are coupled into the lung parenchyma. Once the airway tree is simplified, it is hard to compensate the motions of the truncated airway segments even though these truncated small airway segments only contribute a very small portion of the total airway tree motion. So, after a comprehensive consideration of the number of airway tree segments and Comsol 4.3 computation

time, an airway tree with a total of 255 segments was used for simulation and it is shown in Figure 4.14. It is a simplified airway tree including the trachea and the total 7 bifurcation segments below the trachea.

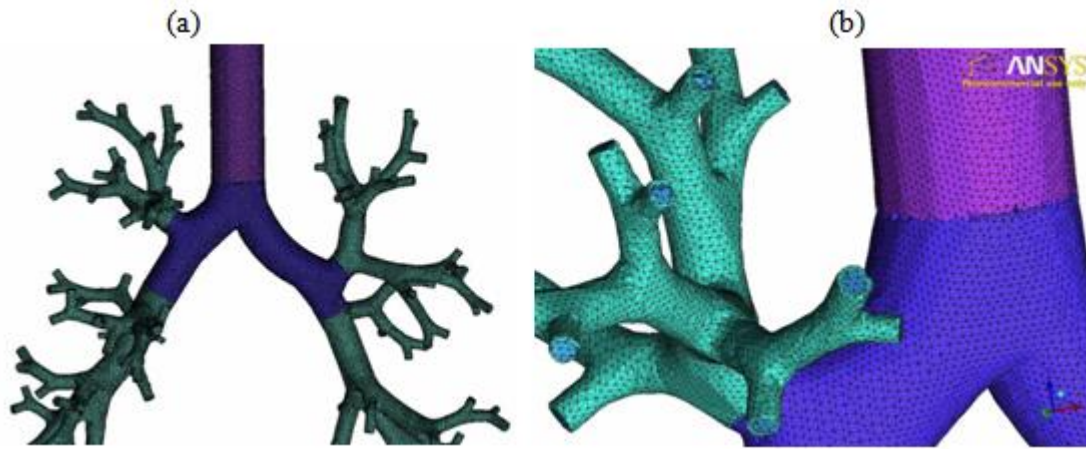


Figure 4.14 (a) Geometry of the simplified airway tree with a total of 255 segments (b) Detail of the terminal airway segment.

Then the simplified airway tree was integrated into the lung and it is shown in Figure 4.15(a). Figure 4.15(b) shows the mesh of the lung and airways. The simulation was performed in acoustic-solid interaction module in Comsol 4.3. Then material properties and boundary conditions were specified to each region. The lung density is taken to be 250kg/m^3 . The parameter input for the lung region was its complex compression wave speed c_p and shear wave speed c_s and they were calculated by $c = \omega/k$. k is the complex wave number of the compression or shear wave. As the experimental data of human lung compression and shear wave speed was not available, it is assumed that the mechanical properties of the fresh pig lung were very close to those of the human lung and they were used when the human lung data were not available. For the compression wave, the wave number was calculated by the Biot theory presented in Chapter 3 and for the shear wave, the wave number was calculated by the lung shear viscoelasticity detailed in Chapter 2. Due to the large difference in cartilage ratio at different airway segments, the simplified airway tree was divided into three regions, the trachea, the left and right principal bronchi and the small airways, as shown by three different colors in Figure 4.14(a). Their complex Young's modulus E and Poisson's ratio ν were specified respectively and they were expressed as

$$E_i = c^i E_c + (1 - c^i) E_s, \quad i=1,2,3. \quad (4.22)$$

where E_c and E_s are the complex Young's modulus of the cartilage and tissue part of the airway and they were taken from Suki et al. [22]. c^i is the cartilage ratio of the i th region defined above. c^1 and c^2 were taken to be 0.67 and 0.5 from Table 4.1 and c^3 was taken to be 0.1 as a representation for all the small airways.

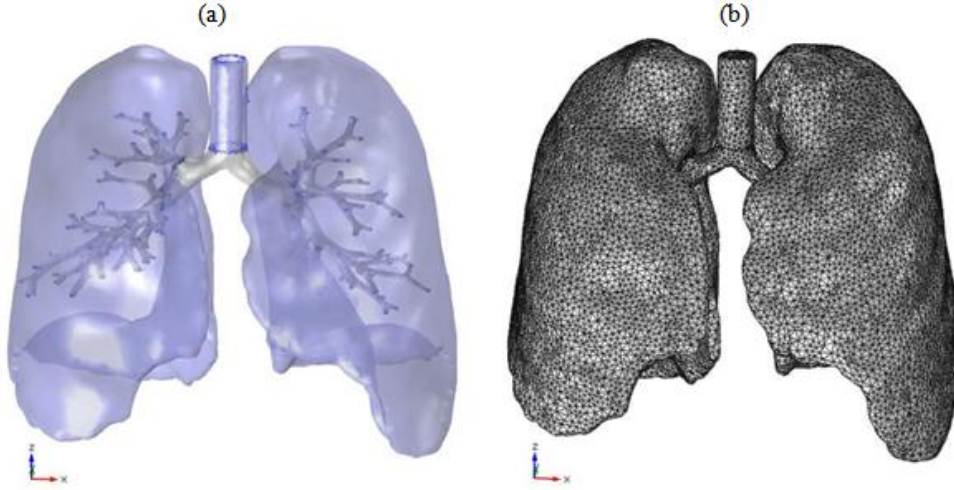


Figure 4.15 (a) Simplified airway tree integrated into the lung (b) Mesh of the lung and airways.

Since the structural parameters of the computer generated airways are not exactly the same as the ones of the Horsfield model, some approximations were taken for the impedance $Z_T^{(n)}[\omega]$ at the terminal segments of the simplified airway tree. As there is no order number of each segment for the computer generated airways, it is impossible to calculate $Z_T^{(n)}[\omega]$ for each segment as there is no hierarchical order information of its downstream segments. But numerical calculations show that for a segment with specific diameter, variations in its downstream segments hierarchical order and small variations on its own diameter only have small effects on its $Z_T^{(n)}[\omega]$; so, $Z_T^{(n)}[\omega]$ was determined based on the diameter of each terminal segment. The diameters of the 128 terminal segments are very close to each other as shown in Figure 4.14(b); their mean diameter was calculated to be 0.258 cm and, based on $d^{(n)}$ in Table 4.1, $Z_T^{(17)}[\omega]$ was assigned as the impedance of these 128 terminal segments. The input pressure was 1 Pa at

the inlet of the trachea. The simulation was performed at 300 Hz and 500 Hz. The corresponding material properties and boundary conditions were listed in Table 4.4 and 4.5.

Table 4.4 Material properties and boundary conditions for simulation at 300 Hz

c_p (m/s)	$25.79+6.04j$	$E_1(\times 10^5\text{Pa})$	$2.82 + 9.32j$	ν_1	0.49998
c_s (m/s)	$5.89+1.05j$	$E_2(\times 10^5\text{Pa})$	$2.25 + 7.44j$	ν_2	0.49998
$Z_T^{(17)}$ (Pa·s)	$16.23+30.22j$	$E_3(\times 10^5\text{Pa})$	$0.92 + 3.03j$	ν_3	0.49999

Table 4.5 Material properties and boundary conditions for simulation at 500 Hz

c_p (m/s)	$28.34+8.05j$	$E_1(\times 10^5\text{Pa})$	$2.82 + 15.52j$	ν_1	0.49998
c_s (m/s)	$6.29+1.21j$	$E_2(\times 10^5\text{Pa})$	$2.25 + 12.44j$	ν_2	0.49998
$Z_T^{(17)}$ (Pa·s)	$18.76+51.10j$	$E_3(\times 10^5\text{Pa})$	$0.92 + 5.04j$	ν_3	0.49999

The human lung surface velocity amplitude from the simulation was compared with the SLDV measurements on the preserved pig lung. It is most appropriate to compare the experimental results with simulations on the same preserved lung geometry; but, there are a few factors which make this direct comparison extremely difficult here. First, the airways can only be generated within a specific volume defined by the code designer; the user can't input an arbitrary volume. So, currently it is very difficult to integrate the generated human airway tree into a pig lung. Second, the structural parameters of the preserved pig lung airway tree are unknown without the imaging technique such as high resolution CT. And finally, there are deviations between the preserved lung geometry constructed by SLDV geometry scan and its real geometry due to the areas where it is difficult to scan. But the comparison between the simulation and experiments on preserved lung was not aimed at fully validating the computer model; it is just to validate the simulation approach. Also the similarity in mechanical properties between the human lung and the pig lung makes such comparison possible.

The surface velocity amplitude of the human lung from simulation and the pig lung from SLDV measurements are shown in Figure 4.16-4.19. The color bar is in dB scale. The velocity amplitudes from the simulation were shifted to have the same dB scale as the experiment. In Figure 4.16, both plots are shown in the color range -140 dB to -70 dB. The data range from the simulation is beyond this, it is from -146.65 dB to -48.25 dB. Definitely this is partially due to the different shape of the two lungs. The high end value -48.25 dB is mainly due to the high velocity amplitude in the area where the left and right principal bronchus enter the lung (the broken area in the middle of the lung shown in Figure 4.18(a)) and this area was not measured by the SLDV due to the lung position. The low end value -146.65 dB is mainly due to the low velocity amplitude in the peripheral area of the lung which was not scanned as shown in Figure 4.11. Figure 4.17(a) shows the velocity amplitude of the areas only in the data range -140 dB to -70 dB from the simulation. Comparisons between Figure 4.16(a) and Figure 4.18(a) show that both the experiment and simulation show similar patterns of velocity amplitude distributions. The velocity amplitudes are largest in the central areas of the lung and then gradually decay in the peripheral areas. While from the simulation the area in the bottom of the lung has lower velocity amplitudes than from the measurement, this is mainly due to the non-uniform distribution of airways in the human lung model. The distal ends of the simplified airway tree do not reach far enough toward the bottom of the lung, thus the motion there gets smaller. The comparisons at 500 Hz also lead to similar observations.

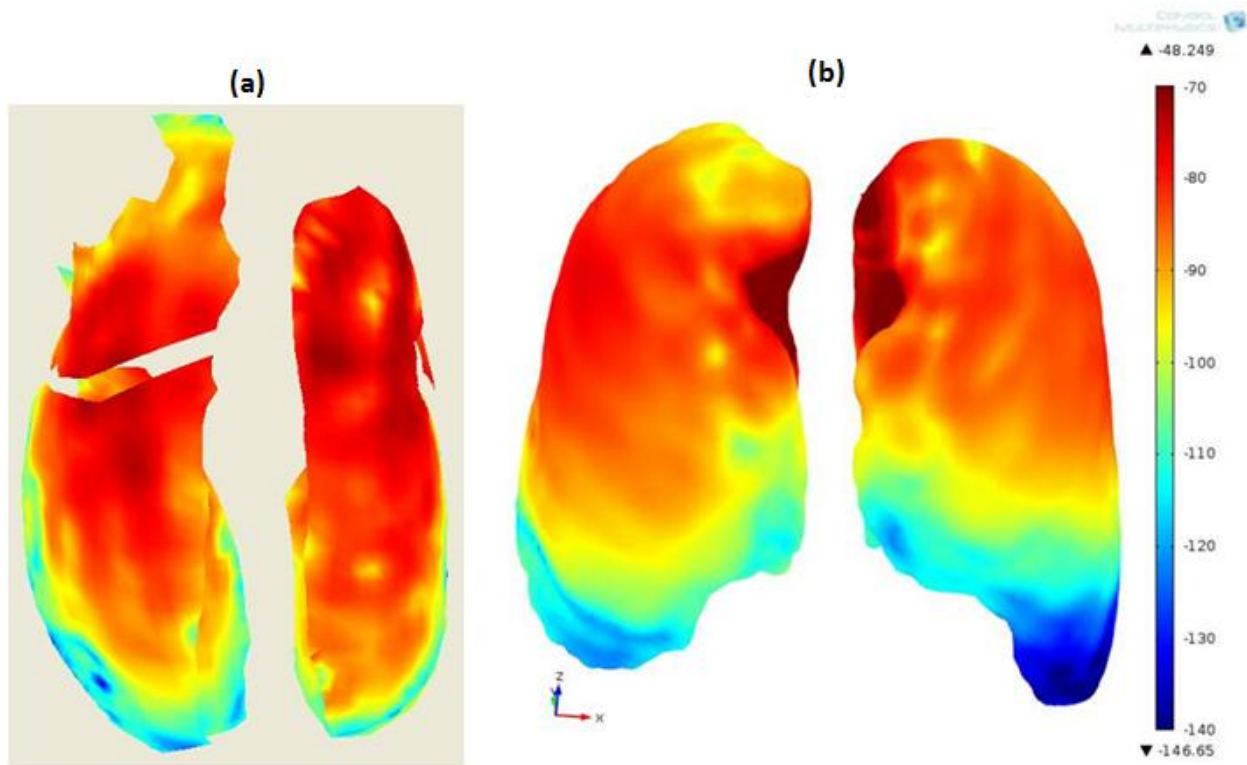


Figure 4.16 Lung surface velocity at 300 Hz (a) Experiment (b) Simulation.

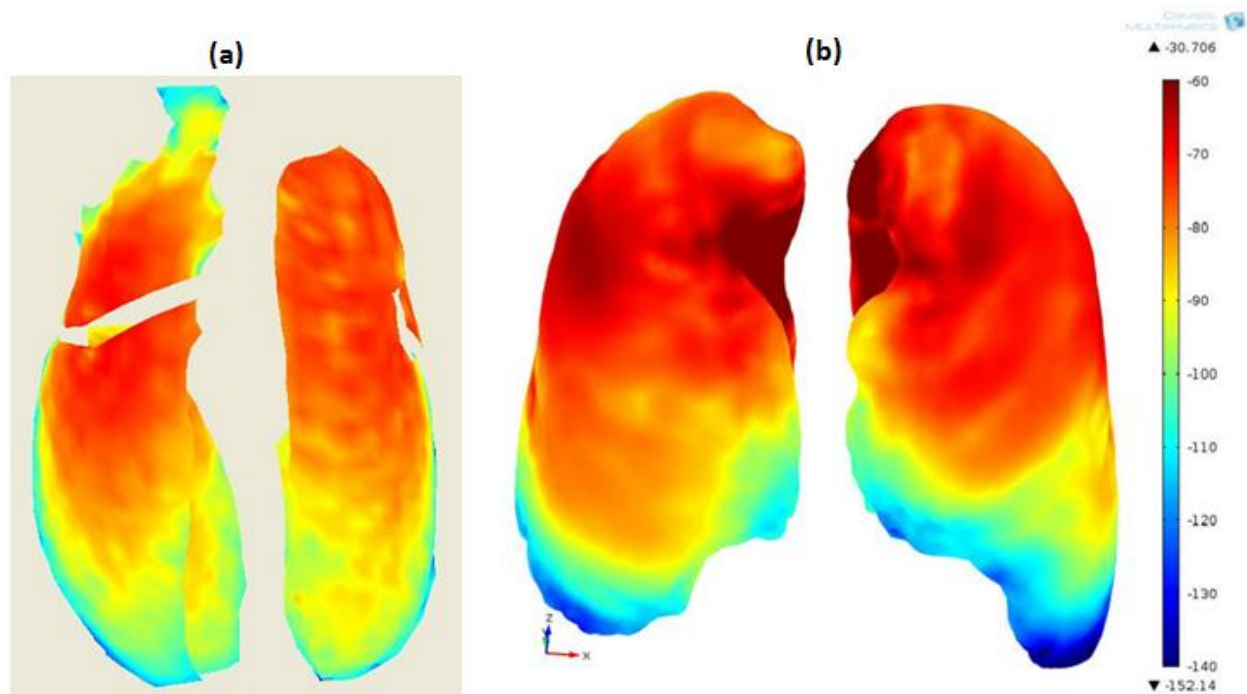


Figure 4.17 Lung surface velocity at 500 Hz (a) Experiment (b) Simulation.

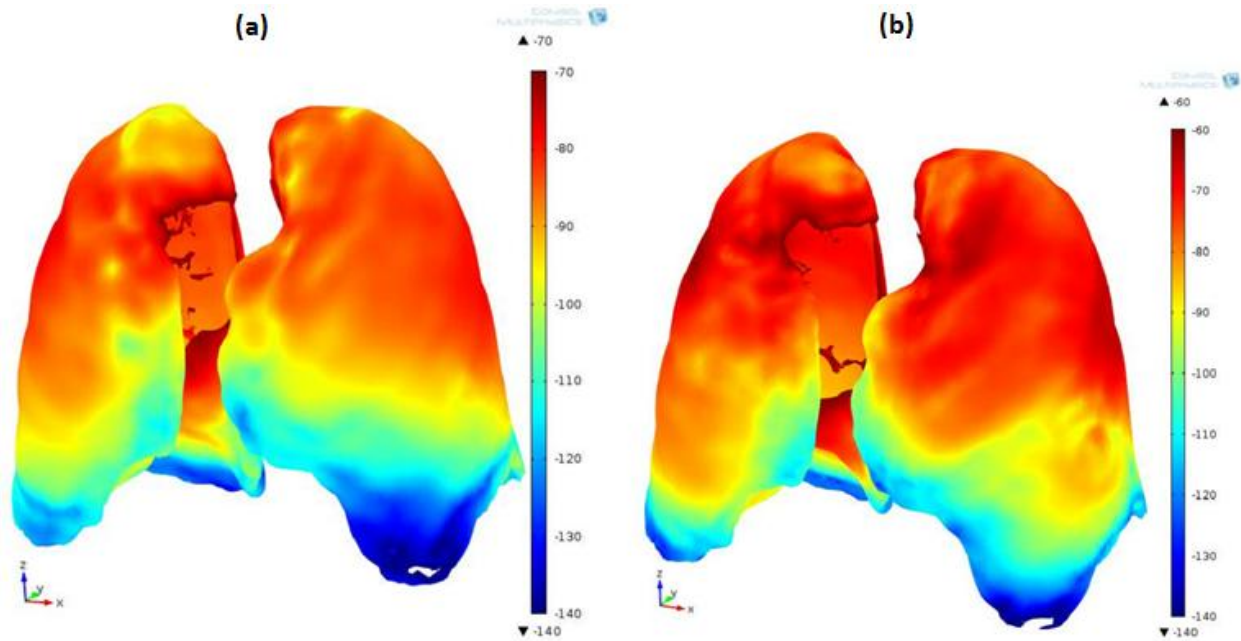


Figure 4.18 Lung surface velocity from simulation (only areas within data range plotted) (a) 300 Hz (b) 500 Hz.

4.5. Discussion

Sound transmission in the airways and coupling into lung parenchyma is studied in this chapter. The study was first carried out on a tissue-mimicking phantom with airway tree inside. Sound was transmitted into the phantom through its airway inlet and couples into the phantom. The phantom airway acoustics generally agreed well between analytical calculations, numerical simulations and experiments under the frequency range of interest. Good agreement was also achieved on phantom surface motion between the numerical simulations and experiments. Simulations on human lung excitation through airway insonification were carried out on a real lung geometry from the Visible Human Male with integration of the simplified computer generated airways into the lung. The acoustic impedance boundary conditions of the terminal airways segments were applied by using the structural parameters of the Horsfield model. The simulations were compared with SLDV measurements on a preserved pig lung and similar trends in lung surface velocity distribution were observed. This approach provides a feasible way of simplifying the airway tree and greatly reduces the computation time.

4.6. References

1. Mansy HA, Balk R, Royston TJ, Sandler RH, 2002, Pneumothorax detection using pulmonary acoustic transmission measurements, *Med. Biol. Eng. Comput.* 40, pp. 520 – 525.
2. Mansy HA, Balk R, Royston TJ, Sandler RH, 2002, Pneumothorax detection using computerized analysis of breath sounds, *Med. Biol. Eng. Comput.* 40, pp. 526 – 532.
3. Pasterkamp H, Patel S, Wodicka GR, 1997, Asymmetry of respiratory sounds and thoracic transmission, *Med. Biol. Eng. Comput.* 35, pp. 103–106.
4. Kompis M, Pasterkamp H, Wodicka GR, 2001, Acoustic imaging of the human chest, *Chest*, 120, pp. 1309-1321.
5. Ionescu CM, Muntean I, Tenreiro-Machado JA, De Keyser R, Abrudean M, 2010, A theoretical study on modeling the respiratory tract with ladder networks by means of intrinsic fractal geometry, *IEEE Trans. Biomed. Eng.* 57(2), pp. 246-253.
6. Paciej R, Vyshedskiy A, Shane J, Murphy R, 2003, Transpulmonary speed of sound input into the supraclavicular space, *J. Appl. Physiol.* 94, pp. 604-611.
7. Wodicka GR, Stevens KN, Golub HL, Cravalho EG, Shannon DC, 1989, A model of acoustic transmission in the respiratory system, *IEEE Trans. Biomed. Eng.* 36, pp. 925 – 34.
8. Vovk IV, Grinchenko VT, Oleinik VN, 1995, Modeling the acoustic properties of the chest and measuring breath sounds, *Acous. Phys.* 41, pp. 667 – 76.
9. Royston TJ, Zhang X, Mansy HA, Sandler RH, 2002, Modeling sound transmission through the pulmonary system and chest with application to diagnosis of a collapsed lung, *J. Acous. Soc. Amer.* 111, pp. 1931 – 1946.
10. Ozer MB, Acikgoz S, Royston TJ, Mansy HA, Sandler RH, 2007, Boundary element model for simulating sound propagation and source localization within the lungs, *J. Acous. Soc. Amer.* 122 (1), pp. 657 – 671.

11. Acikgoz S, Ozer MB, Royston TJ, Mansy HA, Sandler RH, 2008, Experimental and computational models for simulating sound propagation within the lungs, *ASME J. Vib. & Acous.* 130 (2), pp. 021010-1 – 021010-10.
12. Wochner MS, Ilinskii YA, Hamilton MF, Zabolotskaya EA, 2009, Model for fatigue and failure of human lung tissue subjected to low-frequency underwater sound, *Underwater Acoustics Measurements: Technologies and Results 2009 conference*, Nafplion, Greece.
13. Wodicka GR, Stevens KN, Golub HL, Shannon DC, 1990, Spectral characteristics of sound transmission in the human respiratory system, *IEEE Trans. Biomed. Eng.* 37, pp. 1130-1134.
14. Horsfield K, Cumming G, 1968, Morphology of the bronchial tree in man, *J. Appl. Physiol.* 24, pp. 373-83.
15. Horsfield K, Kemp W, Phillips S, 1982, An asymmetrical model of the airway of the dog lung, *J. Appl. Physiol.* 52, pp. 21-26.
16. Fredberg JJ, Moore JA, 1978, Distributed response of complex branching duct networks, *J. Acoust. Soc. Am.* 63, pp. 954 – 61.
17. Habib RH, Chalker RB, Suki B, Jackson AC, 1994, Airway geometry and wall mechanical properties estimated from subglottal input impedance in humans, *J. Appl. Physiol.* 77, pp. 441-51.
18. Habib RH, Suki B, Bates JH, Jackson AC, 1994, Serial distribution of airway mechanical properties in dogs: effects of histamine, *J. Appl. Physiol.* 77, pp. 554 –566.
19. Benade AH, 1968, On the propagation of sound waves in a cylindrical conduit, *J. Acous. Soc. Am.* 44, pp. 616-623.
20. Dubois AB, Brody AW, Lewis DH, Burgess Jr BF, 1956, Oscillation mechanics of lungs and chest in man, *J. Appl. Physiol.* 8, pp. 587-594.
21. Kitaoka H, Takaki R, Suki B, 1999, A three-dimensional model of the human airway tree, *J. Appl. Physiol.* 87, pp. 2207-2217.

CHAPTER 5

Acoustic Measurements of Sound Transmission in Human Subjects

5.1. Introduction

Auscultation has been used qualitatively by physicians for hundreds of years to aid in the monitoring and diagnosis of a wide range of medical conditions, including those involving the pulmonary system (breath sounds), the cardiovascular system (e.g. heart sounds and bruits caused by partially occluded arteries and arteriovenous grafts) and the gastrointestinal system. There may be unique and diagnostically important information in audible frequency sound since characteristic times for many physiological processes and anatomical structural resonances are in that range [1, 2]. This approach offers several potential advantages including noninvasiveness, safety, availability, prompt results, and low cost, making it suitable for in-office check-ups, out-patient home monitoring, and field operations following natural or man-made catastrophes. Simple stethoscopic use is skill-dependent, provides qualitative rather than quantitative information at only a single location, and suffers from inherent limitations of human ability to discern certain acoustic differences. In recent years, many researchers have applied more quantitative measurement and analysis techniques to increase the diagnostic utility of this approach, utilizing electronic sensors and applying computational signal processing and statistical analyses to the measured signals to discern trends or biases correlated with pathologies [3-8].

Alterations in the structure and function of the pulmonary system that occur in disease or injury often give rise to measurable changes in lung sound production and transmission. Lung sounds are known to contain spatial information that can be accessed using simultaneous acoustic measurements at multiple locations. It has been shown that lung consolidation, pneumothorax, and airway obstruction, to name a few conditions, alter the production and/or transmission of sound with spectrally and regionally differing effects that, if properly quantified, might provide additional information about the severity and location of the trauma or pathology [3-6]. Indeed, simultaneous, multi-sensor auscultation methods have been developed to “map” sounds on the thoracic surface by several groups [7-11], and in some cases to then

attempt to triangulate upon the interior location(s) of the sound sources by assuming that the sounds propagate away from the source with spherical symmetry in speed and attenuation [6].

In patients with emphysema [12] and in dogs with pneumothorax [3, 4], a decrease of transmitted amplitude at low frequencies was observed, which is qualitatively consistent with the common auscultatory finding of decreased lung sound intensity. In contrast, cardiogenic pulmonary edema was found to increase the amplitude of sound transmitted to the chest wall in dogs in a linear fashion over a wide frequency bandwidth relative to postmortem wet to dry weight ratios [13], a finding consistent with that of bronchial breathing heard over consolidated lung.

Lung functional and structural imaging based on an array of contact acoustic sensors placed on the back has been researched for the past decade or so [6, 8, 14] and has recently gained more prominence through the burgeoning success of such systems as Deep Breeze™, a commercial product utilizing up to 40 vacuum mounted contact acoustic sensors on the patient's back or integrated into their bed to provide a real time assessment of lung sound strength, spectral content and regional variation, all of which may be beneficial to diagnosis [15-17].

In this chapter of the dissertation, sound transmission in the human chest is measured on normal human subjects by the SLDV and piezodisk sensors embedded on a chair back. The measurements by these two methods are compared and the advantage and disadvantage of each method are discussed.

5.2. Sound Transmission Measured by SLDV

To measure the response of the thorax to sonic perturbations of known quality, a number of investigations have focused on the transmission of sound from introduction at the mouth to detection on the chest surface. Previously the most commonly used sensors to detect chest surface motion are accelerometers and microphones. As these sensors are all in contact with the chest surface, they affect the chest surface motion to some extent. The spatial resolution of the chest surface motion is limited due to the size of each sensor. But with the help of scanning laser Doppler vibrometer (SLDV), both the contact dynamics problem and the spatial resolution problem can be solved.

Figure 5.1 is a schematic diagram of a human subject (with no known pulmonary pathologies) laying on their stomach. The prostrate posture is preferred over the sitting posture as it reduces the motion of the human body to the maximum extent and thus enhances the signal-to-noise ratio (SNR). Bands of retroreflective tape are adhered to the back of the human subject to enhance reflection of the SLDV laser for improved SNR. Studies have confirmed that the thin retroreflective tape has a negligible effect on the measured response – hence, there are no contact dynamics to consider. The human subject has a hose in their mouth through which sound is being transmitted into the torso. Another single-point LDV (PDV-100, Polytec, Irvine, CA) measures vibration at the suprasternal notch, serving as a reference for the SLDV measurement at discrete points on the back. The SLDV laser point (red spot in Figure 5.2) raster scans through an array of designated measurement points. The input sound is the periodic chirp signal from 0-1000 Hz. It is amplified by a power amplifier (P 3500S, Yamaha, Buena Park, CA) and sent to a 3.5 inch speaker (PDWR30W, PylePro, Brooklyn, NY). The scanning area is from the fifth rib to the diaphragm with a total of 210 scanning points on each side of the back. It only takes about 6 minutes for the SLDV to scan the total 420 points. Figure 5.2 shows the scanning area on the left back of the human subject.

The array data is then processed to determine the frequency response function (FRF) at each measurement point. To ensure that the FRF has a high SNR in the frequency range of interest, the coherence between the signal measured by the SLDV and the reference signal is calculated as a measure of the SNR with respect to the reference. The coherence is defined as

$$C_{xy} = \frac{|G_{xy}|^2}{G_{xx}G_{yy}} . \quad (5.1)$$

where G_{xx} and G_{yy} are the autospectral density of the reference signal and the signal measured by the SLDV. G_{xy} is the cross-spectral density between the two signals.

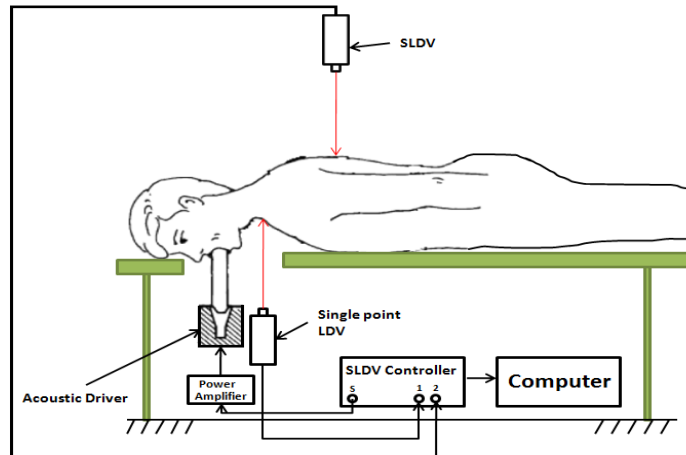


Figure 5.1 Schematic diagram of SLDV measurements on the back of the human subject. (adapted from [18]).



Figure 5.2 Human subject with bands of retro-reflective tape adhered to the back.

The human chest is assumed to be a linear system and the coherence is smaller than one due to the noise in the measurement. On each side of the back a scanning point at the 4th row and the 11th column was selected and its FRF and coherence are plotted in Figure 5.3 and 5.4. From Figure 5.4 it is seen that the coherence is very close to one from around 50 to 500 Hz. So in Figure 5.3 the FRF outside this frequency range may deviate from the real response of the chest surface due to the poor coherence. Even though the chest surface motion amplitude at each point is different, they both decrease with respect to frequency. The frequency range of 100 to 700 Hz is divided into six equally spaced bands. A frequency

at which there are a maximum number of points with coherence ≥ 0.9 is picked up in each band and it is shown in Table 5.1. In the first four frequency bands, there are at least 75% of scanning points with good coherence at the selected frequency while this percentage is below 70% in the last two frequency bands. This also shows that the transmitted sound gets attenuated more in higher frequencies and leads to fewer points with good coherence due to the noise in the measurement.

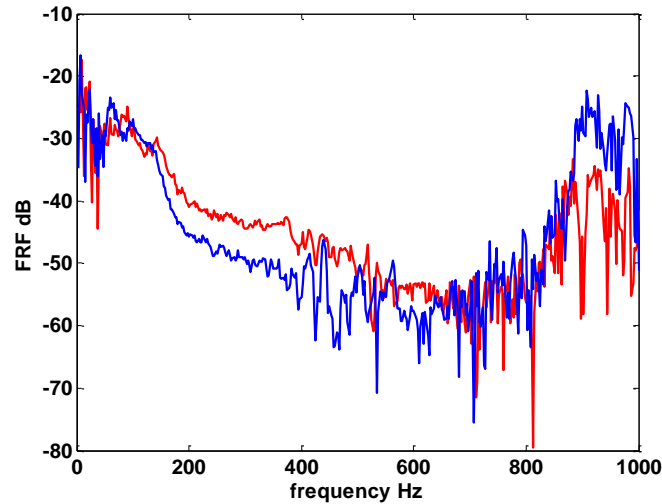


Figure 5.3 FRF of scanning points, — point on left back, — point on right back.

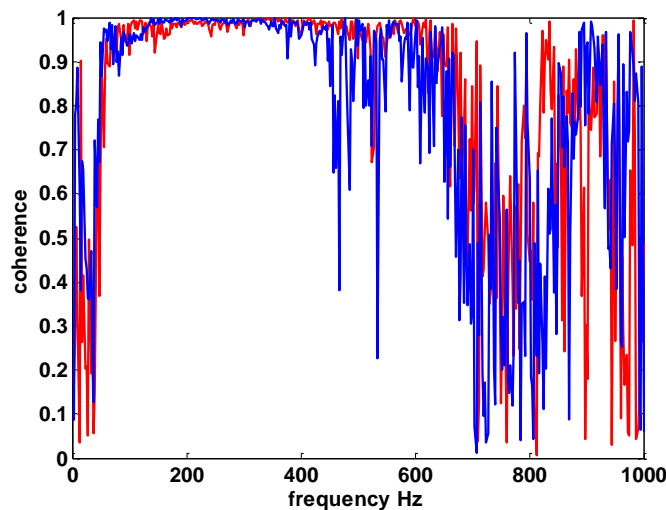


Figure 5.4 Coherence of scanning points, — point on left back, — point on right back.

Table 5.1 Frequencies in each frequency band at which there are a maximum number of points with coherence ≥ 0.9 .

Frequency Band	Frequency (Hz)	Max. # of Points
100-200	110	373
200-300	210	332
300-400	320	317
400-500	440	396
500-600	562.5	294
600-700	610	183

The FRF amplitudes at 210 Hz and 440 Hz are shown in Figure 5.5 and 5.6, respectively. Figures (a) indicate the value at the individually measured points. Figures (b) represent interpolated values. The dB color scale indicates the amplitude level at that point relative to the amplitude measured at the suprasternal notch, which served as the reference input. Measurements are only shown for which the measurement at that frequency at that point exceeded 90% coherence. The coherence of the scanning points on top of the scapular or close to the diaphragm is not as good as that of the other points due to the low amplitude of chest surface motion. Also shown in grayscale on these figures are the estimated location of the ribs (including the scapulae), diaphragm and lungs. These measurements illustrate the strong spatial dependence of sound transmission from the mouth to the chest wall and some expected attenuation over the scapulae and near the diaphragm. As the dB color scale are the same, comparisons on the FRF amplitude at these two frequencies show that for most scanning points, the FRF amplitude at 210 Hz is larger than the one at 440 Hz. This corresponds to the same observation from Figure 5.3 that the FRF amplitude decreases with frequency for most scanning points.

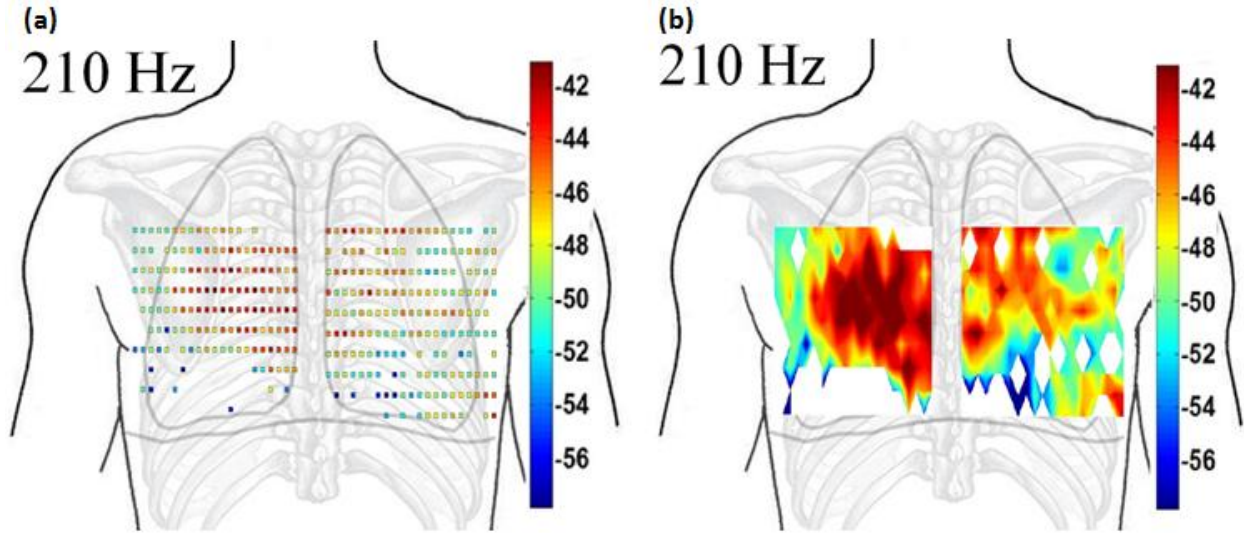


Figure 5.5 FRF at 210 Hz, colorbar in dB, (a) FRF amplitude at the individually measured points (b) interpolated FRF amplitude contour plot.

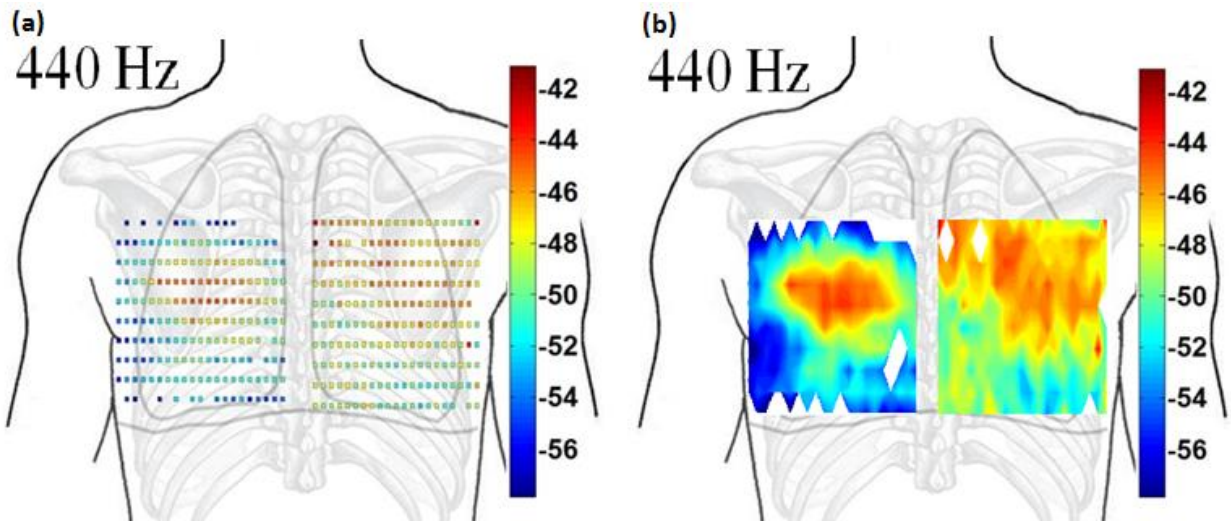


Figure 5.6 FRF at 440 Hz, colorbar in dB, (a) FRF amplitude at the individually measured points (b) interpolated FRF amplitude contour plot.

5.3. Sound Transmission Measured by Piezodisk Sensor

The SLDV serves as a gold standard in the measurement of sound transmission in human chest. But due to its extreme high cost, a more affordable measurement technique needs to be developed as an alternative of the SLDV. The microphone and accelerometers are much lower in cost compared to the

SLDV hardware and software system which is around \$300,000. But, an array of round 100 such sensors is also expensive. Instead a silicone gel coupled piezodisk sensor was used and it is developed by Dr. Thomas Royston and Dr. Todd Spohnholtz in the Acoustics and Vibration Lab where the author works. This sensor is made from a DigiKey 102-1144-ND piezoelectric buzzer. Labor aside, material costs are less than \$5 each, even in small quantities. They require no special electronics, as the electronic leads coming off of the piezoelectric element can be used directly with a high impedance data acquisition system. The top plastic of the sensor is removed and a silicone gel CF 11 (Nusil Technology, Carpinteria, CA) is poured on top of the buzzer element. The picture and the schematic diagram of the sensor are shown in Figure 5.7 (a) and (b).



Figure 5.7 (a) Silicone gel coupled piezodisk sensor (b) schematic diagram of the sensor.

Since the CF 11 silicone gel is on top of the piezodisk, it enables good contact with the skin surface. Before the sensor is used for chest surface motion measurement, it is calibrated by being put on top of a cylindrical CF 11 phantom and driven by a finite dipole source inside the phantom under the frequency range of interest from 0 to 1600 Hz. As shown in Figure 5.8, the finite dipole is inside the cylindrical CF 11 phantom which is 32 cm in diameter and 15 cm in height. The dipole is driven by a shaker (Small Vibration Exciter Type 4808, Bruel & Kjar, Denmark) that is connected to it through a stinger. The reference signal is the acceleration measured by an impedance head (288D01, PCB Piezotronics, Depew, NY) on the shaker end of the stinger. Some mass is added on the piezodisk sensor

to ensure its good contact with the phantom and mimics the force loading condition on the sensor when the back of the human subject lies on the sensors. As the dipole moves up and down in the phantom, the surface motion of the phantom is measured by the piezodisk sensor. The measured signal is a combination of the phantom surface pressure and velocity and the FRF is calculated between this signal and the reference signal.

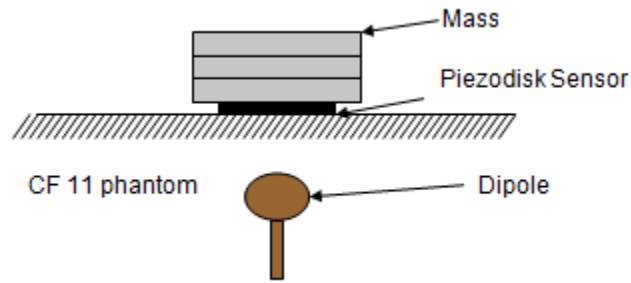


Figure 5.8 Schematic diagram of piezodisk sensor calibration setup.

A total number of 61 piezodisk sensors are calibrated and the FRF of each is not exactly the same as others. Figure 5.9 shows the FRF of 3 sensors. Unlike most of the commercially made sensors which have a pretty flat response in the measurement frequency range, the piezodisk sensor has a frequency dependent response and has a resonant frequency at round 27 Hz. The coherence in the entire frequency range is all nearly one.

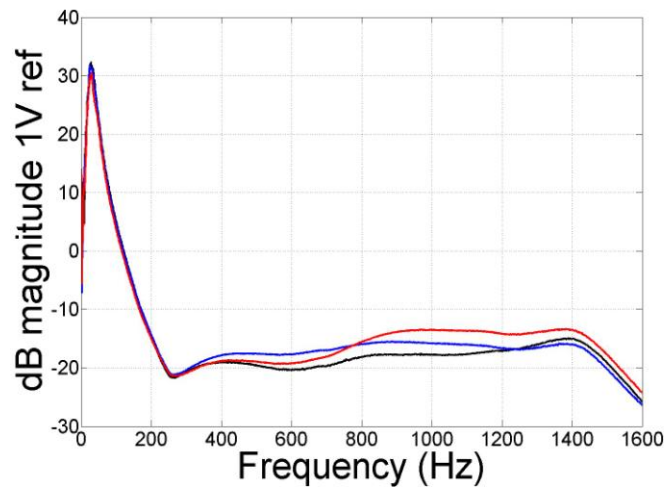


Figure 5.9 FRF of 3 piezodisk sensors from calibration.

After calibration, the piezodisk sensors are put in an array of 6×10 and imbedded on a mesh chair. The sensor chair is shown in Figure 5.10. As shown in Figure 5.11, array measurements were taken on a human subject with no known lung pathologies. The human subject sits on the chair and lay on the sensors to ensure full contact between the back and the sensors. The reference signal is measured by the same piezodisk sensor at the suprasternal notch. The input sound is the periodic chirp signal from 0-1600 Hz and it is amplified by the same amplifier. Figure 5.12 and 5.13 show the FRF and coherence of a scanning point at the 6th row, the 1st column on the left back and a scanning point at the 4th row, the 1st column on the right back. From Figure 5.13 it is seen that the coherence is very close to one from around 100 to 1300 Hz except dips at only a few frequencies. The drop of coherence at these frequencies also leads to a dramatic decrease of the FRF amplitude at the corresponding frequencies. The frequency range of good coherence is much wider than that in the SLDV measurement so this enables us to analyze the FRF at high frequencies. The FRF measured by the piezodisk sensor is more complex than that measured by the SLDV, generally it decreases with frequency only between 150 to 550 Hz.



Figure 5.10 Piezodisk sensors imbedded on a chair.

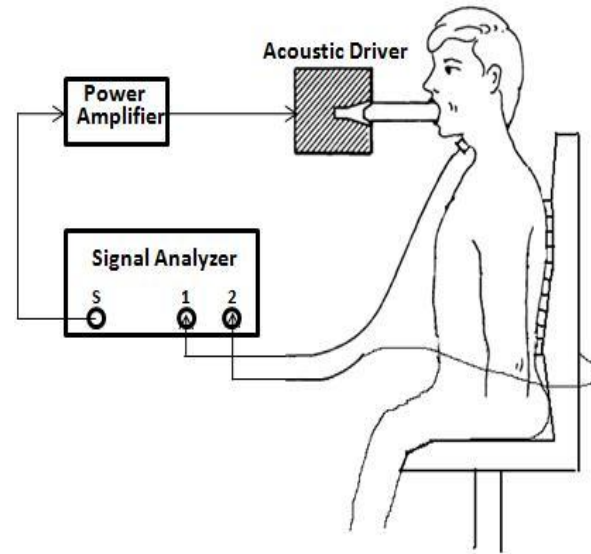


Figure 5.11 Schematic diagram Piezodisk sensor measurements (adapted from [18]).

Similar to the SLDV measurements, the entire frequency range of 100 to 1000 Hz are divided into nine equally spaced bands. A frequency at which there are maximum number of points with coherence ≥ 0.9 is picked up in each band and it is shown in Table 5.2. In all the frequency bands, there are at least 80% percent of scanning points with good coherence at the selected frequency.

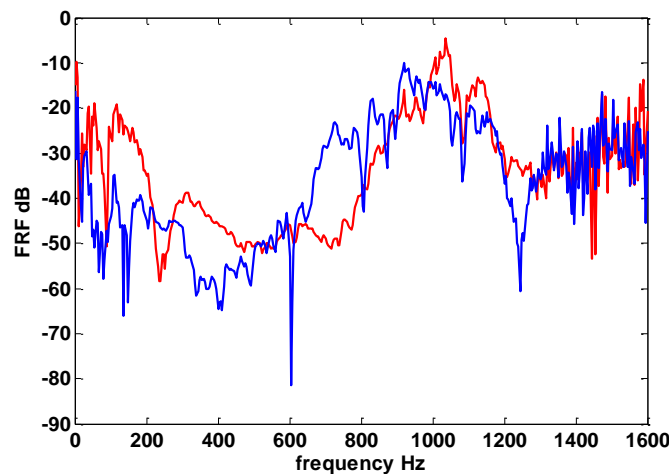


Figure 5.12 FRF of scanning points, — point on left back, — point on right back.

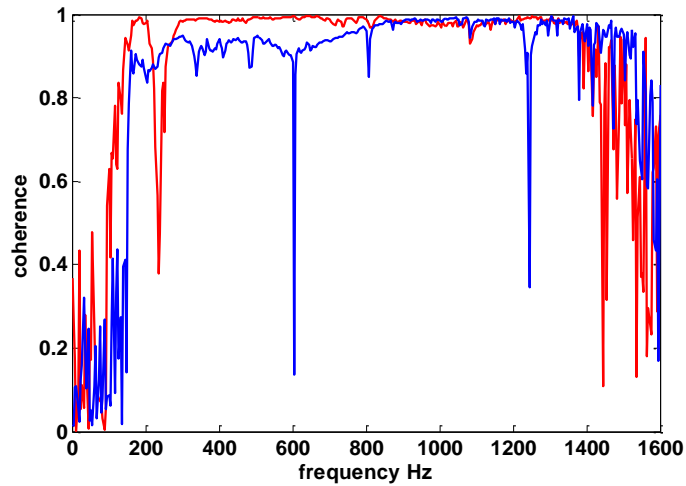


Figure 5.13 Coherence of scanning points, — point on left back, — point on right back.

Table 5.2 Frequencies in each frequency band at which there are a maximum number of points with coherence ≥ 0.9

Frequency Band	Frequency (Hz)	Max. # of Points
100-200	188	42
200-300	284	53
300-400	352	55
400-500	408	56
500-600	512	58
600-700	680	55
700-800	712	51
800-900	900	47
900-1000	912	48

The FRF amplitude at 352 Hz and 512 Hz is shown in Figure 5.14 and 5.15. Again measurements are only shown for which the measurement at that frequency at that point exceeded 90% coherence. The measurements also illustrate the strong spatial dependence of sound transmission from the mouth to the chest wall. Comparisons on the FRF amplitude at these two frequencies show that for most scanning points, the FRF amplitude at 352 Hz is larger than the one at 512 Hz. This corresponds to the same observation from Figure 5.12 that the FRF amplitude decreases with frequency between 150 and 550 Hz for most scanning points.

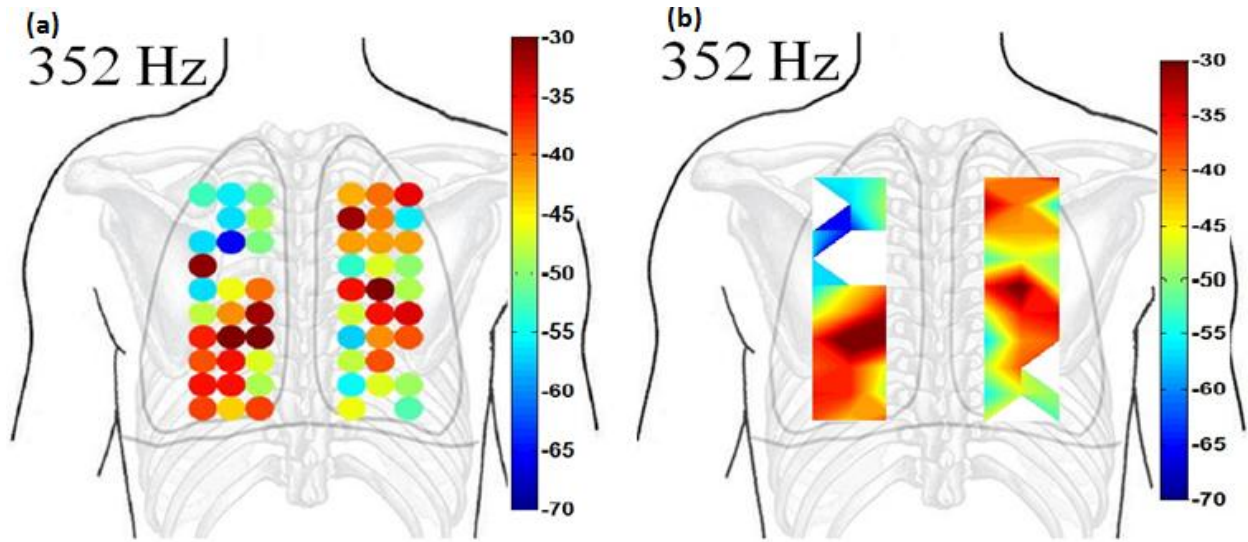


Figure 5.14 FRF at 352 Hz, colorbar in dB, (a) FRF amplitude at each sensor point (b) interpolated FRF amplitude contour plot.

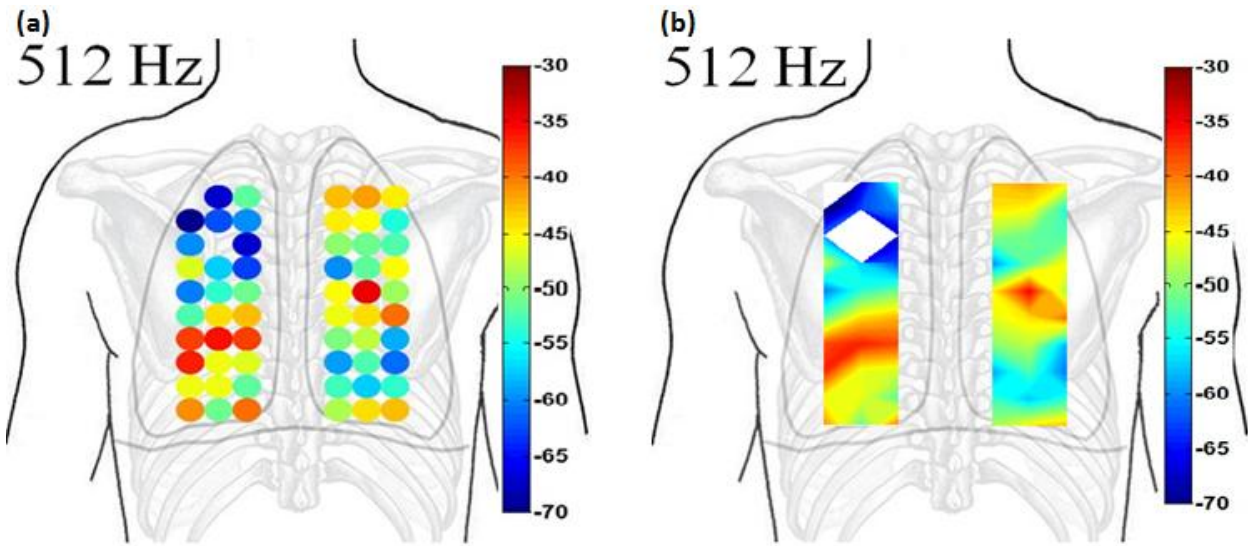


Figure 5.15 FRF at 512 Hz, colorbar in dB, (a) FRF amplitude at each sensor point (b) interpolated FRF amplitude contour plot.

5.4. Comparison of Measurements by Two Techniques

The FRF measured by the two techniques are compared under the same dB scale and Figure 5.16 and 5.17 show the comparisons at two frequencies where both plots have relatively large number of points with coherence ≥ 0.9 . The first two rows of the sensor measurements were removed in the plot to make the measurement region by two methods have the same height even though the width of the sensor

array is narrower. In most regions, the FRF amplitude measured by the SLDV is about 10-15 dB smaller than that measured by the piezodisk sensor. This difference is mostly due to the different physical quantities measured by the two methods, the LDV measures the chest surface velocity while the piezodisk sensor measures the combination of pressure and velocity on the chest surface.

Besides the limited availability of the SLDV due to its high cost, the body movement of the human subject also affects the performance of the SLDV, reducing the SNR of the measurement. These two limitations do not exist for the piezodisk sensor measurement. The human subjects lays on a chair back and his back is in firm contact with the sensors embedded on the chair back. There are two disadvantages of the piezodisk sensor. The first is its non-uniform calibration response. The calibration of each individual sensor needs to be taken in the array measurement. The second is that the exact physical quantity it measures is unknown. The contact measurement will more or less affects the chest surface motion. These limitations make the comparison with computer simulation more difficult than the SLDV measurement.

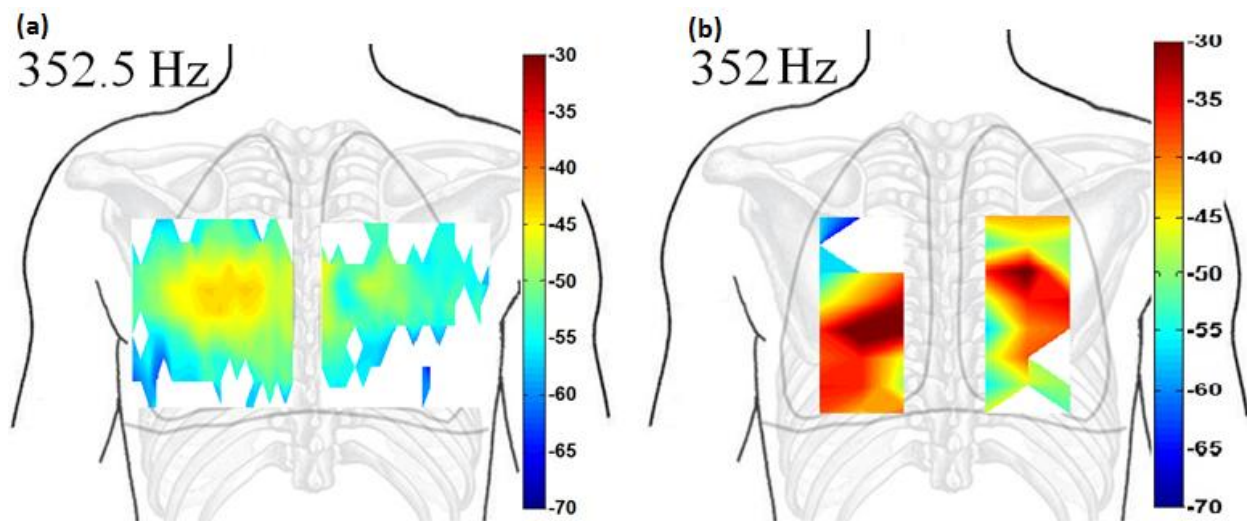


Figure 5.16 Comparison of interpolated FRF amplitude contour plot at 352.5/352 Hz, (a) SLDV measurement (b) sensor array measurement.

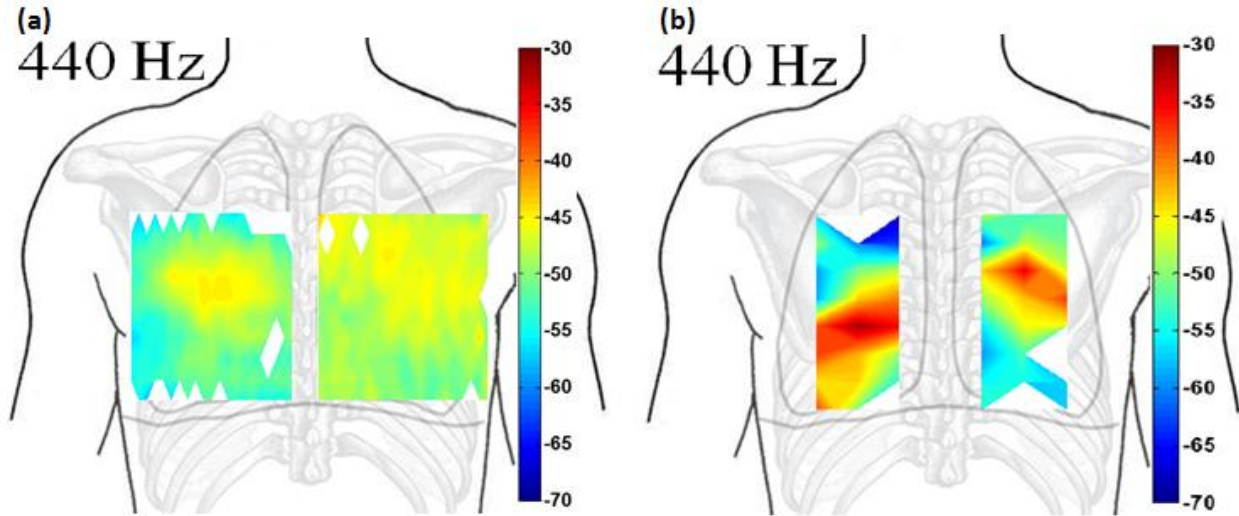


Figure 5.17 Comparison of interpolated FRF amplitude contour plot at 440Hz, (a) SLDV measurement (b) sensor array measurement.

5.5. Discussion

Pilot studies on sound transmission in the human chest are presented in this chapter. The measurements were taken on healthy human subjects by the SLDV or by the piezodisk sensors. The FRF of chest surface motion with respect to the suprasternal notch motion measured by both techniques shows strong spatial dependence on the chest surface. The FRF amplitude distributions on the back were plotted for some frequencies where they are enough measurement points with coherence ≥ 0.9 . The FRF measured by the SLDV generally decreases with frequency from 50 to 500 Hz while the FRF measured by the piezodisk sensor shows a more complex dependence with frequency from 100 to 1300 Hz. The advantage and disadvantage of each method are presented from the measurements comparison. The SLDV is the gold standard for measuring the vibroacoustic field on sound transmission in human chest while its extreme high cost limits its extensive use. Piezodisk sensor serves as an alternative due to its high sensitivity to tiny motion and low cost. Even though it has inherent limitations, the piezodisk sensor is cost-effective and may be more reliable in sound transmission measurement with ongoing improvements on its performances.

5.6. References

1. Pasterkamp H, Kraman SS, Wodicka GR, 1997, Respiratory sounds-advances beyond the stethoscope, *Am. J. Respir. Crit. Care Med.* 156(3), pp. 974-987.
2. Sarvazyan AP, 2005, Audible-frequency medical diagnostic methods: past, present and future, *J. Acous. Soc. Amer.* 117, pp. 2586.
3. Mansy HA, Balk R, Royston TJ, Sandler RH, 2002, Pneumothorax detection using pulmonary acoustic transmission measurements, *Med. Biol. Eng. Comput.* 40, pp. 520 – 525.
4. Mansy HA, Balk R, Royston TJ, Sandler RH, 2002, Pneumothorax detection using computerized analysis of breath sounds, *Med. Biol. Eng. Comput.* 40, pp. 526 – 532.
5. Pasterkamp H, Patel S, Wodicka GR, 1997, Asymmetry of respiratory sounds and thoracic transmission, *Med. Biol. Eng. Comput.* 35, pp. 103–106.
6. Kompis M, Pasterkamp H, Wodicka GR, 2001, Acoustic imaging of the human chest, *Chest*, 120, pp. 1309-1321.
7. Benedetto G, Dalmasso F, Spagnolo R, 1988, Surface distribution of crackling sounds, *IEEE Trans. Biomed. Eng.* 35, pp. 406-412.
8. Charleston-Villalobos S, Cortes-Rubiano S, Gonzalez-Camarena R, Chi-Lem G, and Aljama-Corrales T, 2004, Respiratory acoustic thoracic imaging (RATHI): assessing deterministic interpolation techniques, *Med. & Biol. Eng. & Comput.* 42, pp. 618-626.
9. Pasterkamp H, Consunji-Araneta R, Oh Y, Holbrow J, 1997, Chest surface mapping of lung sounds during methacholine challenge, *Pediatric Pulmonology*, 23, pp. 21 – 30.
10. Bergstresser T, Ofengeim D, Vyshedskiy A, Shane J, Murphy R, 2002, Sound transmission in the lung as a function of lung volume, *J. Appl. Physiol.* 93, pp. 667-674.
11. Paciej R, Vyshedskiy A, Shane J, Murphy R, 2003, Transpulmonary speed of sound input into the supraclavicular space, *J. Appl. Physiol.* 94, pp. 604-611.

12. Böhme HR, Böhme H, 1972, Variable low-frequency sound conduction of the lung in pulmonary emphysema, *Z. Gesamte Inn. Med.* 27, pp. 765–770.
13. Donnerberg RL, Druzgalski CK, Hamlin RL, Davis GL, Campbell RM, Rice DA, 1980, Sound transfer function of the congested canine lung, *Br. J. Dis. Chest*, 74, pp. 23–31.
14. Murphy R, 2007, Computerized multichannel lung sound analysis: development of acoustic instruments for diagnosis and management of medical conditions, *IEEE Eng. Med. & Bio.* 26, pp. 16-19.
15. Dellinger RP, Parrillo JE, Kushnir A, Rossi M, Kushnir I, 2008, Dynamic visualization of lung sounds with a vibration response device: a case series, *Respiration*, 75(1), pp. 60-72.
16. Maher TM, Gat M, Allen D, Devaraj A, Wells AU, Geddes DM, 2008, Reproducibility of dynamically represented acoustic lung images from healthy individuals, *Thorax*, 63(6), pp. 542-548.
17. Wang Z, Jean S, Bartter T, 2009, Lung sound analysis in the diagnosis of obstructive airway disease, *Respiration*, 77(2), pp. 134-138.
18. Wodicka GR, Stevens KN, Golub HL, Cravalho EG, Shannon DC, 1989, A model of acoustic transmission in the respiratory system, *IEEE Trans. Biomed. Eng.* 36, pp. 925 – 34.

CHAPTER 6

SUMMARY AND PERSPECTIVES

6.1. Summary

Sound transmission in the pulmonary system may provide useful information about lung structural and material property alterations caused by disease or injury. Numerous acoustic measurements have revealed the differences of breath sounds and transmitted sounds in the lung under normal and pathological conditions. Compared to the extensive cataloging of lung sound measurements, the mechanism of sound transmission in the pulmonary system and how it changes with alterations of lung structural and material properties has received less attention. A better understanding of sound transmission might improve interpretation of the lung sound measurements and help predict changes in simulations caused by various pathologies.

A long-term goal of the “**Audible Human Project (AHP)**” is to develop a computational acoustic model that would accurately simulate generation, transmission and noninvasive measurement of sound and vibration within the pulmonary system and torso caused by both internal (e.g. respiratory function) and external (e.g. palpation) sources. This dissertation, fitting within the scope of the AHP, is mainly focused on modeling sound transmission in the human lung under normal conditions. Numerical simulations and experiments were carried out to refine and validate the theoretical modeling.

Lung Tissue Viscoelasticity

The two major wave types propagating in the lung are the compression and the shear wave. The shear wave speed and attenuation at different frequencies are mainly affected by the lung tissue shear viscoelasticity. In this dissertation two experimental identification approaches of shear viscoelasticity were used. The first approach is to directly estimate the frequency-dependent surface (Rayleigh) wave speed from experimental data and then to optimize the coefficients in an assumed viscoelastic model type to minimize the difference between the measured and predicted values of wave speed. The second approach is to measure the complex-valued frequency response function (FRF) between the excitation

location and points at known radial distances from the excitation location. The FRF has embedded in it frequency-dependent information about both surface wave phase speed and attenuation that can be used to directly estimate the real and imaginary parts of the complex shear modulus. The coefficients in an assumed viscoelastic tissue model type can then be optimized to minimize the differences in the predicted and experimentally determined values of the complex shear modulus. While theoretical and experimental studies on a tissue mimicking phantom suggested that Approach #2 was more capable of distinguishing which type of viscoelastic model was most appropriate, finite element studies on the phantom and experimental studies on the excised pig lung highlighted the complications that arise due to finite boundary conditions and multiple wave types for both approaches.

Poroviscoelastic Modeling of Sound Propagation in the Lung

The compression wave in the lung is very different from that in other human internal organs. Its propagation speed is close to that of the shear wave and its high attenuation results from the interaction between the air and the lung parenchyma. The effective medium model, which leads to a frequency independent compression wave speed, has been widely used in the past three decades. There are only a few models for compression wave attenuation and not every model has direct support from experimental measurements due to the complexity in experimental estimation of the attenuation. In this dissertation a poroviscoelastic model based on Biot theory of wave propagation in porous media was used for compression wave in the lungs. This model predicts a fast compression wave speed close to the one predicted by the effective medium theory at low frequencies and an additional slow compression wave due to the out of phase motion of the air and the lung parenchyma. Both compression wave speeds vary with frequency. The fast compression wave speed and attenuation were measured on an excised pig lung under two different transpulmonary pressures. Good agreement was achieved between the experimental observation and theoretical predictions. It suggests that the Biot theory may provide a more robust and accurate model than the effective medium theory for wave propagation in the lungs over a wider frequency range.

Sound Transmission in Airways and Coupling into Lung Parenchyma

Sound propagation in the subglottal region including the trachea and the lung was studied in this dissertation. Many research studies have focused on the transmission of sound in the respiratory tract, the tracheobronchial airway tree with explorations of acoustic impedance of the tree, pressure or velocity distributions throughout the tree and response measurement at the mouth or just below the glottis or some combination of these locations with and without endotracheal intubation. Sound transmission through the surrounding biological tissues to reach the chest surface has, arguably, received less attention. Most previous studies assumed simplified geometric models and did not take the airway tree into account. It is usually very difficult to solve problems of breath sounds and transmitted sound through airway insonification by the simplified models without the airways. In this dissertation a computer generated airway tree was simplified to 255 segments and integrated into the lung geometry from the Visible Human Male for numerical simulations. Acoustic impedance boundary conditions were applied at the ends of the terminal segments to represent the unmodeled downstream airway segments. Experiments were also carried out on a preserved pig lung and similar trends of lung surface velocity distribution were observed between the experiments and simulations. This approach provides a feasible way of simplifying the airway tree and greatly reduces the computation time.

Acoustic Measurements of Sound Transmission in Human Subjects

In most previous studies, lung sounds were measured at selected sites mainly by microphones and accelerometers. A more advanced measurement with a larger spatial coverage may have more diagnostic value. In this dissertation Scanning laser Doppler vibrometry (SLDV) was used as a gold standard for transmitted sound measurements on a human subject. A lost cost piezo disk sensor array was also constructed as an alternative to the SLDV. Some similar trends in velocity distribution on the human back were observed though the physical quantities measured by the two measurement techniques are different. It suggests that piezo disk sensor will tend to be cost-effective and reliable in sound transmission measurement with ongoing improvements on its performances. With its quantitative measurement

abilities over a wide temporal and spectral range, the piezo disk sensor array may serve as a quick and more comprehensive tool than the stethoscope which highly depends on the physician's skills.

6.2. Topics for Future Research

Lung MR Elastography

Recently, the phase contrast-based technique known as magnetic resonance elastography (MRE), has been applied to the lungs in pilot studies with limited success. MRE seeks to provide a map of the viscoelastic properties within the region of interest that will affect the shear wave motion that MRE measures. Previously, MRE has been successfully applied to the study of the mechanical properties of a variety of other organs and soft tissue regions in vivo, including the breast, brain, kidney, prostate, liver and muscle. Application to the lungs has proven more challenging, given the poor signal-to-noise available in imaging due to much lower presence of hydrogen in air than in soft tissue (water), and the complex nature of vibratory wave propagation found in the lungs. MRE has the potential to noninvasively both quantify and spatially resolve the viscoelastic properties of the lung. The surface wave or mechanical indentation methods only provide regional and limited viscoelastic properties. With the help of MRE, location-specific viscoelastic properties can be estimated and be input into the computer simulation. So, MRE will have diagnostic potential to lung injury, the progression of disease and/or the response to therapy. It will also benefit computer simulations of lung sound generation and transmission.

Effects of Pathologies

The experimental studies on various lung diseases and injuries have been reported in numerous studies. For a simulation tool such as the AHP which is expected to predict alterations in sound generation and transmission in the human thorax under various abnormal conditions, it is necessary to relate changes in lung structure, mechanical properties, boundary conditions and some other factors to these various abnormal conditions. Several respiratory pathologies such as pneumothorax,

hydrothorax/pleural effusion, edema, consolidation, fibrosis and cancer could be simulated in the mechanical model following baseline measurements. Simulations may provide a better interpretation of the acoustic measurements, including MRE measurements, and aid in differentiating various pathologies.

Lung Sound Generation

It is generally accepted that breath sounds originate from turbulent air flow in larger airways and that the higher frequencies are attenuated by the biological filtering properties of the lung and chest wall. Some hypotheses and experimental studies were reported on the origin and mechanism of normal breath sounds and major categories of adventitious sounds. But there is overall lack of investigations to provide fundamental understanding for lung sound generation due to complex structural nature of the lung and the difficulty in lung sound measurement under the subglottal region. Studies in this dissertation focus on externally introduced sound into the lung, while simulations on breath sounds require a more clear understanding of lung sound generation. More precise understanding of pulmonary sounds and their clinical correlations could also lead to powerful diagnostic tools, which have particular appeal because of their noninvasive nature.

Toward a More Physiologically Accurate and Multi-Scale Lung Model

In this dissertation assumptions and simplifications were made for mechanical simulations on the lung which is governed by more complex physiological principles. A lung model with various volumes at different stages would be necessary for studies of full breathing cycles in the temporal range and the effects of different stages of a breathing cycle on sound generation and transmission. The lungs are suspended in the thoracic cavity which is normally at a slight negative pressure and the rib cage moves during inhalation and exhalation. Incorporation of these physiological conditions into mechanical simulations will bring about results which will be closer to the real physiological response of the lung. The lung is a complex organ with its components at a wide range of scales in dimensions. Simulations of micro-scale phenomena in the lung such as gas exchange in the blood air barrier are not possible on the

current macro-scale mechanical model. Current simulations are still in the scope of computational mechanics while a computational physiology approach which combines the biological/physiological and biomechanical laws toward a multi-scale structure might potentially be a better paradigm for the lung, and such paradigm could be easily applied to other human organs.

CITED LITERATURE

- 1) Achenbach JD, 1973, *Wave propagation in elastic solids*, North-Holland, Amsterdam, Netherlands.
- 2) Acikgoz S, Ozer MB, Royston TJ, Mansy HA, Sandler RH, 2008, Experimental and computational models for simulating sound propagation within the lungs, *ASME J. Vib. & Acous.* 130 (2), pp. 021010-1 – 021010-10.
- 3) Bachofen H, 1968, Lung tissue resistance and pulmonary hysteresis, *J. Appl. Physiol.* 24, pp. 296-301.
- 4) Benade AH, 1968, On the propagation of sound waves in a cylindrical conduit, *J. Acous. Soc. Am.* 44, pp. 616-623.
- 5) Benedetto G, Dalmaso F, Spagnolo R, 1988, Surface distribution of crackling sounds, *IEEE Trans. Biomed. Eng.* 35, pp. 406-412.
- 6) Berger PJ, Skuza EM, Ramsden CA, Wilkinson MH, 2005, Velocity and attenuation of sound in the isolated fetal lung as it is expanded with air, *J. Appl. Physiol.* 98(6), pp. 2235-2241.
- 7) Bergstresser T, Ofengeim D, Vyshedskiy A, Shane J, Murphy R, 2002, Sound transmission in the lung as a function of lung volume, *J. Appl. Physiol.* 93, pp. 667-674.
- 8) Biot MA, 1956, Theory of propagation of elastic waves in a fluid saturated porous solid. I Low frequency range, *J. Acous. Soc. Amer.* 28(2), pp. 168-178.
- 9) Biot MA, 1956, Theory of propagation of elastic waves in a fluid saturated porous solid. II Higher frequency range, *J. Acous. Soc. Amer.* 28(2), pp. 179-191.
- 10) Böhme HR, Böhme H, 1972, Variable low-frequency sound conduction of the lung in pulmonary emphysema, *Z. Gesamte Inn. Med.* 27, pp. 765–770.
- 11) Bonnet G, Auriault JL, 1985, Dynamics of saturated and deformable porous media: homogenization theory and determination of the solid-liquid coupling coefficients, in *Physics of finely divided matter*, Springer, Berlin.
- 12) Bourbie T, Coussy O, Zinszner B, 1987, *Acoustics of porous media*, Gulf Publishing Company, Huston, TX.

- 13) Butler JP, Nakamura M, Sasaki H, Sasaki T, Takishima T, 1986, Poissons' ratio of lung parenchyma and parenchymal interaction with bronchi, *Jpn. J. Physiol.* 36(1), pp. 91-106.
- 14) Chan RW, Titze IR, 2003, Effect of postmortem changes and freezing on the viscoelastic properties of vocal fold tissues, *Ann. Biomed. Eng.* 31, pp. 482–491.
- 15) Charleston-Villalobos S, Cortes-Rubiano S, Gonzalez-Camarena R, Chi-Lem G, Aljama-Corrales T, 2004, Respiratory acoustic thoracic imaging (RATHI): assessing deterministic interpolation techniques, *Med. & Biol. Eng. & Comput.* 42, pp. 618-626.
- 16) Chen SG, Fatemi M, Greenleaf JF, 2004, Quantifying elasticity and viscosity from measurement of shear wave speed dispersion, *J. Acoust. Soc. Am.* 115, pp. 2781–2785.
- 17) Chen Q, Mai VM, Bankier AA, Napadow VJ, Gilbert RJ, Edelman RR, 2001, Ultrafast MR grid-tagging sequence for assessment of local mechanical properties of the lungs, *Magn. Reson. Med.* 45(1), pp. 24-28.
- 18) Craiem D, Armentano R, 2007, A fractional derivative model to describe arterial viscoelasticity, *Biorheol.* 44, pp. 251–263.
- 19) Dai Z, Peng Y, Mansy HA, Royston TJ, Sandler RH, 2011, Estimation of local viscoelasticity of lungs based on surface waves, *ASME IMECE* (November 11 – 17, 2011, Denver, CO).
- 20) Deffieux G, Montaldo M, Tanter, Fink M, 2009, Shear wave spectroscopy for in vivo quantification of human soft tissues visco-elasticity, *IEEE Trans. Med. Imag.* 28, pp. 313–322.
- 21) Dellinger RP, Parrillo JE, Kushnir A, Rossi M, Kushnir I, 2008, Dynamic visualization of lung sounds with a vibration response device: a case series, *Respiration*, 75(1), pp. 60-72.
- 22) Donnerberg RL, Druzgalski CK, Hamlin RL, Davis GL, Campbell RM, Rice DA, 1980, Sound transfer function of the congested canine lung, *Br. J. Dis. Chest*, 74, pp. 23–31.
- 23) Dubois AB, Brody AW, Lewis DH, Burgess Jr BF, 1956, Oscillation mechanics of lungs and chest in man, *J. Appl. Physiol.* 8, pp. 587-594.
- 24) Duck FA, 1990, *Physical properties of tissue: a comprehensive reference book*, Academic Press, New York, NY.

- 25) Dunn F, Fry W, 1961, Ultrasonic absorption and reflection by lung tissue, *Phys. In Med. & Biol.* 5, pp. 401 – 410.
- 26) D'yachenko AI, Lyubimov GA, 1988, Propagation of sound in pulmonary parenchyma, *Izv. Akad. Nauk SSSR*, 5, pp. 3–15.
- 27) Fredberg JJ, Moore JA, 1978, Distributed response of complex branching duct networks, *J. Acoust. Soc. Am.* 63, pp. 954 – 61.
- 28) Fung YC, 1965, *Foundations of solid mechanics*, Prentice Hall, NJ.
- 29) Fung YC, 1993, *Biomechanics: mechanical properties of living tissues*, 2nd Ed., Springer-Verlag, New York.
- 30) Gennisson JL, Deffieux T, Mac é E, Montaldo G, Fink M, Tanter M, 2010, Viscoelastic and anisotropic mechanical properties of in vivo muscle tissue assessed by supersonic shear imaging, *Ultrasound in Med. & Biol.* 36, pp. 789–801.
- 31) Giannoula A, Cobbold RSC, 2008, Narrowband shear wave generation by a finite-amplitude radiation force: the fundamental component, *IEEE Trans. Ultrason. Ferroelectr. Freq. Contr.* 55, pp. 343–358.
- 32) Giannoula A, Cobbold RSC, 2009, Propagation of shear waves generated by a modulated finite amplitude radiation force in a viscoelastic medium, *IEEE Trans. Ultrason. Ferroelectr. Freq. Contr.* 56, pp. 575–588.
- 33) Goss BC, McGee KP, Ehman RC, Manduca A, Ehman RL, 2006, Magnetic resonance elastography of the lung: technical feasibility, *Magn. Reson. Med.* 56, pp. 1060–1066.
- 34) Graff KF, 1991, *Wave motion in elastic solids*, Dover Publication, New York.
- 35) Habib RH, Chalker RB, Suki B, Jackson AC, 1994, Airway geometry and wall mechanical properties estimated from subglottal input impedance in humans, *J. Appl. Physiol.* 77, pp. 441-51.
- 36) Habib RH, Suki B, Bates JH, Jackson AC, 1994, Serial distribution of airway mechanical properties in dogs: effects of histamine, *J. Appl. Physiol.* 77, pp. 554 –566.

- 37) Hajari AJ, Yablonskiy DA, Quirk JD, Sukstanskii AL, Pierce RA, Desl   G, Conradi MS, Woods JC, 2011, Imaging alveolar-duct geometry during expiration via ^3He lung morphometry, *J. Appl. Physiol.* 110, pp. 1448–1454.
- 38) Hajari AJ, Yablonskiy DA, Sukstanskii AL, Quirk JD, Conradi MS, Woods JC, 2012, Morphometric changes in the human pulmonary acinus during inflation, *J. Appl. Physiol.* 112, pp. 937-943.
- 39) Harper VP, Pasterkamp H, Kiyokawa H, Wodicka GR, 2003, Modeling and measurement of flow effects on tracheal sounds, *IEEE Trans. Biomed. Engr.* 50, pp. 1-10.
- 40) Heymans N, 2008, Dynamic measurements in long-memory materials: Fractional calculus evaluation of approach to steady state, *J. Vib. Contr.* 14, pp. 1587-1596.
- 41) Hildebrandt J, 1970, Pressure-volume data of cat lung interpreted by a plastoelastic, linear viscoelastic model, *J. Appl. Physiol.* 28, pp. 365-372.
- 42) Horsfield K, Cumming G, 1968, Morphology of the bronchial tree in man, *J. Appl. Physiol.* 24, pp. 373-83.
- 43) Horsfield K, Kemp W, Phillips S, 1982, An asymmetrical model of the airway of the dog lung, *J. Appl. Physiol.* 52, pp. 21-26.
- 44) Hosokawa A, Otani T, 1997, Ultrasonic wave propagation in bovine cancellous bone, *J. Acoust. Soc. Am.* 101(1), pp. 558-562.
- 45) Hoyt K, Kneezel T, Castaneda B, Parker KJ, 2008, Quantitative sonoelastography for the in vivo assessment of skeletal muscle viscoelasticity, *Phys. Med. Biol.* 53, pp. 4063–4080.
- 46) Iannito M, Royston TJ, MaginRL, 2011, Identifying fractional viscoelastic models based on surface wave motion, *ASME IDETC/CIE*, (Washington DC).
- 47) Ionescu CM, Muntean I, Tenreiro-Machado JA, De Keyser R, Abrudean M, 2010, A theoretical study on modeling the respiratory tract with ladder networks by means of intrinsic fractal geometry, *IEEE Trans. Biomed. Eng.* 57(2), pp. 246-253.
- 48) Jahed M, Lai-Fook SJ, 1994, Stress wave velocity measured in intact pig lungs with cross-spectral analysis, *J. Appl. Physiol.* 76, pp. 565–571.

- 48) Jahed M, Lai-Fook SJ, Bhagat PK, and Kraman SS, 1989, Propagation of stress waves in inflated sheep lungs, *J. Appl. Physiol.* 66, pp. 2675–2680.
- 49) Jenkyn TR, Ehman RL, An K, 2003, Noninvasive muscle tension measurement using the novel technique of magnetic resonance elastography (MRE), *J. Biomech. Eng.* 36(12), pp. 1917-1921.
- 50) Kemper J, Sinkus R, Lorenzen J, Nolte-Ernsting C, Stork A, Adam G, 2004, MR elastography of the prostate: initial in-vivo application, *Rofo*, 176(8), pp. 1094-1099.
- 51) Kiss MZ, Varghese T, Hall TJ, 2004, Viscoelastic characterization of in vitro canine tissue, *Phys. Med. Biol.* 49, pp. 4207–4218.
- 52) Kitaoka H, Takaki R, Suki B, 1999, A three-dimensional model of the human airway tree, *J. Appl. Physiol.* 87, pp. 2207-2217.
- 53) Klatt D, Hamhaber U, Asbach P, Braun J, Sack I, 2007, Noninvasive assessment of the rheological behavior of human organs using multifrequency MR elastography: a study of brain and liver viscoelasticity, *Phys. Med. Biol.* 52, pp. 7281–7294.
- 54) Kompis M, Pasterkamp H, Wodicka GR, 2001, Acoustic imaging of the human chest, *Chest*, 120, pp. 1309-1321.
- 55) Kraman SS, 1983, Speed of low-frequency sound through lungs of normal men, *J. Appl. Physiol.* 55, pp. 1862–1867.
- 56) Kraman SS, Austrheim O, 1983, Comparison of lung sound and transmitted sound amplitude in normal men, *Am. Rev. Respir. Dis.* 128, pp. 451–454.
- 57) Kraman SS, Bohadana AB, 1989, Transmission to the chest of sound introduced at the mouth, *J. Appl. Physiol.* 66, pp. 278–281.
- 58) Kuperman V, 2000, *Magnetic resonance imaging: physical principles and applications*, Academic Press, New York.
- 59) Lai-Fook S, Hyatt R, 2000, Effects of age on elastic moduli of human lungs, *J. Appl. Physiol.* 89, pp. 163-168.

- 60) Lakes R, Yoon HS, Katz JL, 1983, Slow compressional wave propagation in wet human and bovine cortical bone, *Science*, 220(4596), pp. 513-515.
- 61) Lakes RS, 1999, *Viscoelastic solids*, CRC Press, Boca Raton, FL.
- 62) Magin RL, 2006, *Fractional calculus in bioengineering*, Begell House, Redding, CT.
- 63) Mahagnah M, Gavriely N, 1995, Gas density does not affect pulmonary acoustic transmission in normal men, *J. Appl. Physiol.* 78, pp. 928-937.
- 64) Maher TM, Gat M, Allen D, Devaraj A, Wells AU, Geddes DM, 2008, Reproducibility of dynamically represented acoustic lung images from healthy individuals, *Thorax*, 63(6), pp. 542-548.
- 65) Mainardi F, 1997, Fractional calculus: some basic problems in continuum and statistical mechanics, in *Fractals and fractional calculus in continuum mechanics*, Carpinteri A, Mainardi F (eds), Springer Verlag, New York.
- 66) Mansy HA, Balk R, Royston TJ, Sandler RH, 2002, Pneumothorax detection using pulmonary acoustic transmission measurements, *Med. Biol. Eng. Comput.* 40, pp. 520-525.
- 67) Mansy HA, Balk R, Royston TJ, Sandler RH, 2002, Pneumothorax detection using computerized analysis of breath sounds, *Med. Biol. Eng. Comput.* 40, pp. 526 – 532.
- 68) Mariappan YK, Kolipaka A, Manduca A, Hubmayr RD, Ehman RL, Araoz P, McGee KP, 2012, Magnetic resonance elastography of the lung parenchyma in an in situ porcine model with a noninvasive mechanical driver: correlation of shear stiffness with trans-respiratory system pressures, *Magn. Reson. Med.* 67, pp. 210-217.
- 69) Marshall R, Widdicombe JG, 1960, Stress relaxation of the human lung, *Clin. Sci. Lond.* 20, pp. 19-31.
- 70) McGee KP, Hubmayr RD, Ehman RL, 2008, MR elastography of the lung with hyperpolarized ^3He , *Magn. Reson. Med.* 59, pp. 14-18.
- 71) McGee KP, Lake D, Mariappan Y, Hubmayr RD, Manduca A, Ansell K, Ehman RL, 2011, Calculation of shear stiffness in noise dominated magnetic resonance elastography data based on principal frequency estimation, *Phys. Med. Biol.* 56, pp. 4291–4309.

- 72) Meral FC, Royston TJ, Magin RL, 2009, Surface response of a fractional order viscoelastic halfspace to surface and subsurface sources, *J. Acoust. Soc. Am.* 126, pp. 3278–3285.
- 73) Meral FC, Royston TJ, Magin RL, 2010, Fractional calculus in viscoelasticity: an experimental study, *Commu. Nonlin. Sci. & Num. Simul.* 15 (4), pp. 939 -945.
- 74) Miller GF, Pursey H, 1954, The field and radiation impedance of mechanical radiators on the free surface of a semi-infinite isotropic solid, *Proc. Roy. Soc. A* 223, pp. 521–541.
- 75) Miller GF, Pursey H, 1955, On the partition of energy between elastic waves in a semi-infinite solid, *Proc. Roy. Soc. A* 223, pp. 55–69.
- 76) Mow VC, Kuei SC, Lai WM, Armstrong CG, 1980, Biphasic creep and stress relaxation of articular cartilage in compression: theory and experiments, *J. Biomech. Eng.* 102(1), pp. 73-84.
- 77) Murphy R, 2007, Computerized multichannel lung sound analysis: development of acoustic instruments for diagnosis and management of medical conditions, *IEEE Eng. Med. & Bio.* 26, pp. 16-19.
- 78) Muthupillai R, Lomas DJ, Rossman PJ, Greenleaf JF, Manduca A, Ehman, RL, 1995, Magnetic resonance elastography by direct visualization of propagating acoustic strain waves, *Science*, 269, pp. 1854–1857.
- 79) Napadow VJ, Mai, VM, Bankier AA, Gilbert RJ, Edelman RR, Chen Q, 2001, Determination of regional pulmonary parenchymal strain during normal respiration using spin inversion tagged magnetization, *J. Magn. Reson. Imag.* 13(3), pp. 467-474.
- 80) Oestreicher HL, 1951, Field and impedance of an oscillating sphere in a viscoelastic medium with an application to biophysics, *J. Acoust. Soc. Am.* 23, pp. 707–714.
- 81) Orescanin M, Insana MF, 2010, Shear modulus estimation with vibrating needle stimulation, *IEEE Trans. Ultrason. Ferroelectr. Freq. Contr.* 57, pp. 1358-1367.
- 82) Othman SF, Xu H, Royston TJ, Magin RL, 2005, Microscopic magnetic resonance elastography (μ MRE), *Magn. Reson. Med.* 54, pp. 605–614.

- 83) Ozer MB, Acikgoz S, Royston TJ, Mansy HA, Sandler RH, 2007, Boundary element model for simulating sound propagation and source localization within the lungs, *J. Acous. Soc. Amer.* 122 (1), pp. 657 – 671.
- 84) Paciej R, Vyshedskiy A, Shane J, Murphy R, 2003, Transpulmonary speed of sound input into the supraclavicular space, *J. Appl. Physiol.* 94, pp. 604-611.
- 85) Pasterkamp H, Kraman SS, Wodicka, GR, 1997, Respiratory sounds-advances beyond the stethoscope, *Am. J. Respir. Crit. Care Med.* 156(3), pp. 974-987.
- 86) Pasterkamp H, Consunji-Araneta R, Oh Y, Holbrow J, 1997, Chest surface mapping of lung sounds during methacholine challenge, *Pediatric Pulmonology*, 23, pp. 21 – 30.
- 87) Pasterkamp H, Patel S, Wodicka GR, 1997, Asymmetry of respiratory sounds and thoracic transmission, *Med. Biol. Eng. Comput.* 35, pp. 103–106.
- 88) Plona TJ, 1980, Observation of a second bulk compressional wave in a porous medium at ultrasonic frequencies, *Appl. Phys. Lett.* 36, pp. 259-261.
- 89) Qiang B, Greenleaf JF, Zhang XM, 2010, Quantifying viscoelasticity of gelatin phantoms by measurement impulse response using compact optical sensors, *IEEE Trans. Ultrason. Ferroelectr. Freq. Contr.* 57, pp. 1696–1700.
- 90) Rice DA, 1983, Sound speed in pulmonary parenchyma, *J. Appl. Physiol.* 54, pp. 304–308.
- 91) Riek K, Klatt D, Nuzha H, Mueller S, Neumann U, Sack I, Braun J, 2011, Wide-range dynamic magnetic resonance elastography, *J. Biomech. Eng.* 44, pp. 1380–1386.
- 92) Royston TJ, Ozer MB, Acikgoz S, Mansy HA, Sandler RH, 2008, Advances in computational modeling of sound propagation in the lungs and torso with diagnostic applications, Chapter 9, in *Vibration and acoustics in biomedical applications: imaging, characterization and diagnostics*, ASME Press.
- 93) Royston TJ, Mansy HA, Sandler RH, 1999, Excitation and propagation of surface waves on a viscoelastic half-space with application to medical diagnosis, *J. Acoust. Soc. Am.* 106, pp. 3678–3686.

- 94) Royston TJ, Zhang X, Mansy HA, Sandler RH, 2002, Modeling sound transmission through the pulmonary system and chest with application to diagnosis of a collapsed lung, *J. Acous. Soc. Amer.* 111, pp. 1931 – 1946.
- 95) Royston TJ, Yazicioglu Y, Loth F, 2003, Surface response of a viscoelastic medium to subsurface acoustic sources with application to medical diagnosis, *J. Acous. Soc. Amer.* 113, pp. 1109 – 1121.
- 96) Royston TJ, Dai Z, Chaunsali R, Liu Y, Peng Y, Magin RL, 2011, estimating material viscoelastic properties based on surface wave measurements: a comparison of techniques and modeling assumptions, *J. Acous. Soc. Amer.* 130(6), pp. 4126-4138.
- 97) Saibene F, Mead J, 1969, Frequency dependence of pulmonary quasi-static hysteresis, *J. Appl. Physiol.* 26, pp. 732-737.
- 98) Sarvazyan AP, Rudenko OV, Swanson SD, Fowlkes JB, Emelianov SY, 1998, Shear wave elasticity imaging: a new ultrasonic technology of medical diagnostics, *Ultrasound in Med. & Biol.* 24, pp. 1419–1435.
- 99) Sarvazyan AP, 2005, Audible-frequency medical diagnostic methods: past, present and future, *J. Acous. Soc. Amer.* 117, pp. 2586.
- 100) Schanz, M, 2001, *Wave propagation in viscoelastic and poroelastic continua: a boundary element approach*, Springer, Berlin.
- 101) Shah NS, Kruse SA, Lager DJ, Farell-Baril G, Lieske JC, King BF, Ehman RL, 2004, Evaluation of renal parenchymal disease in a rat model with magnetic resonance elastography, *Magn. Reson. Med.* 52(1), pp. 56-64.
- 102) Sharp JT, Johnson FN, Goldberg NB, Van Lith P, 1967, Hysteresis and stress adaptation in the human respiratory system, *J. Appl. Physiol.* 23, pp. 487-497.
- 103) Siklosi M, Jensen OE, Tew RH, Logg A, 2008, Multiscale modeling of the acoustic properties of lung parenchyma, *ESAIM: Proc.* 23, pp. 78-97.
- 104) Simon BR, 1992, Multiphase poroelastic finite element models for soft tissue structures, *Appl. Mech. Rev.* 45, pp. 191-218.

- 105) Simon BR, Liable JP, Pflaster D, Yuan Y, Krag MH, 1996, A poroelastic finite element formulation including transport and swelling in soft tissue structures, *J. Biomech. Eng.* 118, pp. 1-9.
- 106) Sinkus R, Tanter M, Xydeas T, Catheline S, Bercoff J, Fink M, 2005, Viscoelastic shear properties of in vivo breast lesions measured by MR elastography, *Magn. Reson. Imag.* 23(2), pp. 159-165.
- 107) Suki B, Habib RH, Jackson AC, 1993, Wave propagation, input impedance, and wall mechanics of the calf trachea from 16 to 1,600 Hz, *J. Appl. Physiol.* 75(6), pp. 2755-2766.
- 108) Suki B, Barabasi AL, Lutchen KR, 1994, Lung tissue viscoelasticity: a mathematical framework and its molecular basis, *J. Appl. Physiol.* 76, pp. 2749-2759.
- 109) Timoshenko SP, Goodier JN, 1970, *Theory of elasticity*, 3rd ed., McGraw-Hill, New York.
- 110) Vovk IV, Grinchenko VT, Oleinik VN, 1995, Modeling the acoustic properties of the chest and measuring breath sounds, *Acous. Phys.* 41, pp. 667 – 76.
- 111) Wang Z, Jean S, Bartter T, 2009, Lung sound analysis in the diagnosis of obstructive airway disease, *Respiration*, 77(2), pp. 134-138.
- 112) Williams JL, 1992, Ultrasonic wave propagation in cancellous and cortical bone: prediction of some experimental results by Biot's theory, *J. Acoust. Soc. Am.* 91(2), pp. 1106-1112.
- 113) Wochner MS, Ilinskii YA, Hamilton MF, Zabolotskaya EA, 2009, Model for fatigue and failure of human lung tissue subjected to low-frequency underwater sound, *Underwater Acoustics Measurements: Technologies and Results 2009 conference*, Nafplion, Greece.
- 114) Wodicka GR, Stevens KN, Golub HL, Cravalho EG, Shannon DC, 1989, A model of acoustic transmission in the respiratory system, *IEEE Trans. Biomed. Eng.* 36, pp. 925 – 34.
- 115) Wodicka GR, Stevens KN, Golub HL, Shannon DC, 1990, Spectral characteristics of sound transmission in the human respiratory system, *IEEE Trans. Biomed. Eng.* 37, pp. 1130-1134.
- 116) Wodicka GR, DeFrain PD, Kraman SS, 1994, Bilateral asymmetry of respiratory acoustic transmission, *Med. Biol. Eng. Comput.* 32, pp. 489–494.
- 117) Yamakoshi Y, Sato J, Sato T, 1990, Ultrasonic imaging of internal vibration of soft tissue under forced vibration, *IEEE Trans. Ultrason. Ferroelectr. Freq. Contr.* 37, pp. 45–53.

- 118) Yasar TK, Royston TJ, Magin RL, 2012, Wideband MR elastography for viscoelasticity model identification, *Magn. Reson. Med.* doi: 10.1002/mrm.24495.
- 119) Yen RT, Fung YC, Ho HH, Buttermann G, 1986, Speed of stress wave propagation in lung, *J. Appl. Physiol.* 61, pp. 701–705.
- 120) Zhang XM, Kinnick RR, Fatemi M, Greenleaf JF, 2005, Noninvasive method for estimation of complex elastic modulus of arterial vessels, *IEEE Trans. Ultrason. Ferroelectr. Freq. Contr.* 52, pp. 642–652 .
- 121) Zhang XM, Greenleaf JF, 2007, Estimation of tissue's elasticity with surface wave speed, *J. Acoust. Soc. Am.* 122, pp. 2522–2525.
- 122) Zhang XM, Kinnick RR, Greenleaf JF, 2008, Viscoelasticity of lung tissue with surface wave method, *Ultrasonics Symposium, IEEE*, pp.21-23.
- 123) Zhang XM, Qiang B, Urban MW, Kinnick R, Hubmayr R, Greenleaf JF, 2009, Quantitative surface wave method for measuring local viscoelasticity of lungs, *IEEE International Ultrasonics Symposium Proceedings*, pp.479-482.
- 124) Zhang XM, Osborn TG, Pittelkow MR, Qiang B, Kinnick RR, Greenleaf JF, 2011, Quantitative assessment of scleroderma by surface wave technique, *Med. Eng. & Phy.* 33, pp. 31-37.

VITA

NAME: Zoujun Dai

EDUCATION: B.S., Mechanical Engineering, Shanghai Jiaotong University, Shanghai, China, 2006.

Ph.D., Mechanical Engineering, University of Illinois at Chicago, Chicago, Illinois, 2013.

EXPERIENCE: Research Assistant, Acoustics and Vibration Laboratory, Department of Mechanical & Industrial Engineering, University of Illinois at Chicago, August 2007 – December 2012.

Teaching Assistant, ME 341 Experimental Methods in Mechanical Engineering, University of Illinois at Chicago, Fall 2007.

Teaching Assistant, ME 312 Dynamic Systems and Control, University of Illinois at Chicago, Spring 2008 & Spring 2010.

Teaching Assistant, ME 308 Mechanical Vibrations, University of Illinois at Chicago, Fall 2008 & Fall 2010.

HONORS: Provost's Award for Graduate Research, UIC, 2008.

Graduate College Travel Awards, UIC, 2010, 2011.

PROFESSIONAL MEMBERSHIP: American Society of Mechanical Engineers
Acoustical Society of America

PUBLICATIONS: Archival Journal

(1) Dai Z, Peng Y, Royston TJ, Mansy HA, Sandler RH, 2012, Poroviscoelastic models for sound and vibration in the lungs, submitted to *J. of Vib. & Acous.*

- (2) Royston TJ, Dai Z, Chaunsali R, Liu Y, Peng Y, Magin RL, 2011, Estimating material viscoelastic properties based on surface wave measurements: A comparison of techniques and modeling assumptions, *J. Acous. Soc. Amer.* 130(6), pp. 4126-4138.

Conference papers & presentations

- (1) Peng Y, Dai Z, Royston TJ, Mansy HA, Sandler RH, Chest response to vibratory excitation: advances beyond percussion, *ASME IMECE* (Nov. 9 - 15, 2012, Houston, TX).
- (2) Royston TJ, Yasar TK, Dai Z, A comparison of mechanical wave measurement techniques to quantify soft tissue viscoelasticity up to 8 kHz: a phantom study of shear, Rayleigh and Lamb waves, *164th Meeting of the Acoustical Society of America* (Oct. 22 – 26, 2012, Kansas City, MO).
- (3) Peng Y, Dai Z, Mansy HA, Royston TJ, Poroviscoelastic modeling of mechanical wave motion in the lungs, *ASME Summer Bioengineering Conference* (Jun. 20 – 23, 2012, Fajardo, Puerto Rico).
- (4) Royston TJ, Dai Z, Peng Y, Mansy HA, Fractional poroviscoelastic modeling of sound and vibration in the lungs, *4th International Conference on Porous Media & Annual Meeting of the International Society for Porous Media* (May 14 – 16, 2012, West Lafayette, IN).
- (5) Dai Z, Peng Y, Mansy HA, Royston TJ, Sandler RH, Estimation of local viscoelasticity of lungs based on surface waves, *ASME IMECE* (Nov. 11 - 17, 2011, Denver, CO). IMECE2011-65561.

- (6) Dai Z, Peng Y, Royston TJ, Array measurement and imaging of sound transmission through the lungs, *159th Meeting of the Acoustical Society of America* (Apr. 19 – 23, 2010, Baltimore, MD)
- (7) Royston TJ, Dai Z, Mazzucco M, The Audible Human Project: Modeling Subject-Specific Sound Transmission in the Lungs and Torso, *ASME IMECE* (Oct. 31 – Nov. 6, 2008, Boston, MA)
- (8) Dai Z, Royston TJ, Development and evaluation of computational and mechanical phantom models of lung and chest acoustics, *First International Symposium on Audible Acoustics in Medicine and Physiology* (Sept. 8 – 9, 2008, West Lafayette, IN)